

**Spatial Aspects of Nuclear Magnetic Resonance  
Spectroscopy: Static and Radio-Frequency  
Magnetic Field Gradients in Principle and  
Practice**

by

Aaron David Sodickson

Submitted to the Division of Health Sciences and Technology  
in partial fulfillment of the requirements for the degree of

Doctor of Philosophy in Medical Physics

at the

MASSACHUSETTS INSTITUTE OF TECHNOLOGY

May 1997

© Massachusetts Institute of Technology 1997. All rights reserved.

Author .....  
Division of Health Sciences and Technology  
April 1, 1997

Certified by .....  
David G. Cory  
Associate Professor of Nuclear Engineering  
Thesis Supervisor

Accepted by .....  
Martha L. Gray  
J. W. Kieckhefer Associate Professor of Electrical Engineering  
Co-Director, Division of Health Sciences and Technology

MASSACHUSETTS INSTITUTE OF TECHNOLOGY

SCHERER-PLUM

MAY 27 1997

**Spatial Aspects of Nuclear Magnetic Resonance  
Spectroscopy: Static and Radio-Frequency Magnetic Field  
Gradients in Principle and Practice**

by

Aaron David Sodickson

Submitted to the Division of Health Sciences and Technology  
on April 1, 1997, in partial fulfillment of the  
requirements for the degree of  
Doctor of Philosophy in Medical Physics

**Abstract**

All nuclear magnetic resonance (NMR) measurements are influenced by the spatial distribution of spin properties across the sample volume. This thesis presents a general theoretical treatment of spatial phenomena in NMR along with a number of experimental explorations.

A generalized  $k$  space formalism is described which lends physical insight into the spatial modulations underlying a wide variety of NMR experiments. The approach involves a Fourier decomposition of spin coherences into a set of basis functions that most naturally describes the evolution of the system under field gradients and RF pulses. It provides a straightforward physical interpretation of the sample's spatial behavior while simplifying the calculation of analytical results for any signal pathway of interest. The formalism is applied to a diverse range of NMR experiments, including imaging, echo experiments, flow and diffusion measurements, selective excitation sequences, and multiple quantum coherence pathway selection techniques.

A modification of the BIRD and TANGO sequences is presented which incorporates RF gradients to eliminate the net magnetization from uncoupled spins, while completely preserving magnetization with the proper scalar-coupling constant. The spatial variation of the  $B_1$  field strength—here due to the residual field inhomogeneity of a nominally homogeneous coil—causes dephasing of the uncoupled line while refocussing the desired magnetization in a rotary echo. The sequence is demonstrated for selective excitation of the satellites in a chloroform sample, yielding suppression of the uncoupled magnetization by a factor of approximately 800.

A simplified approach to shimming for a high resolution magic angle spinning (MAS) probe is developed. Correction fields of the desired symmetry about the sample's spinning axis are derived as linear combinations of the usual lab-frame spherical harmonic shim-field geometries. The effects of sample spinning are incorporated which further simplifies the shimming procedure.

Radiation damping results from a bulk interaction of the net transverse magneti-

zation with the RF coil. A heretofore unexpected radiation damping signal is demonstrated following a complete inversion of the equilibrium magnetization. This effect is explained by residual RF feedthrough to the coil, and by thermal noise intrinsic to the coil itself.

Thesis Supervisor: David G. Cory

Title: Associate Professor of Nuclear Engineering

## Acknowledgments

In part due to my father's descriptions of his PhD years at MIT ending in the early 60's, I started grad school anticipating a thriving intellectual community where science happened at blackboards and large wooden tables, their worn surfaces hinting at years of scholarly debate.

I owe a great debt of gratitude to my PhD thesis supervisor, Professor David Cory who, more than anyone else at MIT in my graduate years, is responsible for the fulfillment of my overly idealistic expectations. I have particularly enjoyed our brainstorming sessions at the blackboard (alas, the tables are formica), and feel fortunate to have found an advisor who shares pleasure in debating the details or the big picture, and in solving problems from their starting point, even when our predictions about outcome differ. David has truly been a superb mentor, and has profoundly influenced my thinking on nearly all aspects of Nuclear Magnetic Resonance.

I wish also to thank Dr. Werner Maas, who is not only an ever-cheerful and friendly presence in the lab, but a tremendous source of experimental knowledge as well. He has been particularly helpful in enhancing my understanding of the many experimental challenges involved in RF gradient work.

I am blessed with a wonderfully supportive, close, and yes, over-educated family. My brother, Daniel Sodickson, has been an excellent sounding-board, proofreader, and practice audience throughout my years at MIT. Our paths (both academic and geographic) have overlapped significantly, frequently triggering amusement in others, but a source of great pride to me. I have learned a great deal from him, and have thoroughly enjoyed and appreciate our many discussions about research, women, or life in general. His insight has been invaluable.

My Pop, Lester Sodickson, has been an outstanding role model for me as physicist, generalist, and fix-it guy. From my early days doing long-division or disassembling watches, he has been an ever-present source of encouragement, assistance, and patience. He has always remained thoroughly involved in my latest endeavors, and, despite all the lingo, stayed fully up to date on the thrust of my PhD work.

It is a rare physicist who can discuss intricate details of k-space or spin-diffusion with his brother, while being stumped (momentarily of course) by his father at his thesis defense. I feel incredibly privileged to have both these physicists in my life. Although some have raised question about our topics of dinner conversation at home, it is indeed a rare privilege to have family who can so fully understand and contribute insight to one's work.

My dear twin sister Deborah has been an ever-present and indispensable part of my life, from zygote to playmate to dedicated neuroscientist. Her unassuming warmth and disarming sincerity have always given me a safe place to turn for love and understanding.

And finally, love and thanks to my Mom, Isabel Sodickson, the glue that binds us all together. She is the central star about whom we all revolve. Her talents as a psychiatric social worker have kept us all (relatively) well adjusted, and have fully impressed upon me the value of nurturing guidance.

To my friends at MIT (you know who you are), it has been a great pleasure to know you, both at work and at play.

I am grateful to the Office of Naval Research and to the Medical Engineering/Medical Physics (MEMP) program in the Harvard-MIT Division of Health Sciences and Technology (HST) for many terms of graduate fellowship support. My work (and my rent) have also been funded in part by the National Institute for Health and the National Science Foundation.

# Contents

<b>Introduction</b>	<b>13</b>
<b>1 A Generalized <math>k</math>-Space Formalism For Treating the Spatial Aspects of A Variety Of NMR Experiments</b>	<b>16</b>
1.1 Introduction . . . . .	16
1.2 $k$ -Space Picture of the Magnetization Grating . . . . .	17
1.2.1 Static Field Gradients . . . . .	17
1.2.2 RF Pulses . . . . .	18
1.2.3 Fourier Decomposition of the Magnetization Grating . . . . .	19
1.3 Imaging . . . . .	21
1.4 Transformation Properties . . . . .	24
1.4.1 Illustrative Example — the Hahn Echo Experiment . . . . .	24
1.4.2 Generalized RF Transformations . . . . .	25
1.5 Echo Experiments . . . . .	29
1.5.1 General Two-Pulse Echo Experiment . . . . .	30
1.5.2 The Stimulated Echo Experiment . . . . .	31
1.6 Moving Spins . . . . .	34
1.6.1 Flow . . . . .	35
1.6.2 Diffusion . . . . .	41
1.7 Generalizations to Spectroscopy . . . . .	46
1.7.1 Selective Excitation . . . . .	49
1.8 Gradient Selection of Multiple Quantum Coherence Pathways . . . . .	55
1.8.1 Background . . . . .	55

1.8.2	Homonuclear Experiments . . . . .	56
1.8.3	Heteronuclear Experiments . . . . .	63
1.8.4	General Concerns in Gradient Selection Sequences . . . . .	64
1.9	Summary and Conclusions . . . . .	68
<b>2</b>	<b>RF Gradient BIRD/TANGO Sequence to Eliminate Uncoupled Magnetization</b>	<b>74</b>
2.1	Introduction . . . . .	74
2.2	RF vs. $B_0$ Gradients . . . . .	76
2.2.1	RF Gradients in Practice . . . . .	80
2.3	Background for the BIRD and TANGO Sequences . . . . .	86
2.3.1	Pulse Sequence Building Blocks . . . . .	86
2.3.2	Standard BIRD Sequence . . . . .	87
2.3.3	Standard TANGO Sequence . . . . .	89
2.4	RF Gradient Sequences . . . . .	89
2.4.1	RF Gradient BIRD (rBIRD) . . . . .	90
2.4.2	RF Gradient TANGO . . . . .	92
2.4.3	Miscalibration Error Terms . . . . .	92
2.5	Experimental Results . . . . .	94
2.6	Discussion . . . . .	95
2.7	Conclusions . . . . .	101
<b>3</b>	<b>Shimming a High Resolution MAS Probe</b>	<b>105</b>
3.1	Introduction . . . . .	105
3.2	Standard Lab-Frame Shim Geometries . . . . .	107
3.3	Shims in the Tilted MAS Frame . . . . .	109
3.4	Simplifications due to Sample Spinning . . . . .	112
3.5	Conclusions . . . . .	115
<b>4</b>	<b>The Initiation of Radiation Damping by Noise</b>	<b>117</b>
4.1	Introduction . . . . .	117

4.2	Background—Radiation Damping . . . . .	118
4.3	Experimental Results and Interpretation . . . . .	123
4.4	Discussion and Conclusions . . . . .	127



# List of Figures

1-1	Basis functions for Fourier decomposition of the magnetization grating. A) A longitudinal amplitude modulation. B) A right-handed, and C) a left-handed transverse magnetization helix. . . . .	20
1-2	A simple imaging experiment. Gradient evolution shifts the sample's intrinsic spatial variation to higher $k$ values. . . . .	23
1-3	A Hahn echo experiment in a constant gradient field . . . . .	24
1-4	A generalized two-pulse echo experiment, with arbitrary pulse-lengths and relative phases. . . . .	30
1-5	A generalized stimulated echo experiment, with arbitrary pulse-lengths and relative phases. . . . .	33
1-6	Flow-induced phase offsets for longitudinal and transverse magnetiza- tion grating components. . . . .	36
1-7	Motion sensitive gradient experiments, their corresponding $k$ -trajec- tories, and their flow induced phase-offsets $\theta_v$ . . . . .	38
1-8	Velocity-compensated gradient profiles, with their corresponding $k$ - space trajectories and flow-dependent phase factors. . . . .	40
1-9	A PGSE experiment with a constant gradient present for the entire duration of the experiment, in addition to the standard gradient pulses.	43
1-10	A stimulated echo experiment demonstrating bounded diffusion . . .	45
1-11	The jump-return experiment, with its corresponding $k$ -analog descrip- tion. . . . .	49
1-12	A DANTE sequence, composed of equally spaced RF pulses. . . . .	50

1-13	A COSY experiment using pulsed gradients for coherence pathway selection. . . . .	59
1-14	Double Quantum Filtered COSY experiment using pulsed gradients for coherence pathway selection. . . . .	62
1-15	A heteronuclear multiple quantum coherence experiment using pulsed gradients for coherence pathway selection. . . . .	65
2-1	A nutation experiment demonstrating the residual RF inhomogeneity of a nominally homogeneous coil. . . . .	81
2-2	A 2D nutation experiment mapping out the $B_1$ field strength as a function of position along z in the sample. . . . .	83
2-3	Chemical shift as a function of position along z. . . . .	84
2-4	$B_1$ field strength as a function of chemical shift value. . . . .	85
2-5	A common pulse-sequence building block, responsible for the selectivity of the standard BIRD and TANGO sequences and their RF-gradient modifications. . . . .	88
2-6	The RF gradient rBIRD sequence, and it's effects on uncoupled and coupled magnetization components. . . . .	91
2-7	Spectra obtained on a chloroform sample. A) The normal spectrum. B) Satellite inversion with the BIRD sequence. C) Elimination of the uncoupled central line with the rBIRD sequence. . . . .	96
2-8	The residual magnetization that remains after an RF gradient pulse due to spin-locking about the tilted effective RF axis. . . . .	100
3-1	Plots of the nodal surfaces for selected lab-frame shims . . . . .	110
4-1	The reaction field responsible for radiation damping . . . . .	119
4-2	An inversion recovery experiment, demonstrating the rapid return to equilibrium in the presence of radiation damping. . . . .	122
4-3	Radiation damping signals after a "perfect" $\pi$ pulse. . . . .	124

4-4 Coherent and incoherent radiation damping signals initiated, respectively, by spectrometer feedthrough and thermal noise. . . . . 126

# List of Tables

1.1	K-Space Transformations Effected by an on-resonance RF Pulse $\alpha)_\phi$ .	26
1.2	K-Space Transformations Effected by an RF Pulse $\alpha)_\phi$ applied at a resonance offset of $\Delta\omega$ . . . . .	29
1.3	Echo times, amplitude factors, and phase factors for the 5 echoes formed during a 3-pulse stimulated echo experiment. . . . .	32
2.1	Comparison of error terms for the standard and RF-Gradient BIRD sequences. . . . .	94
3.1	Lab frame zonal shims in cartesian coordinates. . . . .	107
3.2	Lab frame tesseral shims in cartesian coordinates. . . . .	108
3.3	Tilted-frame shims expressed as linear combinations of the lab-frame shims . . . . .	113

# Introduction

A focus on spatial aspects in NMR is the underlying theme unifying the otherwise diverse set of topics in this thesis. Due to the construction of the NMR experiment, the detected signal reflects the behavior of magnetization integrated over the entire sample volume. Techniques employing field gradients have become widespread to produce spatial modulations of coherences across the sample. Gradients both in the  $B_0$  field and the RF field may be used for a wide range of applications to encode spatial information or to select desired signal pathways. Meanwhile, unwanted spatial variations inevitably exist in the form of magnetic field inhomogeneities. Substantial effort is exerted to minimize these influences. Furthermore, the behavior of the magnetization as a whole may be altered by its bulk interaction with the RF coil. The work that follows addresses various theoretical and practical issues raised by these diverse spatial effects.

Chapter 1 describes a generalized  $k$  space formalism designed to lend insight into the spatial aspects of a wide variety of NMR experiments. The approach involves a Fourier decomposition of the spatial behavior of coherences across the sample into a set of basis functions that most naturally reflects the evolution in linear field gradients and RF pulses. It provides a rapid means of understanding the sample's underlying spatial behavior, while providing a complete analytical description for all components and coherences of the spin magnetization. The formalism is applied to many experiments, including imaging, echo experiments, selective excitation sequences, and multiple quantum coherence pathway selection techniques in both homonuclear and heteronuclear spin systems. A large variety of physical phenomena are incorporated in the  $k$  space description, including relaxation, evolution in inhomogeneous inter-

actions such as linear field gradients, static field inhomogeneities and chemical shift, motion effect such as uniform flow and molecular diffusion, and J-coupling in multi-spin systems.

Chapter 2 presents a novel modification of the BIRD and TANGO pulse sequences. The new sequence employs radio-frequency field gradients to eliminate the net magnetization from uncoupled spins, while completely preserving coupled magnetization. The standard BIRD and TANGO sequences cause selective nutation of protons directly bound to a coupling partner, while returning uncoupled magnetization to  $+z$ . These sequences lend themselves naturally to modification using RF gradients, which require no increase in pulse sequence complexity. These RF gradients provide substantial suppression of uncoupled resonances and elimination of typical antiphase and multiple-quantum error terms that arise from improperly set pulse lengths or delays. In the RF-gradient BIRD/TANGO sequence, the uncoupled magnetization is dephased in a plane orthogonal to the RF axis, while the desired signal components are refocussed, effectively in a rotary echo. The sequence has applications to solvent suppression and selective isotopomer excitation.

Chapter 3 describes an approach to shimming for a high resolution magic-angle-spinning (MAS) probe. In high resolution spectroscopy, a static  $B_0$  field is required to be as homogeneous as possible, in order to achieve narrow linewidths by reducing spatial variations in Larmor frequency. In the lab frame, current is adjusted through shim coils that produce magnetic fields varying spatially as the spherical harmonics, in order to reduce each component of the net field inhomogeneity. When the sample is tilted to the magic angle, however, these shim geometries no longer have the desired symmetry about the sample axis. However, new shim fields of the desired geometry in the tilted frame may be formed through linear combination of the lab frame correction fields, allowing the tilted sample to be shimmed as usual by varying currents to the lab frame shims in the appropriate combinations. Rapid spinning about the magic angle further simplifies the task, by eliminating the effect of all field configurations except those that are cylindrically symmetric about the spinning axis. A shimming strategy for an MAS sample is discussed, based on an understanding of the correction

field geometries and the simplifications arising due to rapid sample spinning.

The topic of Chapter 4 is the initiation of radiation damping by noise. In certain conditions, radiation damping causes a rapid return of the net magnetization vector to the equilibrium orientation along  $z$ . It is caused by the interaction between the RF coil and the net transverse magnetization integrated over the entire sample volume. Following an inversion pulse, this net transverse component is zero, yet radiation damping occurs nonetheless, contrary to the predictions of the standard theory. Here, two effects are discussed which are capable of initiating the radiation damping process in these circumstances, causing a departure from the unstable magnetization state along  $-z$ . Residual RF leakage to the probe causes a coherent effect, while thermal noise initiates the process incoherently, and is observable only after sources of RF leakage have been eliminated.

References for each topic appear at the end of the corresponding chapter.

# Chapter 1

## A Generalized $k$ -Space Formalism For Treating the Spatial Aspects of A Variety Of NMR Experiments

### 1.1 Introduction

The objective of this work is to create a complete and correct description of the spatial dependence of nuclear magnetization in terms of a Fourier decomposition into components modulated at different spatial frequencies. Just as the conventional  $k$ -space picture is of great use in understanding the spatial aspects of imaging experiments [1], the more general  $k$ -space formalism presented here provides an intuitive physical picture which lends insight into a wider variety of NMR experiments.

In typical experiments, the application of static field gradients and RF pulses creates a spatial variation of the magnetization throughout the sample. This spatial dependence may become quite complex, and will be referred to as the “magnetization grating,” a term motivated by Mansfield and Grannell’s analogy between gradient techniques and optical diffraction [2]. The components of this grating transform



quite simply in the presence of gradients and RF pulses, so it is straightforward to describe the dynamics of a system by tracking changes in the magnetization grating with time.

By following the development of the grating, diverse classes of NMR experiments are easily analyzed, including imaging, echo experiments, selective excitation sequences, and multiple quantum coherence gradient selection methods. The effects of relaxation, flow, molecular diffusion, chemical shift and spin-spin couplings are also easily incorporated. In principle, any sequence of hard RF pulses and  $B_0$  gradients may be treated with this formalism, which provides enhanced insight with no sacrifice in analytical correctness. While the description is cast in a form that makes it most directly applicable to gradient experiments, a simple correspondence may be established which permits treatment of evolution under other inhomogeneous interactions as well, such as the chemical shift or static field inhomogeneities.

## 1.2 $k$ -Space Picture of the Magnetization Grating

It is well known that a combination of magnetic field gradients and RF pulses leads to a periodic modulation of the nuclear spin magnetization in a uniform sample. Here the NMR response will be tied directly to two independent spatial modulations of the spin magnetization, that due to the intrinsic variation in the sample's spin density, and that due to the action of field gradients and RF pulses.

### 1.2.1 Static Field Gradients

The presence of the strong external  $B_0$  field imposes upon the NMR experiment a cylindrical symmetry about the  $z$ -axis. During periods of free evolution, only those interactions which are secular — those that commute with the strong Zeeman Hamiltonian — have an effect on the spin system, as non-secular interactions are second averaged to zero by the rapid precession about  $z$ , and do not therefore contribute coherently to the overall spin dynamics. The  $I_z$  Hamiltonians (inhomogeneous interactions) that contribute to free evolution cause rotations about the  $z$ -axis, leaving

longitudinal magnetization unperturbed while altering the phase of the transverse magnetization. In the presence of a static field gradient  $G_u = \partial B_z / \partial u$  along the  $\hat{u}$  direction, the precession frequency varies linearly with position  $u$ , and causes the local transverse phase to change by  $\gamma G_u u dt = u dk_u$  during the time interval  $dt$ , where  $k_u$  contains all but the linear spatial dependence of the phase factor. In the absence of intervening RF pulses, gradient evolution thus alters the transverse  $k$ -value by,

$$\Delta k_u^{trans} = \gamma \int G_u dt = \gamma \int \frac{\partial B_z}{\partial u} dt, \quad (1.1)$$

with no effect on the longitudinal magnetization. Transverse magnetization that is initially uniform across the sample is thus wound by gradient evolution into an ever-tightening spatial helix about the  $\hat{u}$  direction. By employing the convention of treating transverse magnetization as lying in the complex plane — with  $M_x$  real and  $M_y$  imaginary — such spatial helices may be described as  $e^{i(k_u u + \theta)}$ . This helix corresponds to linear phase ramps as the transverse phase relative to the x-axis increases linearly through the sample along the  $\hat{u}$  direction. The parameter  $k_u$  describes the wavenumber of the modulation, or the pitch of the helix:  $k_u = 2\pi/\lambda$ , where  $\lambda$  is the wavelength. The parameter  $\theta$  is the overall phase offset of the modulation. For example, if a transverse grating component is formed by gradient evolution from a magnetization state that is initially uniform along the x-axis, the phase offset of the resulting helix remains  $\theta = 0$ , regardless of the wavenumber, while magnetization along y yields a helix with offset  $\theta = \pi/2$ .

### 1.2.2 RF Pulses

In contrast to evolution under a secular gradient interaction, RF pulses cause rotations about the transverse RF axis. They have no effect on the transverse magnetization oriented along the RF axis but instead cause mixing between longitudinal magnetization and the transverse component orthogonal to the RF axis. As a result, RF pulses make it possible to produce longitudinal magnetization gratings that are amplitude modulated as  $\sin(k_u u + \theta)$ , for example by placing the  $M_y$  component of a

transverse helix along the z-axis with a  $\pi/2)_x$  pulse. Similarly, a  $\pi)_x$  pulse inverts the transverse magnetization along the y-axis only, thus inverting a transverse grating from, for example, a right-handed to a left-handed helix, or equivalently, reversing the sign of  $k_u$ . Since homogeneous RF pulses cannot alter the spatial distribution of magnetization, they do not change the  $k$ -value of magnetization components, but cause purely a mixing between longitudinal and transverse components of the same absolute  $k$ -value.

### 1.2.3 Fourier Decomposition of the Magnetization Grating

The magnetization along each cartesian axes in the rotating frame is a real function of the position  $u$ . Any spatial modulation of  $M_x$ ,  $M_y$ , or  $M_z$  may thus be decomposed into a real-valued Fourier sum of components amplitude-modulated as  $\sin(k_u u + \theta)$ , where, as above,  $k_u$  is the spatial wavenumber of the component, and  $\theta$  is an overall phase factor that applies to all spins of the component. Throughout this work,  $u$  indicates the direction along which the spatial modulation of interest occurs, typically the lab-frame direction along which an externally applied field gradient varies. Since gradient evolution modulates transverse magnetization into characteristic spatial helices, it is most natural to decompose transverse gratings into such helical components. Indeed, the sinusoidal amplitude modulations along  $M_x$  and  $M_y$  are easily recombined to form the helical phase modulations in the complex plane,

$$M_x \cos(k_u u + \theta) \pm M_y \sin(k_u u + \theta) \longleftrightarrow e^{i(\pm k_u u + \theta)}, \quad (1.2)$$

where the component with  $+k_u$  corresponds to a helix varying along  $u$  in a right-handed sense, and that with  $-k_u$  varies in a left-handed sense.

At a given absolute wavenumber  $|k_u|$  in this formalism, longitudinal magnetization is amplitude-modulated along the  $u$  direction as  $\sin(k_u u + \theta)$ , while transverse magnetization is phase-modulated as  $e^{i(\pm k_u u + \theta)}$ , in right and left-handed spatial helices about the  $\hat{u}$  direction. These three functions—depicted in Fig. 1-1—form a complete basis set: Any spatial modulation along the  $\hat{u}$  direction—of either longitudinal or transverse magnetization—may be decomposed into a Fourier sum of these basis

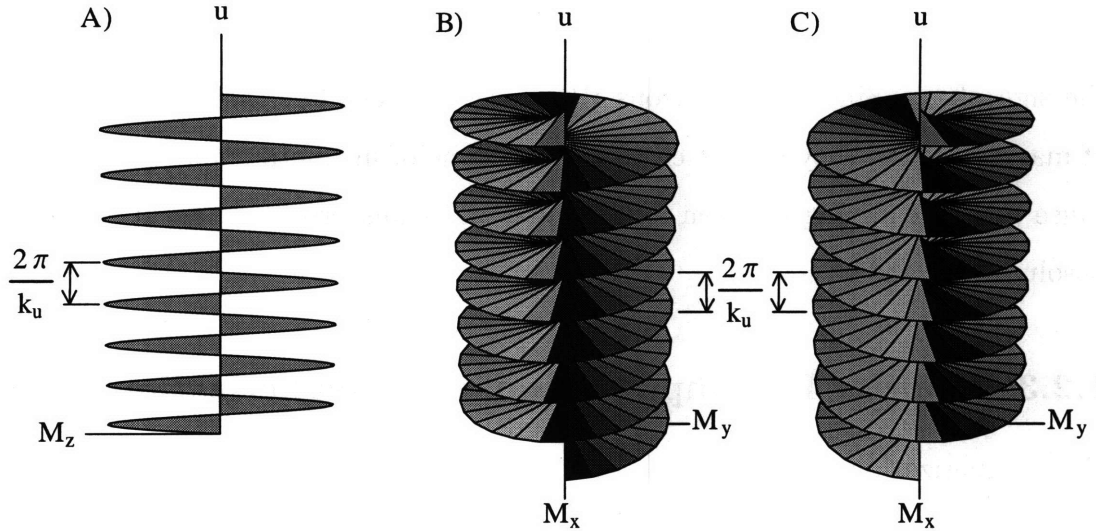


Figure 1-1: Basis functions for Fourier decomposition of any spatial modulation along  $\hat{u}$ . A) An amplitude modulation  $\sin(k_u u + \theta)\hat{z}$  describing the longitudinal magnetization. B) and C) Phase-modulated transverse magnetization grating components. B) A right-handed transverse magnetization helix  $e^{i(k_u u + \theta)}$ , and C) a left-handed helix  $e^{i(-k_u u + \theta)}$ . All three modulations share the same absolute wavenumber  $k_u$ , and are displayed with a phase offset  $\theta = 0$ . Gradient evolution alters the wavenumber of the transverse modulations, while RF pulses cause mixing between the three basis functions.

functions over different  $k_u$  values.

In the imaging literature, the integral in Eq. 1.1 is often used to define the absolute  $k_u$  value rather than the change  $\Delta k_u$ . The two descriptions correspond in the absence of intervening RF pulses. In this work, however, the definition of  $k$  is more general, designating instead the wavenumber of a given spatial component of the magnetization grating. This more general definition of  $k$ -value as modulation wavenumber is necessary for a correct description of the mixing effects of RF pulses.

Knowledge of the behavior of each Fourier component allows reconstruction of the spatial behavior of magnetization across the entire sample. Since  $k_u$  describes the spatial phase variation of transverse magnetization, or the amplitude variation of longitudinal magnetization, the only additional information that is needed to uniquely describe a modulation component is its phase offset at any one position. It is sim-

plest to track the phase offset  $\theta$  at  $u = 0$ , where the field strength due to applied gradients passes through zero. Evolution in  $B_0$  gradients then alters the transverse  $k_u$  in accordance with Eq. 1.1, causing a tightening or slackening of the magnetization helix, while leaving  $\theta$  unchanged. RF pulses, in contrast, cause mixing between the three types of modulations (right-handed and left-handed helices of transverse magnetization, and longitudinal amplitude modulations), all with the same absolute value of  $|k_u|$ . They cannot alter the modulation wavenumbers, but do influence the phase offsets  $\theta$  and the magnitude of each grating component. RF pulses thus modify the amplitude and phase of each Fourier component, while gradients cause these components to shift to different positions in  $k$ -space. Tracking the amplitude and phase of the longitudinal and transverse magnetization components at each  $k$ -value thus provides all the information necessary for a complete description of the full magnetization grating at any instant in time. Detection with a homogeneous RF coil is sensitive only to the transverse grating component with  $k = 0$ , as all spins contributing to this component share the same phase regardless of their position in the sample. All other components are spatially modulated as a function of position, and do not produce detectable signal, as cancellation between phases occurs.

### 1.3 Imaging

NMR imaging is generally concerned with a spatial map  $\rho(r)$  of spin density in the sample, often weighted in some fashion to create contrast based on relaxation times, flow, diffusion, or other physical characteristics of interest. The Fourier transform  $\tilde{\rho}(k)$  represents the decomposition of  $\rho(r)$  into a distribution of components modulated at each reciprocal-space value  $k$ . This distribution  $\tilde{\rho}(k)$  has not been created through gradient evolution, but rather reflects the intrinsic spatial variation of the sample geometry. A sample whose spin density is uniform and of infinite extent corresponds to a delta function in  $k$ -space,  $\tilde{\rho}(k) = \delta(k)$ , while Fourier analysis of a sample that varies spatially includes contributions from modulations of non-zero wavenumber, as is demonstrated in Fig. 1-2A for a rectangular sample geometry.

Signal detection measures the net signal integrated over the sample region, and is thus only sensitive to the spatial dc-value, the component at  $k = 0$ . All the spins of this component share the same phase with respect to the RF field, regardless of their location in the sample, and they thus add constructively, yielding an observable signal. This spatial dc-component at  $k = 0$  contains information only about the spatial average of the spin density, while information about all distinguishing sample features is contained in the  $k \neq 0$  components—those modulated at higher spatial frequencies. These Fourier components extend to infinity, so integration over all space yields complete signal cancellation as the local phase varies equally over all values. In order to reconstruct a meaningful image, a means is thus needed of detecting components of the distribution  $\tilde{\rho}(k)$  other than just  $k = 0$ .

Linear gradients, here along the  $u$  direction, are used to modulate the spin system with a linear-phase ramp of wavenumber  $\Delta k$ , as determined by Eq. 1.1. This gradient-induced modulation simply multiplies the spin density in the spatial domain, which, in the reciprocal  $k$ -space domain, corresponds to convolution with a shifted delta function,

$$\rho(r)e^{i\Delta ku} \xleftrightarrow{FT} \tilde{\rho}(k) \otimes \delta(k + \Delta k) = \tilde{\rho}(k + \Delta k). \quad (1.3)$$

Gradient evolution thus serves to shift the center of the sample's original  $k$ -space distribution to  $k = \Delta k$ . Signal detection then yields the component at  $k + \Delta k = 0$ . By using linear gradients in this manner to shift the  $k$ -space distribution before detecting the current dc component, the original  $\tilde{\rho}(k)$  may be sampled at desired points in  $k$ -space. Within the limits imposed by the Nyquist condition, Fourier transformation of the measured  $\tilde{\rho}(k)$  then returns  $\rho(r)$ . The imaging community typically speaks of measuring high  $k$  components, or of moving through  $k$ -space along a prescribed trajectory. To be more precise, each measurement in fact detects only the current  $k = 0$  component of the shifted  $k$ -space distribution, which, through gradient application, may indeed be made to correspond to a high  $k$ -value of the original unshifted spin density.

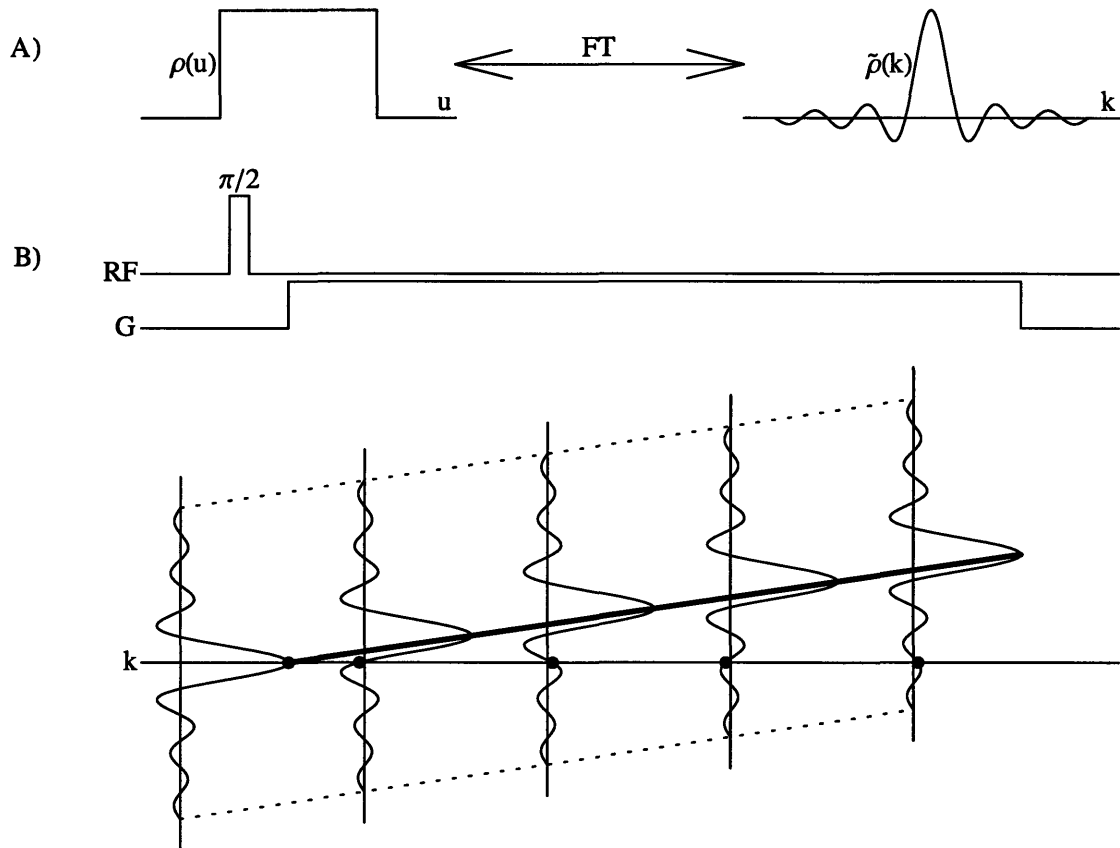


Figure 1-2: A simple imaging experiment. A) Spin density  $\rho(u)$  vs. position for a rectangular sample, and its Fourier transform  $\tilde{\rho}(k)$ . Signal detection measures only the  $k = 0$  component of the distribution, the net magnetization summed over the sample volume. B) Measurement of sample components modulated at higher spatial frequencies is made possible by evolution in a static gradient field. The bold line growing in  $k$  value tracks the modulation imposed upon the spin density by the gradient. This modulation causes the sample's  $k$ -space distribution to shift to higher  $k$  values. Signal detection samples the shifted distribution  $\tilde{\rho}(k + \Delta k)$  at  $k + \Delta k = 0$ . Sampling according to the Nyquist condition, followed by Fourier transformation, reproduces the original spatial distribution  $\rho(u)$ .

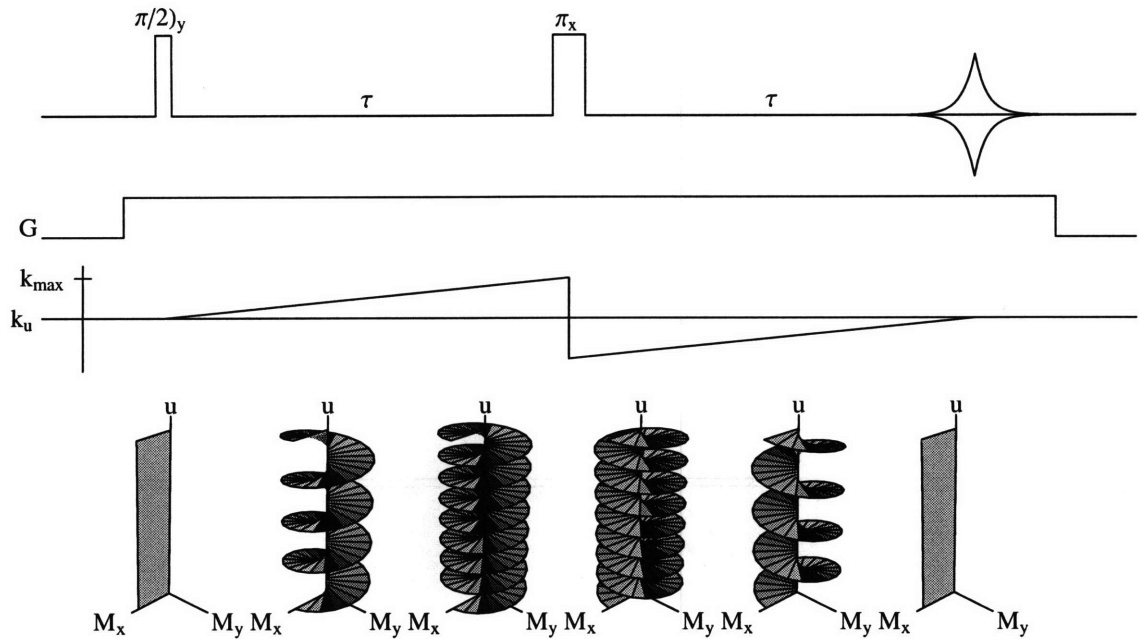


Figure 1-3: Hahn echo experiment in a constant gradient field. After the first pulse, transverse magnetization is spatially wrapped into tightening helices of growing  $k$  value. The  $\pi$  pulse inverts the sign of  $k$  and the sense of the transverse helix. Further gradient evolution then unwinds the transverse magnetization, rephasing spin packets from all locations along the same direction to form the echo.

## 1.4 Transformation Properties

In order to completely describe the spatial magnetization dependence of a sample, it is simply necessary to track the distribution of transverse and longitudinal  $k$  values, along with the corresponding amplitude and phase factors of each component. In following the spin dynamics during an experiment, it is thus crucial to understand how various  $k$  components evolve in a gradient field or transform to other  $k$ -components under the influence of RF pulses.

### 1.4.1 Illustrative Example — the Hahn Echo Experiment

Before the exact form of the transformations are described explicitly, the concepts will first be introduced with the Hahn echo experiment of Figure 1-3, performed in the presence of a constant field gradient.



After the  $\pi/2)_y$  pulse, the transverse magnetization begins in a spatially uniform state ( $k = 0$ ) along the x-axis. As described in Eq. 1.1, evolution in the presence of the static field gradient  $G$  causes the transverse  $k$  value to grow from zero with a linear dependence on time: a magnetization helix forms about the gradient direction, and is wrapped ever-tighter about this axis as time passes, ultimately reaching a final wavenumber of  $k_{max} = \gamma G \tau$  at time  $\tau$ .

The  $\pi_x$  pulse then inverts only the y-component of the transverse magnetization, thus inverting the sense of the helix from a right-handed to a left-handed screw, that is, from  $+k_{max}$  to  $-k_{max}$ . Evolution in the same gradient field for an additional time  $\tau$  then causes the helix to unwind from  $k = -k_{max}$  to  $k = 0$ , at which point an echo occurs as all the transverse magnetization is again aligned uniformly along the x-axis.

If the second RF pulse of Fig. 1-3 is made  $\pi/2)_x$  rather than  $\pi_x$ , it produces a sinusoidal modulation along the z-axis of wavenumber  $k_{max}$ , and a cosine modulation along the x-axis, which may be decomposed into equal contributions at  $+k_{max}$  and  $-k_{max}$ :  $\cos(k_{max}u) = (e^{+ik_{max}u} + e^{-ik_{max}u})/2$ . Gradient evolution during the second  $\tau$  period then refocusses only the transverse component with  $k_u = -k_{max}$ , resulting in an echo of half the amplitude. As these examples demonstrate, RF pulses are in general capable of mixing right and left-handed transverse modulation components  $e^{(i\pm k_u u + \theta)}$ , and longitudinal components  $\sin(k_u u + \theta)\hat{z}$ .

## 1.4.2 Generalized RF Transformations

Table 1.1 shows the mixing of modulation components caused by an on-resonance RF pulse  $\alpha)_\phi$ , which causes a rotation  $R(\alpha)_\phi$  through a nutation angle  $\alpha$  about a transverse axis oriented at phase  $\phi$  from the x-axis. Hennig [3] has previously derived a similar table of RF transformations using different definitions for the longitudinal basis functions, and with the RF phase  $\phi$  and all modulation phase offsets  $\theta$  set to zero. All magnitude terms in the transformation table depend only on the nutation angle  $\alpha$  and are independent of the RF phase, while the final phase offsets  $\eta$  depend only on the RF phase  $\phi$  and on the phase offset  $\theta$  of the starting modulation state. How these factors affect the transformation is of course dependent on which states

	+k transverse $Ae^{i(+ku+\eta)}$		-k transverse $Ae^{i(-ku+\eta)}$		+k longitudinal $A \sin(ku + \eta)\hat{z}$	
	Ampl. $A$	Phase $\eta$	Ampl. $A$	Phase $\eta$	Ampl. $A$	Phase $\eta$
+k trans. $e^{i(+ku+\theta)}$	$\cos^2(\frac{\alpha}{2})$	$\theta$	$\sin^2(\frac{\alpha}{2})$	$-\theta + 2\phi$	$\sin(\alpha)$	$\theta - \phi$
-k trans. $e^{i(-ku+\theta)}$	$\sin^2(\frac{\alpha}{2})$	$-\theta + 2\phi$	$\cos^2(\frac{\alpha}{2})$	$\theta$	$\sin(\alpha)$	$-\theta + \phi + \pi$
+k long. $\sin(ku+\theta)\hat{z}$	$\frac{1}{2} \sin(\alpha)$	$\theta + \phi + \pi$	$\frac{1}{2} \sin(\alpha)$	$-\theta + \phi$	$\cos(\alpha)$	$\theta$

Table 1.1: K-Space Transformations Effected by an on-resonance RF Pulse  $\alpha)_\phi$ . An RF-induced rotation through an angle  $\alpha$  about a transverse axis oriented at phase  $\phi$  from the x-axis, mixes basis functions without altering the wavenumber  $k$ . The starting magnetization states in the left-most column are transformed to the modulations in the uppermost row, with amplitudes that depend only on the nutation angle  $\alpha$  and phase-offsets that depend only on the RF-phase  $\phi$  and the starting offset  $\theta$ .

are mixed by the RF pulse.

### Transformation Amplitudes

Regardless of the RF phase of the  $\alpha$  nutation, a starting transverse modulation state of wavenumber  $\pm k$  transforms to the same state with an amplitude of  $\cos^2(\alpha/2)$ , to the transverse state of opposite  $k$  value with amplitude  $\sin^2(\alpha/2)$ , and to a longitudinal grating of wavenumber  $k$  with amplitude  $\sin(\alpha)$ . These magnitude terms arise from the effect of the RF pulse on only the component of the transverse magnetization orthogonal to the RF axis. An RF pulse along x mixes only  $M_y$  and  $M_z$ , so for a starting  $e^{iku}$  modulation, an  $\alpha_x$  pulse produces the transformation:

$$e^{iku} = [\cos(ku), \sin(ku), 0] \xrightarrow{\alpha_x} [\cos(ku), \sin(ku) \cos(\alpha), \sin(ku) \sin(\alpha)], \quad (1.4)$$

where the cartesian magnetization components are denoted as  $[M_x, M_y, M_z]$ . The  $M_z$  component is a longitudinal amplitude modulation of magnitude  $\sin(\alpha)$ , while the transverse components may be decomposed into phase modulated components,

$$e^{iku} \left( \frac{1 + \cos \alpha}{2} \right) + e^{-iku} \left( \frac{1 - \cos \alpha}{2} \right) = e^{iku} \cos^2 \left( \frac{\alpha}{2} \right) + e^{-iku} \sin^2 \left( \frac{\alpha}{2} \right). \quad (1.5)$$

The transformation amplitudes arising from a starting transverse modulation of wave-number  $-k$  arise in exactly the same manner.

Transforming a starting longitudinal modulation with an  $\alpha$ -pulse produces,

$$[0, 0, \sin(ku)] \xrightarrow{\alpha_x} [0, -\sin(ku) \sin(\alpha), \sin(ku) \cos(\alpha)], \quad (1.6)$$

leaving  $\cos(\alpha)$  along  $z$ , while producing an amplitude modulated component oriented along only one axis in the transverse plane. This transverse component is decomposed into counter-rotating phase-modulated components at  $\pm k$ ,

$$-i \sin(ku) \sin(\alpha) = \frac{\sin(\alpha)}{2} (-e^{iku} + e^{-iku}), \quad (1.7)$$

resulting in an amplitude factor of  $\sin(\alpha)/2$  for both transverse grating components.

## Transformation Phases

As seen in Table 1.1, when the RF transformation leaves some component of the modulation in the same starting and ending states, the phase offset remains unchanged—the effect of the RF is simply a reduction in the amplitude of that component. Transverse  $+k$  transforms to  $+k$ ,  $-k$  to  $-k$ , and longitudinal  $k$  to the same longitudinal  $k$  state with no change in the value  $\theta$  of the phase offset from start to finish, regardless of the phase of the RF pulse.

In contrast, when the RF-rotation produces an inversion of a transverse  $\pm k$  modulation to a spiral of the opposite handedness at  $\mp k$ , the phase offset is inverted as well. For example, a  $\pi_x$  pulse inverts  $M_y$  only, while leaving  $M_x$  unaltered. This causes a reversal everywhere of the local phase factor  $ku + \theta$ , inverting not only the  $k$ -value, but the offset  $\theta$  as well. Use of an RF-pulse of arbitrary phase  $\phi$  adds an additional phase offset of  $2\phi$ . This may be most easily understood by decomposing the rotation into component parts:  $R(\alpha)_\phi = R(-\phi)_z R(\alpha)_x R(+\phi)_z$ . Starting from an initial phase offset of  $\theta$ , a phase  $-\phi$  is added in the first  $z$ -rotation. The net offset is

then inverted to  $-\theta + \phi$  as the  $R(\alpha)_x$  rotation transforms  $+k$  to  $-k$ . Finally, the last z-rotation adds a further phase offset of  $+\phi$ , resulting in a final offset of  $-\theta + 2\phi$ .

Similar mechanisms are at play in determining the phase transformations between transverse and longitudinal gratings. These transformations contain only  $\pm\phi$  terms rather than  $\pm 2\phi$  terms, as one of the two z-rotations is applied to a longitudinal state and thus has no effect. Conversion from transverse  $+k$  to longitudinal  $k$  results in the starting offset  $\theta$  minus a  $\phi$  term arising from the  $R(-\phi)_z$  rotation applied to the transverse state. From transverse  $-k$  to a longitudinal  $k$  state, the  $-\phi$  rotation is followed by an inversion of the phase offset in concert with the  $k$  value inversion. There is also an additional  $\pi$  contribution that arises from the choice of the longitudinal grating basis function as a sine modulation. This extra phase term provides for the sign change when a transverse state is made to nutate first to the z-axis, then back into the transverse plane, as by two sequential  $\pi/2$  pulses. If instead cosine modulations were used as the longitudinal basis functions,  $\pm\pi/2$  phase terms would appear in each transformation between transverse states and longitudinal states, with the same net effect.

The reverse transformations from a longitudinal to a transverse state are unaffected by the first  $R(-\phi)_z$  rotation, but simply add a phase of  $+\phi$  from the final  $R(+\phi)_z$  rotation. In the transformation to transverse  $-k$ , this follows the inversion of the starting phase offset  $\theta$ . The transformation to transverse  $+k$  includes the same additional  $\pi$  contribution described above.

### Off-Resonance RF Transformations

The transformations of Table 1.1 are valid for on-resonance RF pulses only. If instead an RF pulse is applied off-resonance, the transformations must be modified as RF-induced rotations instead occur about a tilted effective axis in the rotating frame. For an RF pulse of length  $\tau$  and nominal nutation angle  $\alpha_0 = \omega_1\tau$  which is applied at a resonance offset of  $\Delta\omega$ , the net result is a rotation through an angle  $\alpha = \alpha_0\sqrt{1 + (\Delta\omega/\omega_1)^2}$  about an effective axis tilted out of the transverse plane by an angle  $\Delta = \tan^{-1}(\Delta\omega/\omega_1)$ . Table 1.2 shows the full mixing between basis functions

	+k transverse $Ae^{i(+ku+\eta)}$		-k transverse $Ae^{i(-ku+\eta)}$		+k longitudinal $A \sin(ku + \eta)\hat{z}$	
	Ampl. $A$	Phase $\eta$	Ampl. $A$	Phase $\eta$	Ampl. $A$	Phase $\eta$
+k trans. $e^{i(+ku+\theta)}$	$ T $	$\theta + \phi_T$	$\sin^2(\frac{\alpha}{2}) \cos^2 \Delta$	$-\theta + 2\phi$	$ L  \cos \Delta$	$\theta - \phi + \phi_L$
-k trans. $e^{i(-ku+\theta)}$	$\sin^2(\frac{\alpha}{2}) \cos^2 \Delta$	$-\theta + 2\phi$	$ T $	$\theta + \phi_T$	$ L  \cos \Delta$	$-\theta + \phi$ $+\pi - \phi_L$
+k long. $\sin(ku+\theta)\hat{z}$	$\frac{1}{2} L  \cos \Delta$	$\theta + \phi$ $+\pi + \phi_L$	$\frac{1}{2} L  \cos \Delta$	$-\theta + \phi + \phi_L$	$\cos \alpha \cos^2 \Delta$ $+\sin^2 \Delta$	$\theta$

$$\begin{aligned}
T_r &= \cos^2\left(\frac{\alpha}{2}\right) \cos^2 \Delta + \cos \alpha \sin^2 \Delta & L_r &= \sin \alpha \\
T_i &= \sin \alpha \sin \Delta & L_i &= 2 \sin^2\left(\frac{\alpha}{2}\right) \sin \Delta \\
|T| &= \sqrt{T_r^2 + T_i^2} & |L| &= \sqrt{L_r^2 + L_i^2} \\
\phi_T &= \tan^{-1}(T_i/T_r) & \phi_L &= \tan^{-1}(L_i/L_r)
\end{aligned}$$

Table 1.2: K-Space Transformations Effected by an RF Pulse  $\alpha)_\phi$  applied at a resonance offset of  $\Delta\omega$ . The tilted effective axis is at an angle  $\Delta = \tan^{-1}(\Delta\omega/\omega_1)$  from the transverse plane, and the effective nutation angle is lengthened to  $\alpha = \alpha_0\sqrt{1 + (\Delta\omega/\omega_1)^2}$ .

that is brought about by such an off-resonance RF pulse.

The amplitude terms now include a complex dependence on the resonance offset, both in the effective flip angle  $\alpha$  and in the tilt angle  $\Delta$  of the effective RF axis from the transverse plane. The phase factors have added contributions  $\phi_T$  and  $\phi_L$  that depend both on the offset value and on the nutation angle, in contrast to the phases of Table 1.1 which are independent of  $\alpha$ .

These transformations do of course reduce to those of Table 1.1 when the RF pulse is applied on resonance. Since  $\Delta\omega = 0$ , the tilt angle of the effective axis  $\Delta = 0$ , which causes both  $T_i$  and  $L_i$  to disappear. The added phase factors  $\phi_T$  and  $\phi_L$  thus also disappear, and all amplitude terms reduce to the previous values.

## 1.5 Echo Experiments

The transformations presented in Table 1.1 may be easily applied to echo experiments in order to derive echo amplitudes and phases. The descriptions presented below

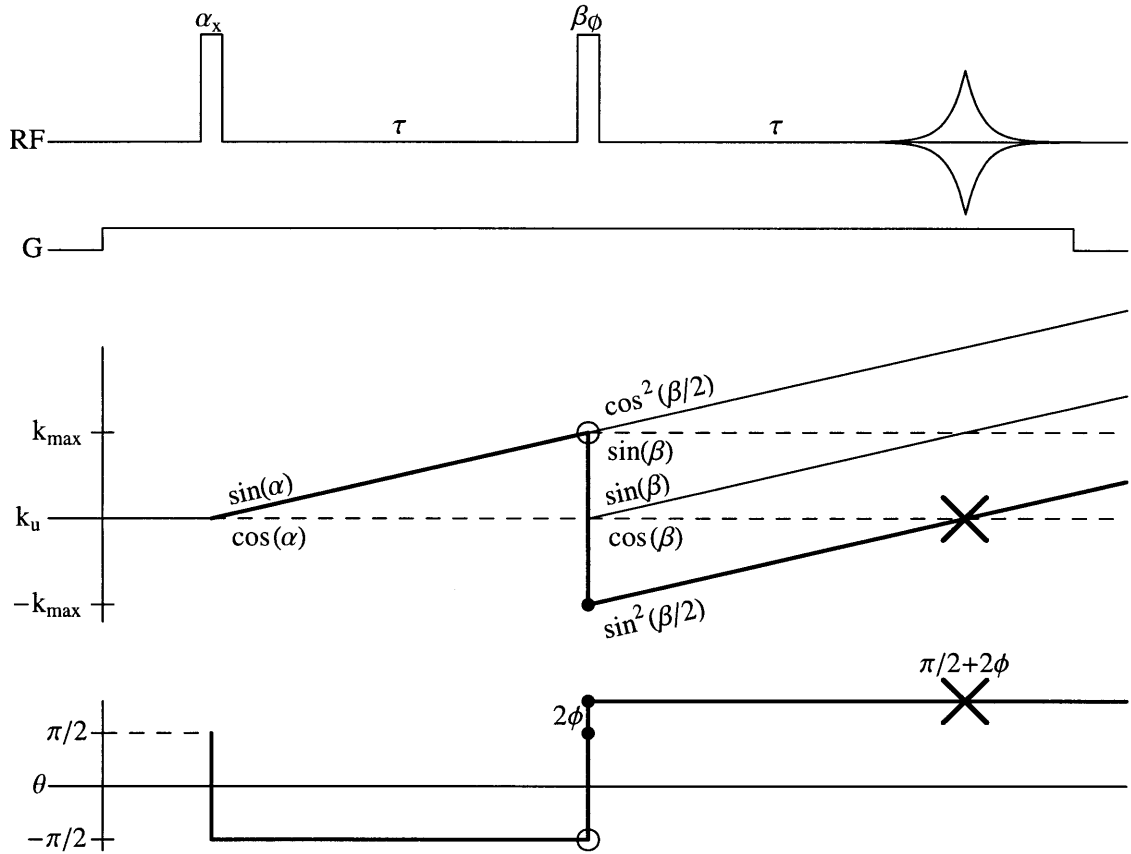


Figure 1-4: Generalized two-pulse echo experiment, with arbitrary pulse-lengths and relative phases. The only echo formed has amplitude  $\sin(\alpha) \sin^2(\beta/2)$  and phase offset  $\pi/2 + 2\phi$ .

follow the phase ( $ku + \theta$ ) at all locations by tracking changes in  $k$  and  $\theta$ . Echoes occur when  $k$  returns to zero, i.e. when spins at all positions  $u$  re-align at a final common phase of  $\theta$ .

### 1.5.1 General Two-Pulse Echo Experiment

Figure 1-3 demonstrates the evolution in  $k$ -value during a Hahn echo experiment, with the echo occurring when  $k$  is refocused to zero at time  $t = 2\tau$ . Figure 1-4 shows the more general case of the echo formed by two pulses of arbitrary flip angle and relative phase. Multiplicative amplitude factors are introduced by both RF-induced transformations, yielding a net echo amplitude of  $\sin(\alpha) \sin^2(\beta/2)$ . For the standard spin-echo sequence  $\pi/2 - \tau - \pi - \tau$ , this yields an echo amplitude of 1, while a

$\pi/2 - \tau - \pi/2 - \tau$  echo is reduced to an amplitude of  $1/2$ . The phase-offset diagram indicates the accumulation of the phase  $\theta$  for the refocussed  $k$ -pathway of interest. The first  $x$ -pulse nutates magnetization to the  $-y$  axis, producing a magnetization phase of  $-\pi/2$ . The second pulse inverts this phase offset in concert with the  $k$ -value inversion, and adds an additional  $2\phi$  as discussed in the last section, yielding a final echo phase of  $\theta = \pi/2 + 2\phi$ . This result of course matches the familiar echo behavior: An  $x, x$  echo is seen to occur along the  $+y$  axis at  $\theta = \pi/2$ , while an  $x, y$  echo occurs along the  $-y$  axis at  $\theta = 3\pi/2$ . These familiar results highlight the ease with which the  $k$ -space formalism may be used to describe the spatial aspects of experiments which might otherwise require more complicated analysis.

In this and other experiments described below, a uniform sample of infinite extent along the gradient direction is assumed, so that the initial distribution of  $k$  values  $\tilde{\rho}(k)$  may be treated as  $\delta(k)$ , thus simplifying the corresponding  $k$ -space diagrams. The modulations depicted in these diagrams correspond solely to the gratings imposed upon the spin density by the combination of RF pulses and periods of gradient evolution. In order to account for spatial variation of the spin density, these  $k$ -space trajectories must be convolved with the intrinsic spatial dependence of the sample, as described above for the imaging experiment. In this way, the simplified  $k$ -space diagrams shown trace the trajectory of the initial  $\tilde{\rho}(k = 0)$  point. As the gradient echo of Fig. 1-4 is formed, the sample distribution  $\tilde{\rho}(k)$  is swept through the detected  $k = 0$  point, resulting in an echo of finite width whose envelope matches  $\tilde{\rho}(k)$ . This produces the familiar result that Fourier transformation of a gradient echo yields a projection of the spin density along the gradient direction  $\hat{u}$ .

### 1.5.2 The Stimulated Echo Experiment

Adding a third RF-pulse to produce a stimulated echo results in a significant increase in complexity, producing 5 echoes which are more difficult to describe rigorously with other methods. The  $k$ -space approach allows simple extraction of echo times, amplitudes and phases, while providing valuable insight into the underlying spin dynamics. Figure 1-5 demonstrates the most general and thus most complex 3-pulse

echo #	time	amplitude	phase
1	$2t$	$\sin(\alpha) \sin^2(\frac{\beta}{2}) e^{-2t/T_2}$	$\frac{\pi}{2} + 2\phi_2$
2	$2t + T$	$\sin(\alpha) \sin(\beta) (\frac{\sin(\gamma)}{2}) e^{-2t/T_2} e^{-T/T_1}$	$\frac{\pi}{2} + \phi_2 + \phi_3$
3	$2T$	$\sin(\alpha) \sin^2(\frac{\beta}{2}) \sin^2(\frac{\gamma}{2}) e^{-2T/T_2}$	$-\frac{\pi}{2} - 2\phi_2 + 2\phi_3$
4	$2T + t$	$\sin(\beta) \sin^2(\frac{\gamma}{2}) e^{-2T/T_2} [1 - (1 - \cos(\alpha)) e^{-t/T_1}]$	$\frac{\pi}{2} - \phi_2 + 2\phi_3$
5	$2T + 2t$	$\sin(\alpha) \cos^2(\frac{\beta}{2}) \sin^2(\frac{\gamma}{2}) e^{-2(t+T)/T_2}$	$\frac{\pi}{2} + 2\phi_3$

Table 1.3: Echo times, amplitude factors, and phase factors for the 5 echoes formed during a 3-pulse stimulated echo experiment.

experiment with arbitrary RF nutation angles and phases. Echoes form at each zero-crossing of  $k$ . As in the previous 2-pulse experiment, amplitude and phase factors accumulate (multiplicatively and additively, respectively) at each RF-transformation, yielding simple expressions for each echo.

Table 1.3 tabulates echo times, amplitudes and phases for the 5 echoes of the 3-pulse stimulated echo experiment. Each RF pulse mixes every line in the  $k$ -space diagram into at most 3 components, with amplitude and phase factors determined from Table 1.1. By combining these factors along each pathway of interest, the overall amplitude and phase of each echo is easily determined. The utility of the stimulated echo experiment is in the formation of the stimulated echo at time  $2t + T$ , where  $t$  is the delay between the first two pulses, and  $T$  is the delay between the second and third pulses. Transverse magnetization produced by the first pulse is wound to a certain  $k$ -value by gradient evolution during the  $t$  delay. The second pulse then transforms a component of this grating into a longitudinal amplitude modulation of the same  $k$  value, which remains unaffected by gradient evolution during the long delay  $T$ . The horizontal dashed line in the figure indicates this stored longitudinal magnetization component. The third pulse returns a portion of this longitudinal magnetization component to the transverse plane, at which point decomposition into counter-rotating magnetization helices yields the amplitude factor of  $1/2$  which is a trademark of stimulated echo experiments. Unwinding of one of these components produces the stimulated echo after further gradient evolution of length  $t$ .



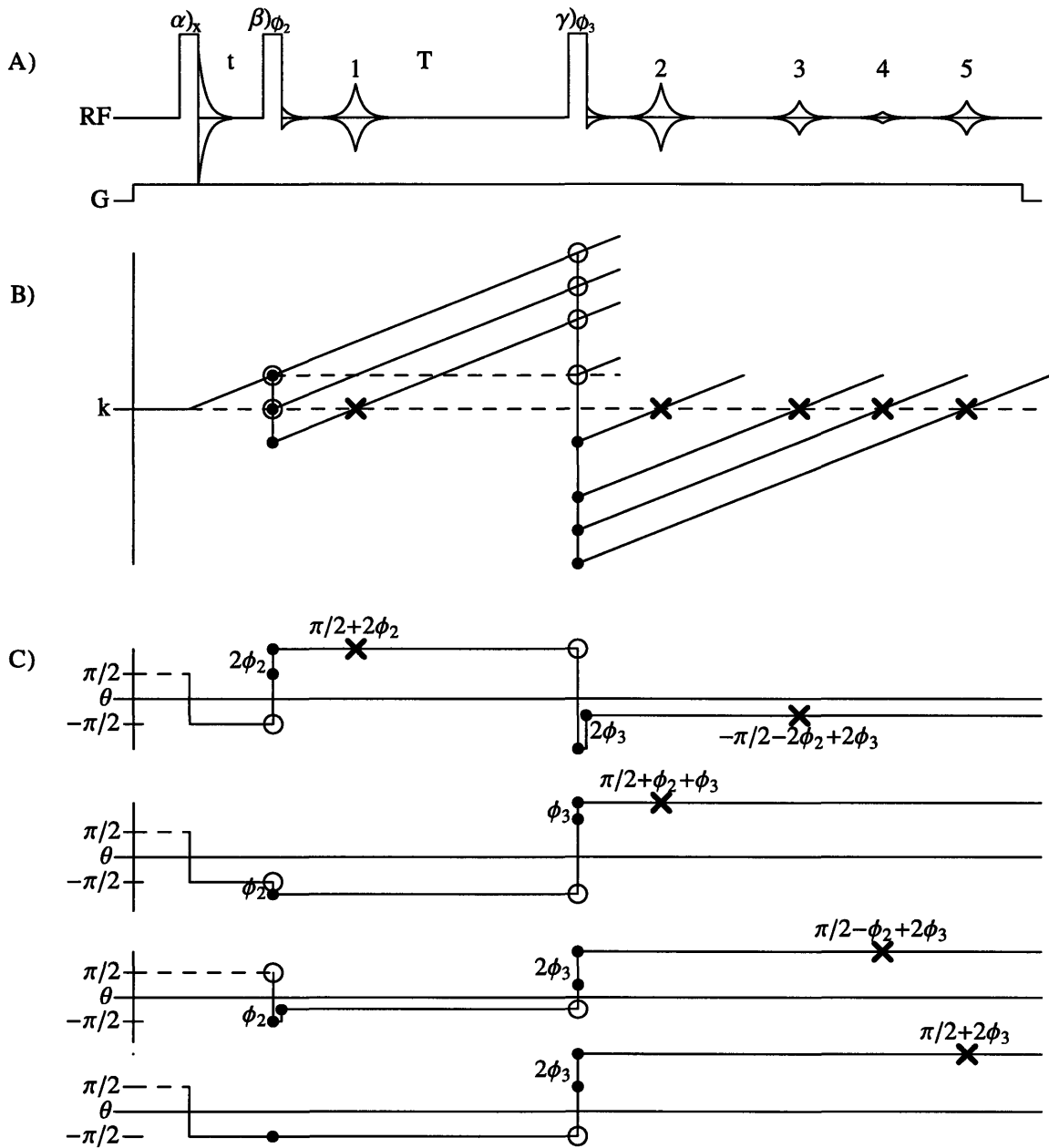


Figure 1-5: A) Generalized stimulated echo experiment, with arbitrary pulse-lengths and relative phases. Five echoes occur, at the zero-crossings of the  $k$ -space trajectories in B). Their amplitudes and phases are tabulated in Table 1.3. Echo 2 is the stimulated echo, which arises from the longitudinal modulation component which is drawn as a dashed line between the second and third pulses. The phase diagrams of C) correspond, from top to bottom, to echoes 1 and 3, echo 2, echo 4, and echo 5.

Echo 1 is a Hahn echo formed by the first two pulses, exactly as demonstrated in Fig. 1-4. Echo 2 is the stimulated echo described above, with the longitudinal storage period during the  $T$  delay. Echo 3 is a second refocussing of the magnetization that first generated echo 1. Echo 4 is a refocussing of magnetization placed into the transverse plane for the first time by the second pulse (and thus disappears if  $\alpha = \pi/2$  and  $T_1 \gg t$ ). Finally, echo 5 is a hahn echo formed by the first and third pulses, with the intervening pulse merely contributing an amplitude factor without inverting the transverse  $k$  value. If all three pulse lengths  $\alpha$ ,  $\beta$ , and  $\gamma$  are set to  $\pi/2$ , and in the absence of relaxation, the echo amplitudes, in order, would be  $1/2$ ,  $1/2$ ,  $1/4$ ,  $0$ ,  $1/4$ .

$T_1$  and  $T_2$  relaxation have been incorporated in Table 1.3 simply by accumulating multiplicative attenuation factors from each delay time along the  $k$ -pathway of interest, with decay terms inferred from the magnetization orientation either in the transverse plane or along the z-axis during each period of free-precession. The stimulated echo is the only one that decays as  $T_1$  rather than  $T_2$  during the long  $T$  delay. As a result, it is often used in experiments that require echo formation after times long compared to  $T_2$  but short compared to  $T_1$ , as in measurements of slow diffusion or flow. As is shown below, the effects of other phenomena such as bulk flow and unrestricted molecular diffusion are just as easily incorporated, introducing phase or magnitude terms during delay times.

## 1.6 Moving Spins

In general, the effect of spin motion on the spatial distribution  $\rho(r, \tau)$  of magnetization over time may be calculated by integrating the product of the initial distribution  $\rho(r, 0)$  with the conditional displacement probability  $P(r|r', \tau)$  that a spin will move from  $r$  to  $r'$  between times zero and  $\tau$ . If the displacement probability is spatially invariant, as in the case of uniform flow or unrestricted diffusion, this probability is a function of the displacement  $\Delta r = r - r'$  alone, and the integral simplifies to a convolution:

$$\rho(r, \tau) = \int dr' \rho(r, 0) \cdot P(r - r', \tau) = \rho(r, 0) \otimes P(r, \tau). \quad (1.8)$$

Fourier transform yields,

$$\tilde{\rho}(k, \tau) = \int \rho(r, \tau) e^{-i\vec{k} \cdot \vec{r}} dr = \tilde{\rho}(k, 0) \tilde{P}(k, \tau). \quad (1.9)$$

Standard gradient techniques used to study motion effects such as flow and diffusion are sensitive only to motion along the modulation axis of the grating. If, for example, a gradient is used to modulate a uniform sample along  $\hat{u}$ , then the grating imposed upon  $\rho(r)$  varies solely as a function of  $u$ , and the spatial convolution of Eq. 1.8 depends only on  $P(u, \tau)$ , the projection of  $P(r, \tau)$  along the  $u$  direction;  $\rho(r)$  remains uniform along the other sample axes, yielding an unchanged, uniform distribution after convolution along those axes. Equivalently, the Fourier transform  $\tilde{\rho}(k, \tau)$  of Eq. 1.9 picks out only the non-zero spatial components of the dot product  $\vec{k} \cdot \vec{r}$ , corresponding in the spatial domain to  $P(u, \tau)$ .

### 1.6.1 Flow

In the case of uniform flow of velocity  $\vec{v}$ , every spin, regardless of its starting position, moves a distance  $\Delta u = \hat{u} \cdot \vec{v} dt$  along the  $u$  direction during a time interval  $dt$ . Any magnetization grating, composed of longitudinal or transverse modulation components, is thus displaced a fixed distance. This uniform shift of the grating does not change the wavenumber  $k_u$  of any component, and does not attenuate the magnitude of that component, but solely induces a phase shift [4] that depends on the ratio of the displacement to the spatial wavelength of the modulation component:

$$d\theta_v = -2\pi \frac{\Delta u}{\lambda} = -\vec{k}_u \cdot \vec{v} dt. \quad (1.10)$$

This flow-induced phase shift is demonstrated in Figure 1-6 for both longitudinal and transverse basis functions.

In the notation of Eqs. 1.8 and 1.9, this uniform motion by  $\Delta u$  corresponds to a spatial convolution with a shifted delta function. The displacement probability is  $P(u, dt) = \delta(u - \Delta u)$ , whose Fourier transform is  $\tilde{P}(k_u, dt) = e^{-ik_u \Delta u} = e^{-i\vec{k}_u \cdot \vec{v} dt}$ . A

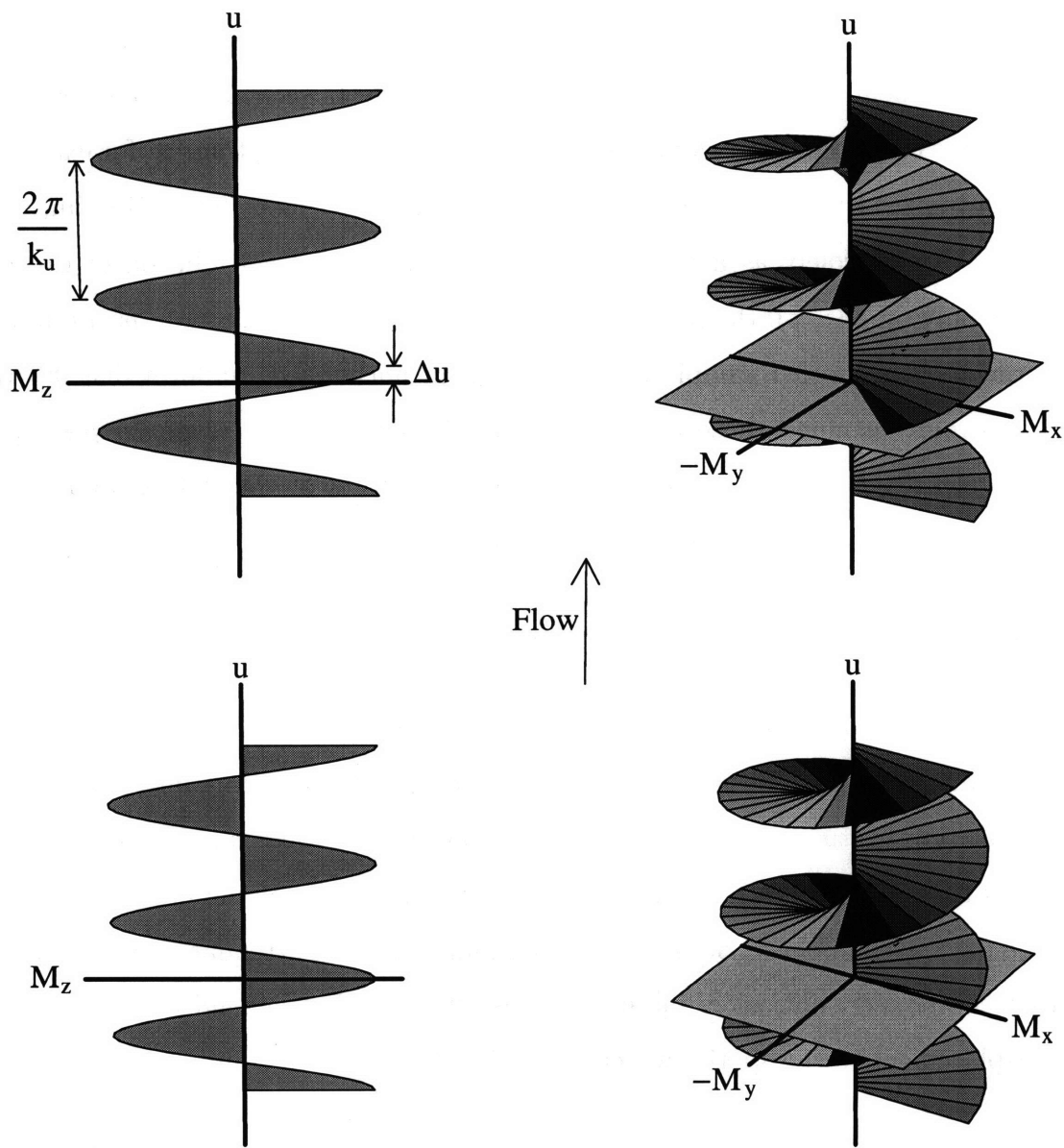


Figure 1-6: Flow-induced phase offsets for A) longitudinal and B) transverse magnetization gratings. Motion along the modulation axis causes a bulk displacement of the grating, incrementing the phase offset by  $-k_u \Delta u$ .

magnetization component modulated along  $u$  with wavenumber  $k_u$  thus acquires a global phase offset  $d\theta_v = -\vec{k}_u \cdot \vec{v} dt$ , in agreement with Eq. 1.10. As indicated by the dot product  $\vec{k}_u \cdot \vec{v}$ , a phase offset is induced only by motions along the modulation direction. Motion along an orthogonal direction displaces the grating sideways, and thus causes no phase shift relative to  $u = 0$ .

In the absence of a gradient field,  $k$  remains constant with time. Integration of Eq. 1.10 over a finite time interval  $\Delta$  then yields a flow-induced phase offset,

$$\theta_v = - \int_0^\Delta \vec{k}_u \cdot \vec{v} dt = -\vec{k}_u \cdot \vec{v} \Delta. \quad (1.11)$$

In the presence of an applied gradient field of strength  $g$ , on the other hand, the  $k$ -value grows linearly with time, producing a flow-dependent phase offset that accumulates with a quadratic time dependence in the presence of steady spatially uniform flow. If  $k(t)$  grows linearly with time as  $k(t) = k_0 + \gamma g t$  between a starting value  $k_0$  and a final value at time  $\delta$  of  $k_\delta = k_0 + \gamma g \delta$ , then integration yields the flow-induced phase offset,

$$\theta_v = - \int_0^\delta \vec{k}_u(t) \cdot \vec{v} dt = - \left[ \vec{k}_0 \delta + \gamma \vec{g} \frac{\delta^2}{2} \right] \cdot \vec{v} = - \frac{\vec{k}_0 + \vec{k}_\delta}{2} \cdot \vec{v} \delta. \quad (1.12)$$

Together, Eqs. [1.11] and [1.12] may be used to deduce the effects of flow on modulation components with constant or steadily growing wavenumbers, and are sufficient to analyze the velocity sensitivity of many standard gradient experiments. Echo experiments are frequently used to measure flow-dependent phase shifts, since these phase terms only arise in grating components modulated at  $k \neq 0$ .

### Flow-Sensitive Echo Experiments

Figure 1-7 demonstrates three common flow-sensitive experiments. Figs. 1-7A, B, and C depict a gradient echo experiment, a spin echo experiment, and a stimulated echo experiment, respectively. During the first gradient pulse of length  $\delta$ , the transverse modulation wavenumber grows from  $k_0 = 0$  to  $|k_{max}| = \gamma g \delta$ , resulting from Eq. 1.12 in a phase offset that grows quadratically with time, to reach a final magni-

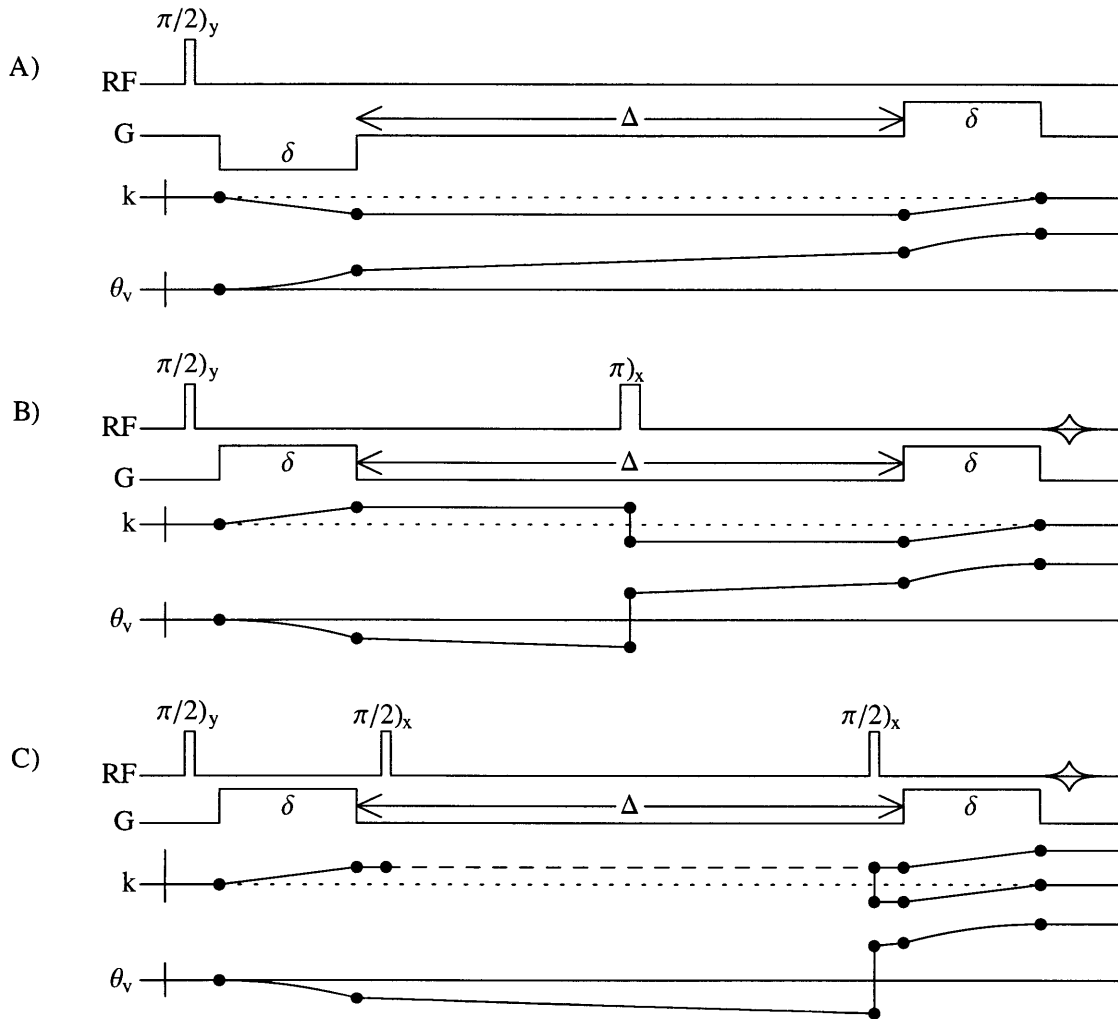


Figure 1-7: Motion sensitive gradient experiments, their corresponding  $k$ -trajectories, and their flow induced phase-offsets  $\theta_v$ . A) The gradient echo experiment, B) the pulsed gradient spin echo experiment (PGSE), and C) the stimulated echo experiment. Spins in all three experiments accrue the same flow-induced phase factor  $\theta_v = \exp[i\gamma\vec{g} \cdot \vec{v}\delta(\delta + \Delta)]$ , and the same diffusive attenuation factor  $\exp[-D\gamma^2g^2\delta^2(\Delta + 2\delta/3)]$ . As the final RF pulse of experiments B) and C) invert  $k$ ,  $\theta_v$  and the slope of subsequent  $\theta_v$  accumulation, the two gradient must have the same relative sign to form an echo, in contrast to experiment A) which requires gradient pulses of opposite sign. Note the quadratic time dependence of  $\theta_v$  during the intervals  $\delta$  when the gradients are on, versus the linear dependence during the interval  $\Delta$  between gradient pulses. RF phases have been chosen so that the only contribution to the phase offset is induced by displacement of the grating by bulk flow.

tude  $|k_{max}|\hat{u} \cdot \vec{v} \delta/2$ . During the delay  $\Delta$  between the end of the first gradient pulse and the beginning of the second,  $k$  remains constant, resulting from Eq. 1.11 in a further phase accumulation of magnitude  $|k_{max}|\hat{u} \cdot \vec{v} \Delta$  as the grating is displaced along the direction of flow. The second gradient pulse in each experiment refocusses the grating, unwinding the wavenumber linearly from  $-k_{max}$  to zero, which results in an observable signal and increments the phase offset further by  $k_{max}\hat{u} \cdot \vec{v} \delta/2$ . For all three experiments, the net phase offset induced by flow is thus,

$$\theta_v = \vec{k}_{max} \cdot \vec{v} (\delta + \Delta) = \gamma \vec{g} \cdot \vec{v} \delta (\delta + \Delta). \quad (1.13)$$

In the gradient echo experiment of Fig. 1-7A, the two gradient pulses must be applied with opposite sign in order to refocus the grating and produce a detectable signal. In the spin echo and stimulated echo experiments of Fig. 1-7B and 1-7C, however, the gradient pulses have the same sign, as the last RF pulse of each sequence simultaneously inverts the sign of  $k$ , the sign of the offset  $\theta_v$  and the slope of further flow-induced phase accumulation.

### Flow-Compensated Gradient Sequences

Figures 1-8A-1-8C show velocity-compensated gradient-echo experiments. To form an echo,  $k$  must return to zero. For velocity compensation,  $\theta_v$  must also return to zero at the end of the sequence: any gradient waveform that produces a time-dependence of  $k$  such that  $\int k(t)dt = 0$  will accrue no net flow-induced phase term. Many  $k$ -trajectories can be devised which satisfy these criteria, as for example, the sequence of Fig. 1-8A. A general class of flow-compensated sequences comprises sequences of gradient pulses each with the same duration but alternating signs, whose magnitudes vary as the binomial coefficients. The first two such sequences, with gradient amplitudes varying as  $[-1, +2, -1]$ , and  $[-1, +3, -3, +1]$ , are shown in Fig. 1-8B and 1-8C. A gradient profile with amplitudes varying as the binomial coefficients of a given order produces a  $k$ -trajectory which varies between extremes that also alternate in sign and whose relative magnitudes vary as the binomial coefficients of one order lower. The sum of these phase alternating binomial coefficients (and thus the integral of the  $k$ -trajectory

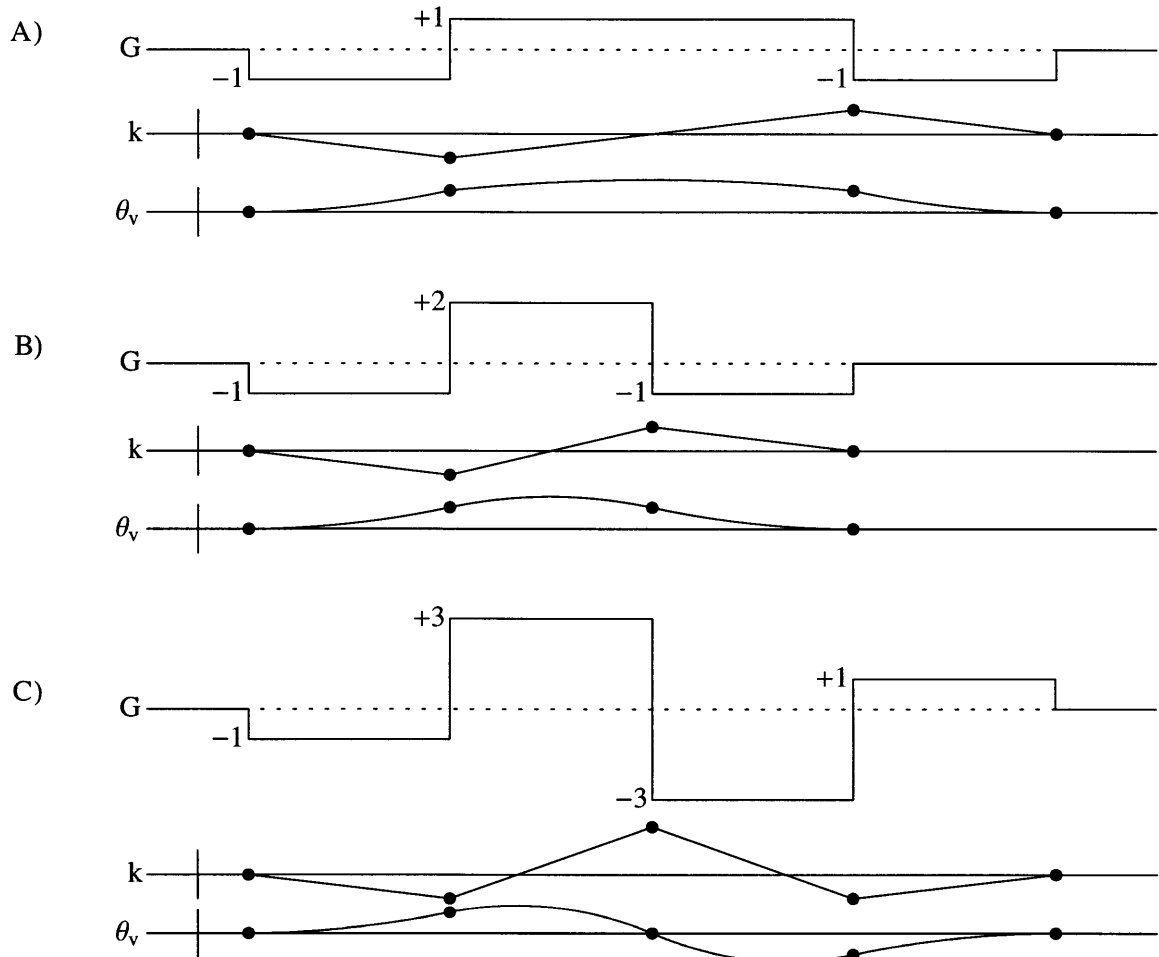


Figure 1-8: Velocity-compensated gradient profiles, with their corresponding  $k$ -space trajectories and flow-dependent phase factors. Both  $k$  and  $\theta_v$  return to zero at the end of each sequence, providing, respectively, for echo formation and overall flow compensation. A) A simple profile of constant gradient strength. B) and C), the first two sequences in the class of compensated profiles whose gradient strengths vary as binomial coefficients. While all three sequences are insensitive to uniform flow, they do suffer attenuation due to molecular diffusion, as described in the text.



with time) is zero, resulting in no overall phase shift due to flow.

### Extension to Bulk Acceleration

The sensitivity of pulse sequences to higher-order flow phenomena such as bulk acceleration is often treated with a moment expansion of the gradient waveform with respect to time [5]. It may also be extracted, however, by integrating the phase shift  $d\theta_v = -k \cdot \Delta u$  of Eq. 1.10. For the general case of  $\Delta u = (v_0 + at)dt$ , the phase shift may be integrated over time to yield a net phase shift,

$$\theta_v = -\vec{k} \cdot \left( \vec{v}_0 \Delta + \vec{a} \frac{\Delta^2}{2} \right), \quad (1.14)$$

during intervals of length  $\Delta$  during which  $k$  remains constant. Alternatively, for intervals  $\delta$  during which  $k$  changes linearly between the values  $k_0$  and  $k_\delta = k_0 + \gamma g \delta$ , integration yields,

$$\theta_v = -\frac{\vec{k}_0 + \vec{k}_\delta}{2} \cdot \vec{v}_0 \delta + \left( \frac{\vec{k}_0}{2} + \vec{k}_\delta \right) \cdot \vec{a} \frac{\delta^3}{3} \quad (1.15)$$

## 1.6.2 Diffusion

### Unrestricted Diffusion

In the case of unrestricted diffusion,

$$P(r, \tau) = \frac{1}{\sqrt{2\pi\sigma^2}} \exp\left(-\frac{1}{2} \frac{r^2}{\sigma^2}\right) \iff \tilde{P}(k, \tau) = \exp\left(-\frac{1}{2} k^2 \sigma^2\right), \quad (1.16)$$

where  $\sigma = \sqrt{2D\tau}$  for diffusion in one-dimension with diffusion constant  $D$ . Although physically diffusion does occur in 3 dimensions throughout the sample, gradient techniques are only sensitive to the motions along the grating modulation axis, which thus reduces the dimensionality of the problem. Equations 1.9 and 1.16 indicate that longitudinal and transverse grating components modulated at wavenumber  $k$  undergo attenuation by a factor  $\exp(-k^2 D dt)$  due to unrestricted molecular diffusion for time  $dt$ . This corresponds to convolution of the spatial modulation with a

gaussian centered at  $\Delta r = 0$ , whose width grows as the square root of time. Since this displacement probability is symmetric, the result is a pure attenuation of the modulation component, with no phase shift or change in wavenumber [6].

Just as the flow-induced phase shift of the last section was integrated over time to yield the net offset during a finite interval, so must the diffusive attenuation exponent be integrated to produce the overall diffusion-induced attenuation factor  $\exp[-D \int k^2(t) dt]$  along the  $k$ -trajectory of interest. For an interval  $\delta$  during which the  $k$ -value changes linearly with time from  $k_0$  to  $k_\delta = k_0 + \gamma g \delta$  due to evolution in a constant gradient field, the end result is an attenuation factor

$$A = \exp \left[ -D \frac{\delta}{3} (k_0^2 + k_\delta^2 + k_0 k_\delta) \right]. \quad (1.17)$$

During intervals  $\Delta$  where the wavenumber remains constant at  $k = k_0$ , the attenuation factor is  $\exp(-k_0^2 D \Delta)$ . For the other common case of an interval  $\delta$  with a linear  $k$ -trajectory between a value of zero at one end and  $k_{max} = \gamma g \delta$  at the other, the factor becomes  $\exp(-D k_{max}^2 \delta / 3) = \exp(-\gamma^2 g^2 D \delta^3 / 3)$ . For  $k$  trajectories that are not piecewise linear, as with shaped gradient pulses, the exponent  $-D \int k^2(t) dt$  must be integrated explicitly.

The gradient experiments of Figure 1-7, described above for their velocity-encoding properties, are also sensitive to diffusion. The diffusive attenuation factors for these experiments are easily determined by application of Eq. 1.17 to each linear section of the  $k$  trajectory. The gradient echo, spin echo, and stimulated echo experiments of Fig. 1-7A, 1-7B, and 1-7C, all produce the same diffusive attenuation factors. As  $|k|$  grows from zero to  $k_{max} = \gamma g \delta$  during each encoding pulse, or decreases from  $k_{max}$  to zero during the refocussing pulse, there is an attenuation  $\exp(-D k_{max}^2 \delta / 3)$ . During the interval  $\Delta$  of constant  $|k| = k_{max}$  between the gradient pulses, diffusion causes an attenuation  $\exp(-D k_{max}^2 \Delta)$ . Note that the wavenumber inversion in B and C has no effect on the attenuation factor as  $k^2$  remains constant. The overall diffusive attenuation of these three standard experiments is thus

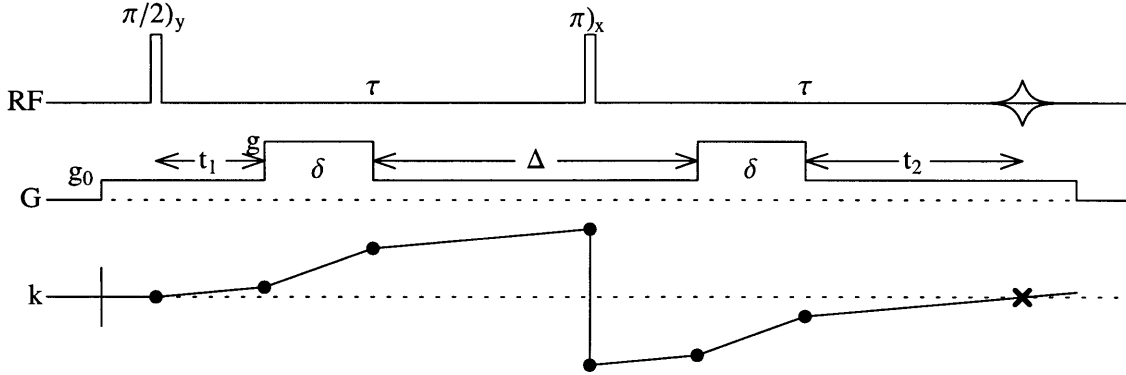


Figure 1-9: The PGSE experiment of Fig. 1-7B, with a constant gradient  $g_0$  present throughout the entire duration of the experiment, in addition to the standard gradient pulses.

$$A = \exp \left[ -Dk_{max}^2 \left( \Delta + \frac{2\delta}{3} \right) \right] = \exp \left[ -D\gamma^2 g^2 \delta^2 \left( \Delta + \frac{2\delta}{3} \right) \right]. \quad (1.18)$$

The gradient echo experiments of Figs. 1-8A-1-8C are all velocity compensated to have no net dependence on bulk flow. However, as the microscopic motions of diffusion are incoherent, it is not possible to refocus diffusive effects: the exponent of the attenuation factor contains an integral of  $k^2$ , which is always positive, so there is no way to compensate a sequence to eliminate diffusive losses entirely. Application of Eq. 1.17 produces the attenuation factors  $\exp[-4Dk_m^2\delta/3]$ ,  $\exp[-5Dk_m^2\delta/3]$ , and  $\exp[-8Dk_m^2\delta/3]$  for the sequences of Fig. 1-8A, Fig. 1-8B, and Fig. 1-8C, respectively, where  $k_m = \gamma g \delta$  is the wavenumber attained after the first gradient lobe of length  $\delta$  in each experiment. Clearly, in order to reduce diffusive losses, one must reduce either the excursion in  $k$  or the length of time over which the grating is present before refocussing. A Carr-Purcell cycle, for example, may be used in the presence of a constant field gradient to limit diffusive attenuation by restricting the maximum excursion in  $k$ .

As a final example of diffusive attenuation, Figure 1-9 depicts the pulsed-gradient spin echo experiment of Fig. 1-7B with an added constant gradient  $g_0$  that remains present for the entire duration of the sequence. By using Eq. 1.17 and a table of the

modulation wavenumber at each discontinuity in the  $k$ -trajectory, it is again straightforward to calculate the overall attenuation. The result is the standard attenuation factor [7],

$$A = \exp\left\{-\gamma^2 D \left[ g^2 \delta^2 \left( \Delta + \frac{2}{3} \delta \right) + \frac{2}{3} g_0^2 \tau^3 - g g_0 \delta (t_1^2 + t_2^2 + \delta(t_1 + t_2) + \frac{2}{3} \delta^2 - 2\tau^2) \right] \right\}, \quad (1.19)$$

where the intervals  $\Delta$ ,  $\delta$ ,  $t_1$ ,  $t_2$ , and  $\tau$  are all defined in the figure. (Note that  $\Delta$  has been defined here as the delay between the end of the first gradient pulse and the beginning of the second, in contrast to the standard definition as the spacing between the beginnings of the two pulses. This accounts for the terms  $(\Delta + 2\delta/3)$  above in place of the  $(\Delta - \delta/3)$  terms that appear in [7].)

The attenuation factors derived above are correct only for the case of unrestricted molecular diffusion. If diffusion is restricted by, for example, sample walls, these spatial features will be reflected in the initial  $\rho(r, 0)$  and  $\tilde{\rho}(k, 0)$ , which, as in the imaging experiment, will then include not only the grating imposed by gradient evolution, but the sample geometry as well. While it is tempting to use the above attenuation factors separately on each component of  $\tilde{\rho}(k)$ , this approach is in fact only correct for short diffusion times before diffusion becomes restricted by the bounding walls. For longer times the displacement probability is no longer well represented by a gaussian function of  $\Delta r$ , as diffusion cannot proceed further past the bounding wall. The displacement probability loses its spatial invariance and a complete analysis requires full integration with  $P(r|r', \tau)$ , which takes into account the full geometry of the bounding regions. By contrast, a spatially-limited spin-density produced by selective excitation of magnetization in a small region of an infinite-extent sample may in fact be treated correctly with the  $k$ -dependent attenuation factors of this section, as spins in each  $k$ -component then freely diffuse over an infinite extent with no interference by boundary walls.

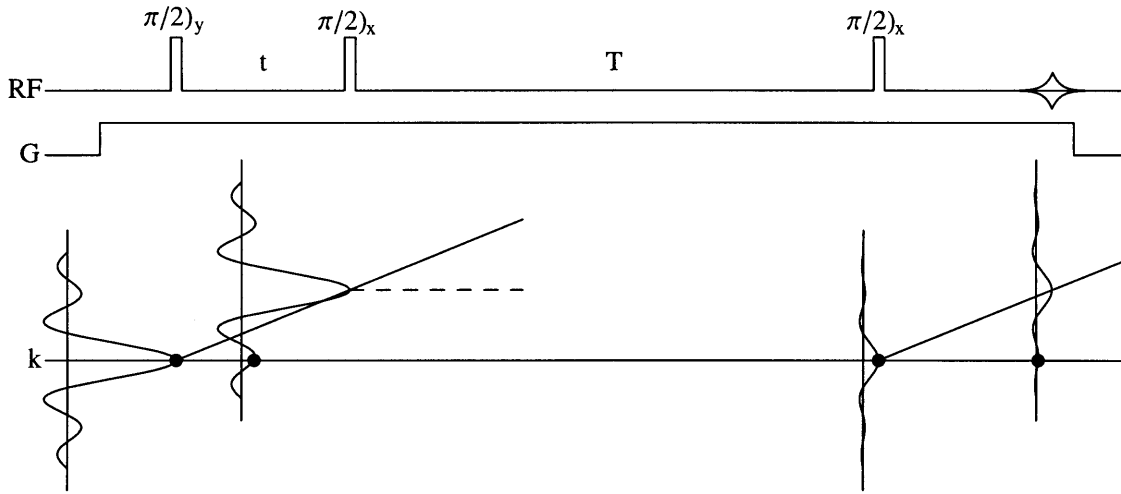


Figure 1-10: A stimulated echo experiment demonstrating bounded diffusion. The amplitude of the  $k = 0$  components is the same for the distributions before and after the  $T$  delay, as the net magnetization is conserved.

### Bounded Diffusion

In the extreme limit of fully bounded diffusion, analytical results may again be derived without prior knowledge of the bounding geometries. For a given bounded volume (such as a fluid-filled pore with solid walls), the stimulated echo diffusion experiment is shown in Fig. 1-10. At the beginning of the experiment, before gradient evolution occurs,  $\tilde{\rho}(k)$  reflects the wall geometry of the bounding region. Gradient evolution for time  $\delta$  shifts the center of this distribution to  $k_\delta = \gamma g \delta$ , to produce  $\tilde{\rho}(k + k_\delta)$ . During the interval  $\Delta$ , bounded diffusion occurs. In this limit, the spatial extent of the bounding region is small compared with the diffusion length scale  $\sigma = \sqrt{2D\Delta}$ , so that on average, a given molecule has traversed the bounding region many times, and is thus equally likely to be found anywhere within that region [8]. There is no longer any variation in the magnetization throughout the bounding region: the gradient-induced modulation had been effectively eliminated by bounded diffusion. The distribution of magnetization thus still has the same form  $\tilde{\rho}(k)$  as at the beginning of the experiment. However, as the net magnetization inside the bounding region must be conserved in the absence of relaxation, the amplitude of this distribution is  $\tilde{\rho}(+k_\delta)$ , the dc-component present after the first gradient pulse. The second period of gradient

evolution again shifts this distribution, resulting in a detected  $k = 0$  component of amplitude  $\tilde{\rho}^2(+k_\delta)$ . Fully bounded diffusion thus provides a potential probe of the bounding geometry, though it should be noted that each measurement contains the net signal over the full sample volume, with contributions from all bounded regions, which may have different geometries.

## 1.7 Generalizations to Spectroscopy

The echo experiments of Figs. 1-4 and 1-5 were depicted as occurring in the presence of a constant, static gradient field varying along the  $\hat{u}$  direction. The combination of RF pulses and intervals of evolution in the gradient gave rise to magnetization components modulated along  $\hat{u}$  with wavenumbers  $k_u$  easily determined at all times. The local phase  $ku + \theta$  at all locations was determined by tracking changes in  $k$  and  $\theta$  during the course of the sequence, with an echo occurring whenever a grating component passed through  $k = 0$ . The  $k$ -space formalism presented thus far technically describes the phase evolution with time only due to linear static field gradients, and would thus be strictly applicable only to echo experiments carried out under these conditions. In practice, however, the results predicted for these experiments can easily be generalized to correctly describe refocussing of other inhomogeneous interactions that remain fixed throughout the length of the experiment, such as static field inhomogeneities or chemical shift differences. For example, the results of the echo experiments may be generalized to a refocussing of static field-inhomogeneities of arbitrary spatial dependence. Alternatively, the  $k$ -space modulation produced by a pulse cycle in the presence of a static gradient may be used to calculate the frequency-selectivity of the cycle, whether the true source of frequency dispersion is an applied gradient or chemical shift differences of spectral lines in the absence of a gradient.

In the case of linear gradients, the precession frequency of different spin packets, and thus the accumulated phase at any given time, varies as a function of position along the gradient direction. For a general (i.e. not necessarily linear) inhomogeneity in the  $B_0$  field, this variation is a function of the local field strength, while for spin

packets that differ on the basis of chemical shift, it is instead a function of the nuclear shielding parameter  $\sigma$ . Position, field strength, or shielding parameter can thus be used equivalently as reciprocal coordinates for defining a  $k$ -analog in order to treat echoes formed by refocussing linear gradients, more general field inhomogeneities, or chemical shift differences. Regardless of the nature of the inhomogeneous interaction being refocussed,  $\theta$  incorporates the overall RF-induced phase shifts that apply to all spins in the sample, while the  $k$ -analog tracks the differential phase accumulation of separate spin packets as a function of the appropriate reciprocal coordinate. The phase offset  $\theta$  is simply the acquired phase of a spin packet that is perfectly on-resonance, or equivalently, in a position where the local field deviation due to a field gradient or other inhomogeneity is zero. The  $k$ -value or  $k$ -analog then keeps track of other phase offsets as a function of position, field strength, or chemical shift value.

### Re-Parametrized Basis Functions

All that is thus required to generalize the formalism is a new parameterization of the three basis functions of Fig. 1-1 — the longitudinal amplitude modulation and the transverse phase modulations of either handedness. When dealing with linear gradient fields, it is natural to decompose the sample magnetization into longitudinal sinusoids and transverse magnetization helices, all varying spatially along the gradient axis. If the variations in  $B_0$  field are not linear, however, these spatial modulations become distorted, as regions with stronger local field gradients are wound tighter than regions with better field homogeneity. It is then simplest to remap the sample into modulations that vary as a function of the local field strength. These modulations have the same form as those depicted in Fig. 1-1, with the spatial coordinate  $u$  replaced by the local field strength. When there is a linear mapping between field strength and position — in the presence of a linear field gradient — these field-strength dependent modulations revert to the previous spatial grating components.

More general modulation components are those that vary as a function of resonance offset frequency. This offset may arise from  $B_0$  field inhomogeneities, giving rise to the basis functions described above, or may result from chemical shift differences

between sample constituents. In this case there is no longer a physical spatial axis along which the grating components vary, but it is nonetheless useful to decompose the sample into modulations varying as a function of offset. Free evolution of a starting uniform transverse magnetization state for times  $\tau$  and  $2\tau$  results in transverse magnetization states  $\exp(i\Delta\omega\tau)$  and  $\exp(i\Delta\omega 2\tau)$ , respectively. Longer evolution produces transverse modulations that vary more rapidly as a function of the offset  $\Delta\omega$ . Instead of tracking the spatial frequency of a modulation, the new  $k$ -analog—with units of time—instead denotes a wavenumber in frequency space. As before, RF pulses mix the transverse and longitudinal states, producing more complex gratings.

At any time during an experiment, the distribution of  $k$ -analog components is merely a Fourier series — a decomposition of the magnetization (both transverse and longitudinal) into modulations with fast or slow variations as a function of resonance offset frequency. Simply by summing the distribution of basis functions with the proper amplitudes and phases, it is straightforward to derive the frequency dependence of a pulse sequence, regardless of the physical source of the frequency dispersion.

As an example, Fig. 1-11 depicts a jump return sequence [9], with its corresponding Fourier series representation. Summing over the  $k$ -analog values using the amplitude and phase factors from the transformation rules of Table 1.1, yields the state

$$\begin{aligned} & \left[ \cos \alpha \sin \alpha - \sin \alpha \cos^2(\alpha/2) \right] e^{i(+\Delta\omega\tau+\pi/2)} \\ & \quad + \left[ \sin \alpha \sin^2(\alpha/2) \right] e^{i(-\Delta\omega\tau+\pi/2)} \\ & \quad + \left[ \cos^2 \alpha - \sin^2 \alpha \sin(\Delta\omega\tau - \pi/2) \right] \hat{z}, \end{aligned} \tag{1.20}$$

which is identical to the product operator result after the spin operators have been converted to their equivalent magnetization components.

Any series of hard RF pulses and delays may be analyzed equivalently in the cartesian basis set  $[M_x, M_y, M_z]$  or the  $k$ -analog basis set  $\exp i(\pm\Delta\omega t + \theta)$ ,  $\sin(\Delta\omega t + \theta)\hat{z}$ . The  $k$ -analog formalism is a useful tool to demonstrate which Fourier series components are formed in the course of an experiment, and yields graphical insight into the spin dynamics. The coefficient of each line may be determined by accumulating amplitude and phase factors from Table 1.1 along the corresponding trajectories.



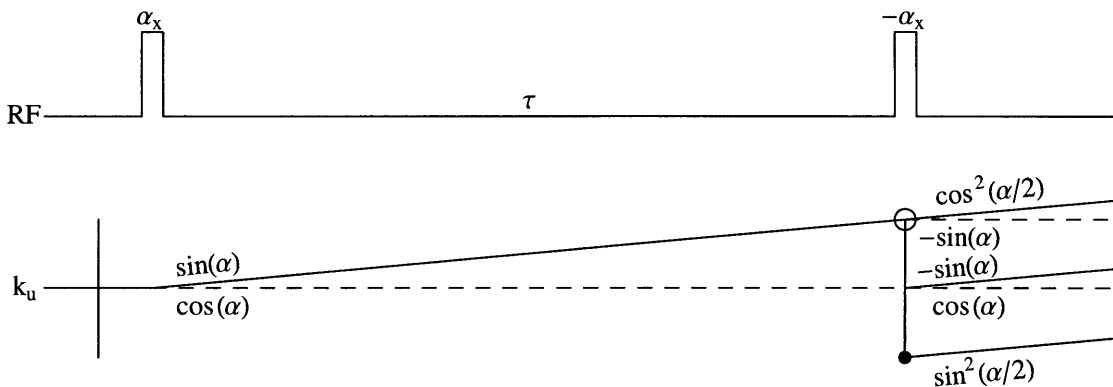


Figure 1-11: The jump-return experiment, with its corresponding  $k$ -analog description. The lines in  $k$  most generally denote magnetization components modulated as a function of  $\Delta\omega\tau$ , thus producing a Fourier series describing the frequency response of the sequence. If the offset  $\Delta\omega$  were caused by evolution in a linear field gradient, these modulation components would revert to those varying as a function of  $k_u u$ , and summing the Fourier series would yield the spatial selectivity of the experiment.

### 1.7.1 Selective Excitation

Often in NMR the Fourier transform of the pulse sequence is used to determine its approximate frequency response. The  $k$ -analog formalism provides a more correct description, but reduces to the standard approach when the appropriate simplifying assumptions are made.

#### Example — the DANTE Sequence

Figure 1-12 shows a DANTE sequence [10], a series of short hard RF pulses separated by equal time intervals  $\tau$ . The  $k$ -space diagram demonstrates that just after the  $n$ th pulse, Fourier series components are present that are modulated at  $m\Delta\omega\tau$ , with  $m$  taking integer values between  $(n - 1)$  and  $-(n - 1)$ . If the DANTE sequence is performed in the presence of a linear field gradient, and followed by a  $\pi$  pulse to invert all  $k$  values, a series of echoes separated by  $\tau$  results as each grating component is sequentially refocused to  $k = 0$ . This technique is exploited in the DUFIS [11] and BURST [3, 12] family of imaging sequences where phase encoding is incremented between sequential echoes. The  $k$ -space picture gives an immediate understanding of how echo formation proceeds in these experiments.

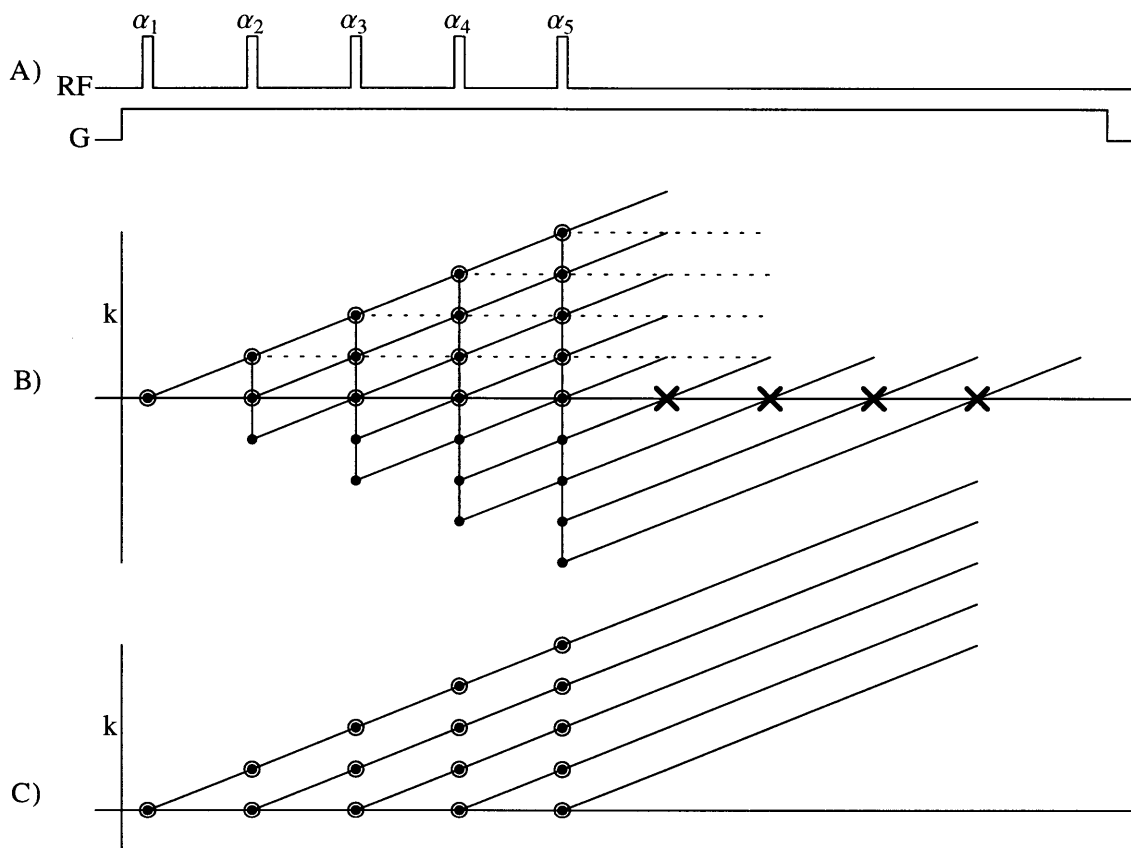


Figure 1-12: A) A DANTE sequence, composed of equally spaced RF pulses. B) The complete  $k$  space diagram. The lines in  $k$  may be summed in a Fourier series to yield the complete spatial dependence of magnetization throughout the sample. More generally, the  $k$ -analog picture correctly describes the frequency dependence of transverse and longitudinal magnetization as a function of resonance offset  $\Delta\omega$ , whether the offset is produced by a field gradient or chemical shift. C) The simplified  $k$  space diagram consistent with the small angle approximation. The resulting Fourier series simply corresponds to the Fourier transform of the pulse sequence.

From the RF transformations of Table 1.1, a given component of wavenumber  $m$  just after each RF pulse may be simply related to the three components with wavenumbers of the same magnitude just before the pulse. These components in turn have a one-to-one correspondence—through gradient or chemical shift-evolution—with the states at the beginning of the interval, just after the previous pulse. For a string of RF pulses of nutation angle  $\alpha_n$ , all with the same phase  $x$ , the  $m$ th transverse and longitudinal Fourier series coefficients after the  $n$ th pulse— $A_m^n$  and  $A_{z,m}^n$ —may be determined from the previous coefficients by the recursion relations,

$$\begin{aligned} A_m^n &= A_{m-1}^{n-1} \cos^2(\alpha_n/2) - A_{(-m-1)}^{n-1} \sin^2(\alpha_n/2) - A_{z,|m|}^{n-1} \sin(\alpha_n) \frac{\epsilon_m}{2}, \\ A_{z,m}^n &= \left[ A_{m-1}^{n-1} + A_{(-m-1)}^{n-1} \right] \frac{\sin(\alpha_n)}{\epsilon_m} + A_{z,m}^{n-1} \cos(\alpha_n), \end{aligned} \quad (1.21)$$

where  $\epsilon_m = 1 + \delta_m$ . Initial conditions require that  $A_{z,m}^0 = \delta_m$  and that all  $A_m^0 = 0$ . For a train of RF pulses all along  $x$ , the phases of all coefficients in Eq. 1.21 are  $\pi/2$ , up to a sign which has been incorporated in the recursion relations. If different RF phases were used, it would be necessary to separately track the magnitudes and phase offsets of each grating component in accordance with Table 1.1.

The resulting dispersion in  $k$ -values yields the Fourier series for the longitudinal and transverse magnetization components after the  $n$ th pulse,

$$\begin{aligned} M_{long.}(\Delta\omega) &= \sum_{m=0}^{n-1} A_{z,m}^n \cos[m\Delta\omega\tau], \\ M_{trans.}(\Delta\omega) &= \sum_{m=-(n-1)}^{n-1} i A_m^n e^{im\Delta\omega\tau}. \end{aligned} \quad (1.22)$$

### The Small Angle Approximation

If the approximation is made that each pulse in the train has a small flip angle, and the transformation amplitudes are calculated only to first order in the flip angle, then the  $k$ -space grating reduces to the greatly simplified diagram of Fig. 1-12C. In this approximation, the equilibrium longitudinal magnetization acts as an inexhaustible source of new unmodulated magnetization, always maintaining its full intensity at  $M_z = M_0$ , since  $\cos \alpha_n \approx 1$ . From this source, each RF pulse creates transverse

magnetization, producing a  $k$  space line that grows from  $k = 0$ , whose amplitude is simply weighted as  $\sin(\alpha_n) \approx \alpha_n$ , and whose phase is  $-\pi/2 + \phi_n$ . These lines remain unmixed by later RF pulses, and simply continue to grow in  $k$  value throughout the duration of the sequence, since the terms associated with  $k$  inversions and transformations to longitudinal gratings all enter to higher order in the small flip angle  $\alpha_n$ . The result is a greatly simplified  $k$ -space picture, which corresponds to the Fourier series for magnetization components,

$$\begin{aligned} M_{long.}(\Delta\omega) &= 1, \\ M_{trans.}(\Delta\omega) &= -i e^{i(n-1)\Delta\omega\tau} \sum_{m=0}^{n-1} \alpha_m e^{-i[m\Delta\omega\tau]} e^{i\phi_m}. \end{aligned} \quad (1.23)$$

The transverse magnetization is thus proportional to the Fourier transform of a train of  $n$  delta functions separated in time by  $\tau$ , and weighted with the complex coefficients  $\alpha_m \exp(i\phi_m)$ . In other words, in the small flip angle approximation, the frequency selectivity of the pulse sequence is simply equal to the Fourier transform of the pulse sequence in the time domain, where the end of the pulse sequence is defined as  $t = 0$ . For a DANTE sequence composed of  $N$  equivalent hard pulses, the pulse sequence may be viewed as an infinite train of delta functions separated by intervals  $\tau$ , times a rectangle function of length  $N\tau$ . The Fourier transform of this sequence yields an infinite train of delta functions separated by frequency units of  $1/\tau$ , convolved with a narrow sinc function whose first zero crossings fall at frequencies of  $\pm 1/(N\tau)$ . The frequency selectivity of the DANTE sequence is thus approximately a train of narrow sinc functions [5].

The small flip-angle Fourier series approximation has been used to design or analyze the frequency response of many selective excitation sequences composed of hard pulses. Notable examples include DANTE [10], solvent suppression sequences with pulses weighted as binomial series coefficients [13]–[15], or with other weightings [16] in order to alter the width or shape of the null regions. By appropriately choosing RF pulse amplitudes and phases, it is possible to tailor the production of lines in  $k$  space in order to produce a desired spatial profile, or more generally, a desired frequency selectivity. It is, for example, possible to create a frequency selectivity that is approx-

imately a square wave, so that spins at all offsets are excited with uniform intensity, but alternating sign [17, 18]. The small-flip angle approximation inherent in Eq. 1.23 makes the design problem particularly straightforward, although for quantitatively correct results with practical flip angles, the full Fourier series coefficients should be calculated through use of the RF transformations of Table 1.1.

### Frequency Response of Continuous RF Waveforms

If the interval  $\tau$  between delta function RF pulses shrinks to zero, the approximate Fourier analysis of Eq. 1.23 may be extended to an analysis of the frequency response of a continuous RF waveform. In the limit as  $\tau$  approaches zero, the Fourier series sum of Eq. 1.23 becomes a Fourier transform integral,

$$M_{trans}(\Delta\omega) = -i \int_{-T}^0 dt \alpha(t) e^{-i[\Delta\omega t]} e^{i\phi(t)}, \quad (1.24)$$

where the end of the RF waveform is defined as time  $t = 0$ . In the small angle approximation, the frequency dependence of transverse magnetization excited by a shaped pulse or by any RF waveform of finite extent may thus be determined simply by taking the Fourier transform of the RF waveform  $\alpha(t) \exp(i\phi(t))$ . This result is widely used, and has been previously derived from the Bloch equations with the small angle approximation that  $M_z \approx M_0$ ,  $\sin \alpha \approx \alpha$  [10], or as the first order result of a full perturbation analysis [19]. It can be used to determine the selectivity of shaped pulses as a function of offset frequency or—if a linear gradient is used to map resonance offset to position—as a function of position in the sample. To describe experiments whose gradient sequences vary with time, further modifications have been made which determine the spatial selectivity from the Fourier transform of a weighted  $k$  space trajectory [20, 21].

The standard Fourier approach for determining the frequency selectivity of a pulse sequence has two major limitations in its applicability, based on the approximations implicit in the derivation. The first of these, the small flip angle approximation, has already been discussed. While the Fourier transform of the pulse sequence may be useful in qualitatively determining the frequency profile, correct quantitative results

cannot be expected in cases where the bulk magnetization is significantly perturbed from its equilibrium orientation along  $z$ . For large flip angles, the correct  $k$  space diagram becomes more complex, as each RF pulse performs mixing between modulation components. Nonetheless, for pulse sequences comprising a series of hard pulses, the frequency response may be determined analytically from the Fourier series of Eq. 1.22, if the Fourier series coefficients have been determined by the history of RF transformations using Table 1.1, as in Eq. 1.21 and Fig. 1-12B.

The second important approximation inherent in the Fourier transform approaches is a hard pulse approximation. Each delta function RF pulse is assumed to be strong enough that it effects a rotation about an axis in the transverse plane. This allows the RF-induced rotations and the gradient or offset-induced  $z$ -rotations to be separated into sequential evolution periods. In reality, if the resonance offset is not negligible compared to the RF nutation frequency, the rotations cannot be separated, but result in a net rotation about a tilted effective axis oriented along the vector sum of the two individual contributions. The transformations of Table 1.1, the starting point for the derivations presented above, treat only on-resonance RF rotations about purely transverse axes. This produces a potential source of error in determining the frequency selectivity of a sequence, since those spins which evolve at high resonance offset values during the intervals between pulses will also experience RF rotations about effective axes that are tilted away from the transverse plane. If the resonance offset is effected by a field gradient, this limitation may be averted by applying the gradient only between RF pulses: All spins then experience on-resonance rotations, interspersed between periods of gradient-induced  $z$ -rotations.

The exact frequency response of a pulse sequence may always be determined by numerical solution of the full Bloch equations, which incorporate rotations about the tilted effective axes. However, unless off-resonance pulses must be analyzed explicitly, the  $k$ -space formalism yields identical results by tracking all Fourier components built up by the pulse sequence, which providing more physical insight than a numerical Bloch equation solution.

## 1.8 Gradient Selection of Multiple Quantum Coherence Pathways

The results of the previous sections pertain to a single-spin system, in which case multiple quantum coherences (MQC's) cannot arise. When the system under study involves chemically distinct interacting spins, however, coupling gives rise to multiple quantum coherences. Field gradients are often used in experiments involving MQC's, as a means of selecting certain coherence pathways and suppressing others. Since MQC's can no longer be represented by classical magnetization components, the  $k$ -space picture of previous sections must be modified to account for the spatial effects of gradients on MQC's.

### 1.8.1 Background

The product operator formalism [22] provides a convenient basis set to describe the density matrix of a spin system in the presence of MQC's. While the standard cartesian product operators  $I_x$ ,  $I_y$ , and  $I_z$  for each spin in the system are commonly used to predict the results of a pulse sequence, another useful and complete basis set is comprised of  $I_+$ ,  $I_-$ , and  $I_z$ , where  $I_{\pm} = I_x \pm iI_y$ . While the cartesian operators transform somewhat more conveniently under RF-induced rotations, the raising and lowering operators are conserved during periods of free precession, and simplify the treatment of multiple quantum coherence. In order to calculate the effects of RF pulses, z-rotations during free evolution, and J couplings, it is most convenient to rewrite the standard operator transformations [22] using the raising and lowering operators  $I_+$  and  $I_-$  in place of the cartesian operators  $I_x$  and  $I_y$ :

$$\begin{aligned}
\text{RF Pulses : } I_{\pm} &\xrightarrow{\alpha\phi} I_{\pm} \cos^2\left(\frac{\alpha}{2}\right) + I_{\mp} e^{\pm i2\phi} \sin^2\left(\frac{\alpha}{2}\right) \pm I_z e^{\pm i(\phi+\pi/2)} \sin(\alpha), \\
I_z &\xrightarrow{\alpha\phi} I_z \cos(\alpha) + \frac{i}{2} \sin(\alpha) (I_+ e^{-i\phi} - I_- e^{+i\phi}), \\
\text{Free Evolution : } I_{\pm} &\xrightarrow{\phi_z} I_{\pm} e^{\mp i\phi},
\end{aligned} \tag{1.25}$$

$$\text{J Coupling : } I_{\pm} \xrightarrow{J} I_{\pm} \cos(\pi Jt) \mp i 2I_{\pm} S_z \sin(\pi Jt).$$

Multiple quantum coherences comprise outer products of the single-spin operators, with the coherence number  $p$  defined as the difference between the number of  $I_+$  and  $I_-$  operators in the combination. In general, multiple-quantum coherences of order  $p$  are defined [22] as

$$\begin{aligned}
\{pQC\}_x &= \frac{1}{2}(I^{[+p]} + I^{[-p]}), \\
\{pQC\}_y &= \frac{1}{2i}(I^{[+p]} - I^{[-p]}),
\end{aligned} \tag{1.26}$$

where  $I^{[+p]}$  denotes a given product operator of coherence number  $p$ , and  $I^{[-p]}$  denotes the corresponding operator where all component single-spin  $I_{\pm}$  terms have been reversed to  $I_{\mp}$ . With these definitions,  $\{pQC\}_x$  transforms to  $\{pQC\}_y$  in a right-handed sense under a rotation about the z-axis. The overall precession frequency is determined by adding or subtracting each spin's individual precession frequency, depending on whether that spin contributes a raising or a lowering operator to the combination.

## 1.8.2 Homonuclear Experiments

Regardless of the number of spins contributing to the product, a homonuclear operator of coherence number  $p$  accumulates a net phase of  $e^{-ip\phi}$  under a  $\phi_z$  rotation [23, 24], as each single spin operator contributes independently to the overall phase factor in accordance with Eq. 1.25. Under an  $I_z$  hamiltonian such as the chemical shift or a field gradient, an operator with  $p = 2$  thus evolves twice as rapidly as one with  $p = 1$ , while a  $p = -1$  state evolves in the opposite sense. If a field gradient of magnitude  $G_u$  is present, an operator of coherence number  $p$  accumulates a spatially-dependent phase factor  $\exp(iu\Delta k_u)$ , where



$$\Delta k_u = -p\gamma \int G_u dt. \quad (1.27)$$

This phase factor differs from that of Eq. 1.1 by the inclusion of the multiplicative factor  $-p$ . The geometric interpretation of this phase factor is also somewhat different from the  $k$ -value of Eq. 1.1, as it does not correspond to the wavenumber of a physical magnetization grating in  $[M_x, M_y, M_z]$ . Nonetheless, the overall spatial dependence of the system may be inferred by the combination of  $k$ -values for operators at each coherence number  $p$ .

Fig. 1-13A depicts a COSY experiment, with gradients incorporated to perform P/N type selection [25]. Neglecting RF-phase factors, and the amplitude factors arising from chemical shift and J-coupling, the desired transfer in the cartesian operator basis is

$$I_z \xrightarrow{\pi/2} I_y \xrightarrow{t_1} I_x S_z \xrightarrow{\pi/2} I_z S_x \xrightarrow{t_2} S_y. \quad (1.28)$$

Decomposing the cartesian operators into raising and lowering operators yields the standard coherence-pathway diagram of Fig. 1-13B. Alternatively, the  $I_{\pm}$  basis set may be used from the start, with the RF-induced mixing between states of different coherence number determined through application of the transformations of Eq. 1.25.

In an N-type spectrum, chemical shift evolution occurs in an opposite sense during  $t_1$  and  $t_2$ , while a P-type experiment measures evolution in the same sense during the two intervals. As the NMR experiment is constructed to detect only  $p = -1$  operators, the desired N-type coherence pathway thus has coherence number  $p = +1$  during  $t_1$  and  $p = -1$  during  $t_2$ . Since chemical shift evolution and gradient evolution are both described by  $I_z$  hamiltonians, the two interactions commute and may thus be considered independently. Just like the chemical shift, gradient evolution also occurs in an opposite sense during the intervals of an N-type experiment. Application of gradient pulses of the same sign—one during each evolution interval—can thus be used to select the desired N-type pathway, as shown in Fig. 1-13C, which depicts only those coherence pathways producing  $p = -1$  during  $t_2$ , as this is the only coherence detected. The gradient evolution is refocussed by the reversal of coherence number in

the N-type pathway, while the P-type pathway is eliminated by two periods of equal gradient evolution. Undesired axial peaks excited by the second RF pulse are also suppressed by the gradient sequence. They arise from longitudinal magnetization left by the first pulse or created by  $T_1$  relaxation during  $t_1$ , and are unaffected by the first gradient pulse, but suppressed by the second.

Fig. 1-13D depicts a modified coherence pathway diagram which superimposes the effects of gradient evolution on the standard coherence pathway diagram, thus separating density matrix components on the basis of coherence number  $p$  as well as the value of the spatially-dependent phase factor  $k$ . In this diagram, the only observable pathway (with  $p = -1$  during  $t_2$ ) that is refocussed to  $k = 0$  corresponds to the N-type signal.

As a consequence of the transformations of Eq. 1.25, some general statements may be made about the allowable structure of coherence pathway diagrams such as that in Fig. 1-13D. Any line with given values of  $p$  and  $k$  is mirrored by a symmetrically-formed line at  $-p, -k$ . Regardless of RF pulse-lengths and phases, the two lines always have the same magnitudes, while their relative phases are determined by the history of RF phases used in creating those lines.

From Eq. 1.25, an RF pulse of any phase transforms the starting  $I_z$  state into single quantum operators with equal magnitudes  $\sin(\alpha)/2$ . Gradient evolution modulates the states of opposite  $p$  value in opposite senses, resulting in inverse  $k$  values. Chemical shift induces a relative phase shift between the two lines, and J-coupling gives rise to two-spin, single quantum operators  $I_{\pm}S_z$ . The next RF pulse acts independently on each single spin operator, and leaves  $k$  unchanged, but alters  $p$  symmetrically. For example, the state  $I_+S_z \exp(-iku)$  transforms to  $I_-S_- \exp(-iku)$  with the same magnitude as the transformation from  $I_-S_z \exp(+iku)$  to  $I_+S_+ \exp(+iku)$ . The result is purely symmetric pairings. Further periods of gradient evolution or RF transformations have the same effect, never breaking the symmetry of coherence pathway trajectories. Each state of coherence number  $p$  and spatial phase factor  $+k$  thus appears in concert with a state of equal magnitude with coherence number  $-p$  and phase  $-k$ .

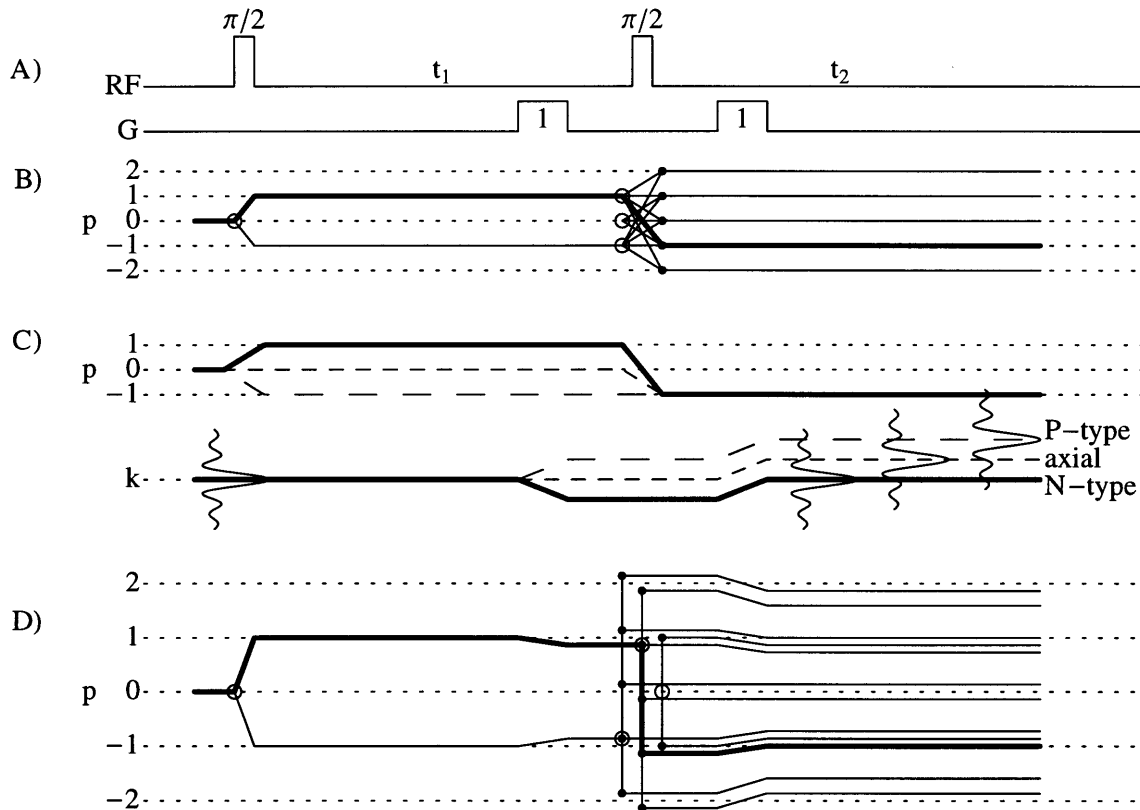


Figure 1-13: A COSY experiment using pulsed gradients for coherence pathway selection. A) The pulse sequence. B) Standard coherence pathway diagram, showing all transfers, with the refocused N-type pathway depicted in bold. The only observable pathways are those with  $p = -1$  during the detection period  $t_2$ . C) Simplified coherence pathway diagram of observable pathways only, with their corresponding spatially dependent  $k$ -values induced by gradient evolution. Note the varying slope of  $k$ -accumulation during the first gradient pulse. The second gradient pulse refocusses only the N-type pathway to  $k = 0$ , while suppressing the other two pathways. The spatial distributions  $\tilde{\rho}(k)$  have been convolved with the gradient-induced lines to demonstrate the approximate suppression factors of the sequence. D) A modified coherence pathway diagram that tracks both  $p$  and  $k$ . The lines in the immediate vicinity of each  $p$  value share that coherence number, but have different  $k$  values. Each line of coherence number  $+|p|$  and spatial phase factor  $-k$  is accompanied by a line of equal magnitude at  $-|p|$  and  $+k$ . These symmetrically formed lines, taken together, produce  $|p|$ -quantum coherences modulated in spatial helices of wavenumber  $+k$ , in analogy with the transverse magnetization helices of earlier sections. RF pulses transform the starting operator states marked by open circles into final states marked with filled circles.

Combination of these symmetrically-formed operators from the coherence pathway diagram yields multiple quantum coherences as defined in Eqs. 1.26. The symmetric lines combine as

$$\begin{aligned}
& I^{[+p]}e^{-i(ku+\theta)} + I^{[-p]}e^{+i(ku+\theta)} \\
&= (I^{[+p]} + I^{[-p]}) \cos(ku + \theta) - i(I^{[+p]} - I^{[-p]}) \sin(ku + \theta) \quad (1.29) \\
&\propto \{pQC\}_x \cos(ku + \theta) \quad + \{pQC\}_y \sin(ku + \theta) ,
\end{aligned}$$

where  $2\theta$  is an arbitrary phase between the two product operator terms, which is determined by the history of the RF phases employed in the pulse sequence. For single-spin states with  $p = \pm 1$ , or  $p = 0$ , these combinations simply reproduce the transverse and longitudinal gratings of earlier sections.

For systems composed of more than one spin, however, Eq. 1.29 corresponds to a spatial helix of the corresponding MQC. The wavenumber and sense (right or left handed) of the helix is determined by the  $k$ -value of the operator with negative coherence number. The relative phases of the two operators determines only the phase offset of the resulting modulation. In summary, combination of the two lines  $[+p, -k]$  and  $[-p, +k]$  in the coherence pathway diagram forms a spatial helix of the corresponding  $p$ -quantum coherence, with spatial wavenumber  $+k$ .

Returning to Fig. 1-13D, it is straightforward to read off all modulations present in the sample at any time during the course of the experiment. At the end of the experiment, only the N-type lines—with the trajectory  $p = \pm 1$  during  $t_1$  to  $p = \mp 1$  during  $t_2$ —are refocussed to  $k = 0$ . While detection singles out the component ending at  $p = -1$ , these two lines taken together represent a single quantum coherence that is spatially uniform over the sample, with a phase offset determined by the RF phases encountered along the trajectory. The axial lines, with the trajectory  $p = 0$  to  $p = \mp 1$  combine into a right-handed helix with wavenumber  $+\Delta k = \gamma G \delta$ , where  $\delta$  is the gradient pulse-length. The P-type lines, which remain at  $p = \mp 1$  throughout  $t_1$  and  $t_2$ , form a single-quantum coherence wrapped into a spatial helix of wavenumber  $+2\Delta k$ . In addition, there are double quantum coherences modulated with wavenumbers  $+\Delta k$  and  $+3\Delta k$ . Also present are  $\{ZQC\}$  helices modulated with

wavenumber  $+\Delta k$  and  $-\Delta k$ . Transformation of  $I_{\pm}S_z$  yields a total of four  $p = 0$  operators  $I_{\pm}S_{\mp}$  and  $I_{\mp}S_{\pm}$ , with phase factors  $\pm\Delta k$ . Since the wavenumber of the  $\{ZQC\}$  combination is determined by the  $k$  value of the  $I_{\pm}S_{\mp}$  terms, both right and left handed helices are present.

Figures 1-14A and 1-14B show a double quantum filtered COSY experiment [26] in its full complexity. As before, the symmetry of the modified coherence pathway diagram is evident. The delay  $\Delta$  and the additional gradient pulse interspersed between the evolution and detection times permits the selective filtering of only those pathways that pass through a state of  $\{DQC\}$  during  $\Delta$ . With the gradient pulse combinations used, the only observable coherence with  $p = -1$  that is refocused to  $k = 0$  during detection is seen to be the N-type signal passing through a state of  $\{DQC\}$  during  $\Delta$ . Its coherence pathway passes through states of  $[p = +1, k = -\Delta k]$ ,  $[p = +2, k = -3\Delta k]$  and  $[p = -1, k = 0]$  just after each successive gradient pulse. These operators and their symmetrically formed lines make up spatial grating components of  $\{SQC\}$  with wavenumber  $+\Delta k$ ,  $\{DQC\}$  with wavenumber  $+3\Delta k$ , and the detected  $\{SQC\}$  which is uniform over the sample with  $k = 0$ .

As in Fig. 1-13C, the complex picture of Fig. 1-14B can be simplified to depict only the coherence pathways of interest, those that result in observable coherences with  $p = -1$  during detection. These pathways may be tracked along with their corresponding  $k$ -values, with the understanding that these trajectories are accompanied by symmetric reflections about the  $p = 0$  and  $k = 0$  axes, and that combination of symmetric pairs forms spatially modulated multiple quantum coherences, whose wavenumber is determined by the  $k$  value of the line with negative coherence number  $p$ . Fig. 1-14C demonstrates the simplified diagram for certain of the N-type trajectories.

In general, more than one combination of gradient pulse lengths or amplitudes may be used to select a given coherence pathway trajectory during a pulse sequence. However, the need to eliminate all other interfering pathways adds significantly to the difficulty of selecting a working gradient sequence to perform the multiple quantum coherence selection. A useful rule of thumb to simplify the process is to drive the

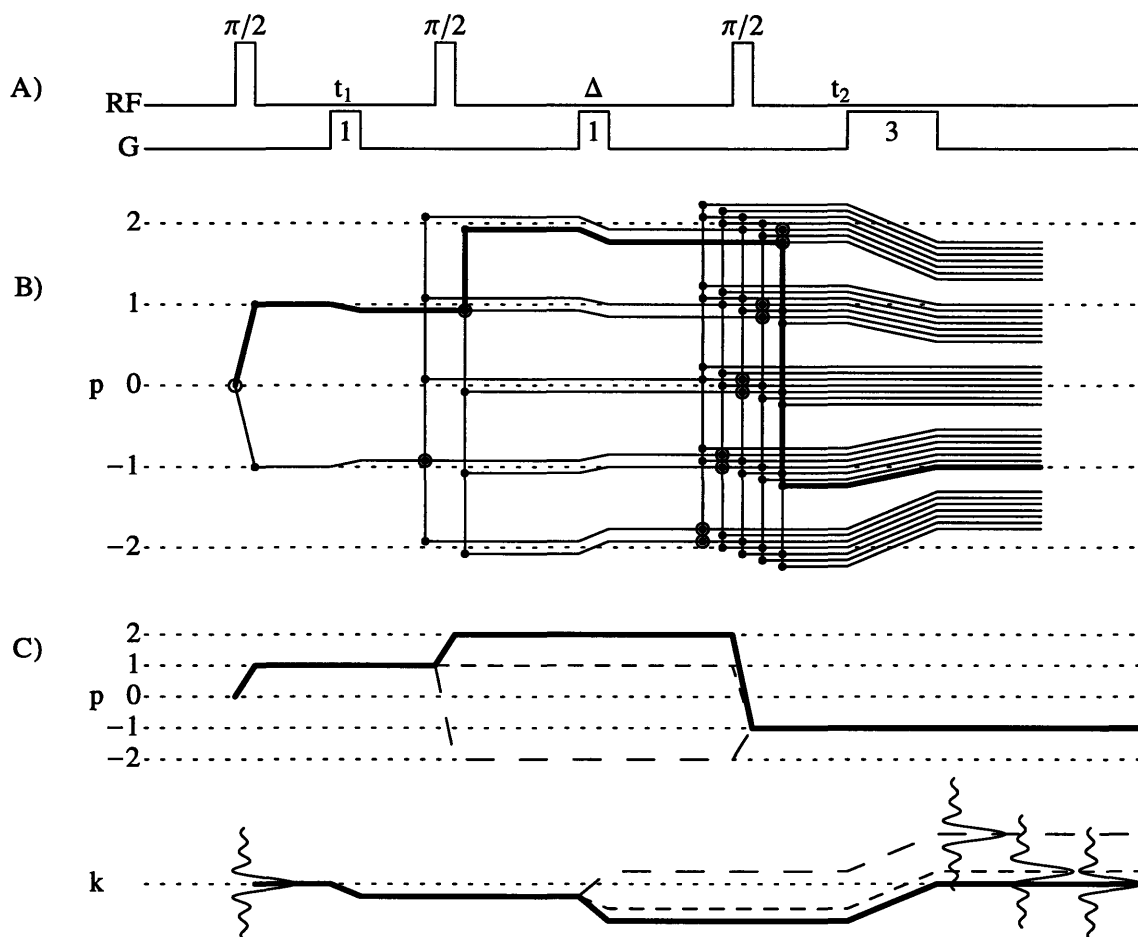


Figure 1-14: Double Quantum Filtered COSY experiment using pulsed gradients for coherence pathway selection. A) The pulse sequence. B) Coherence pathway diagram tracking coherence number  $p$  and spatial phase factor  $k$ . All lines appear in concert with symmetrically formed lines reflected about the  $p = 0$ ,  $k = 0$  axes, to form multiple quantum coherences spatially modulated with a wavenumber equal to the  $k$  value of the operator with negative  $p$ . Of the lines producing detectable states with  $p = -1$  during  $t_2$ , the combination of gradient pulses used preserves only the trajectory presented in bold, which passes through a state of  $\{DQC\}$  during the  $\Delta$  delay. RF pulses transform starting states marked by open circles into final states marked with filled circles. C) A simplified coherence pathway diagram presenting three of the N-type lines, with their corresponding  $k$ -values. Adequacy of the suppression is determined by the convolution of these line in  $k$  with the intrinsic spatial dependence of the sample  $\tilde{\rho}(k)$ .

desired trajectory to successively higher values of  $|k|$  with each gradient pulse, followed by a final refocussing gradient pulse to return the selected coherence to  $k = 0$  before detection.

### 1.8.3 Heteronuclear Experiments

In the case of a heteronuclear spin system, a further generalization must be made. Under the influence of a gradient field, each spin species  $i$  accumulates a phase factor proportional both to its coherence number  $p_i$  and to its gyromagnetic ratio  $\gamma_i$ . A spin operator containing heteronuclei accumulates a net phase factor

$$\Delta k = - \sum_i p_i \gamma_i \int G_u dt, \quad (1.30)$$

after evolution in a gradient field  $G_u$ , where the sum is over all nuclei contributing to the operator. Since the  $\gamma_i$  differ, analysis of heteronuclear experiments requires that the  $[p, k]$  trajectories be tracked separately for each nucleus.

Figure 1-15 demonstrates this bookkeeping for a heteronuclear multiple quantum coherence (HMQC) experiment [27, 28]. Each nucleus is treated separately in the first two coherence pathway diagrams, with  $k$  values determined by the appropriate gyromagnetic ratio. The gyromagnetic ratio of the proton is assumed to be four times that of carbon in this case, so that a given gradient pulse causes proton and carbon  $k$  values to change in the ratio 4 : 1.

In the proton coherence pathway diagram of Fig. 1-15B, notice the effect of the  $\pi$  pulse. In exact correspondence to the effect of  $\pi$  rotations on the magnetization grating components of previous sections, here the  $\pi$  pulse inverts the handedness of the  $\{SQC\}$  helix formed by combination of the two operators, reversing the wavenumber from  $+k$  before the pulse to  $-k$  after the pulse.

The two separate coherence pathway diagrams of Fig. 1-15B and Fig. 1-15C are combined in Fig. 1-15D into a single complete diagram tracking the net coherence number  $p_I + p_S$  and the net  $k$  value, simply by summing the  $p$  and  $k$  values of the individual proton and carbon spin trajectories. Formation of all possible combinations yields a total of twelve lines in this case. The selected pathway, for example,

is formed by merging individual spin trajectories that result in carbon chemical shift encoding during  $t_1$  and proton chemical shift evolution during  $t_2$ . The chosen proton line ends in a detectable state of  $p_I = -1$ , and contributes no net chemical shift evolution during  $t_1$ , as its coherence number is inverted midway through that period. Conversely, the selected carbon pathway is in a  $p_S = 1$  state for chemical shift encoding during  $t_1$ , but returns to a longitudinal state of  $p = 0$  during  $t_2$  so that the proton chemical shift evolution alone may be recorded. The transfer amplitudes of these individual coherence lines are determined not only by the RF pulse lengths used, but by the J-coupling transition amplitudes as well. Each  $\Delta$  period introduces a  $\sin(\pi J\Delta)$  weighting. For these desired pathways, the effect of the gradient sequence is determined by applying Eq. 1.30 during each gradient pulse.

The approach of separately tracking the coherence numbers and spatial modulations of coupled spins in heteronuclear experiments also provides correct results for homonuclear experiments, where all  $\gamma_i$  are equal. By highlighting the individual states of the  $I$  and  $S$  spins throughout the experiment, it can provide additional insight into the source of numerous lines in complex diagrams such as that of Fig. 1-14B.

## 1.8.4 General Concerns in Gradient Selection Sequences

### Suppression Factors

If the sample were uniform and of infinite extent along the gradient direction, undesired signals could be suppressed by creating slowly varying modulations of small  $k$  value, as the integral over all space would even then produce perfect signal cancellation over all phases. Equivalently, the spatial Fourier transform of the sample,  $\tilde{\rho}(k) = \delta(k)$ , has infinitesimal width, so even a slight modulation shifts the distribution enough that the  $k = 0$  component is negligible, and the suppression complete. If the sample has a spatially varying spin density, however, the starting distribution  $\tilde{\rho}(k)$  is no longer a delta function but contains contributions at higher wavenumbers. In order to produce adequate suppression, it is thus necessary to produce more rapid modulations, shifting the distribution to high enough  $k$  values that the desired level



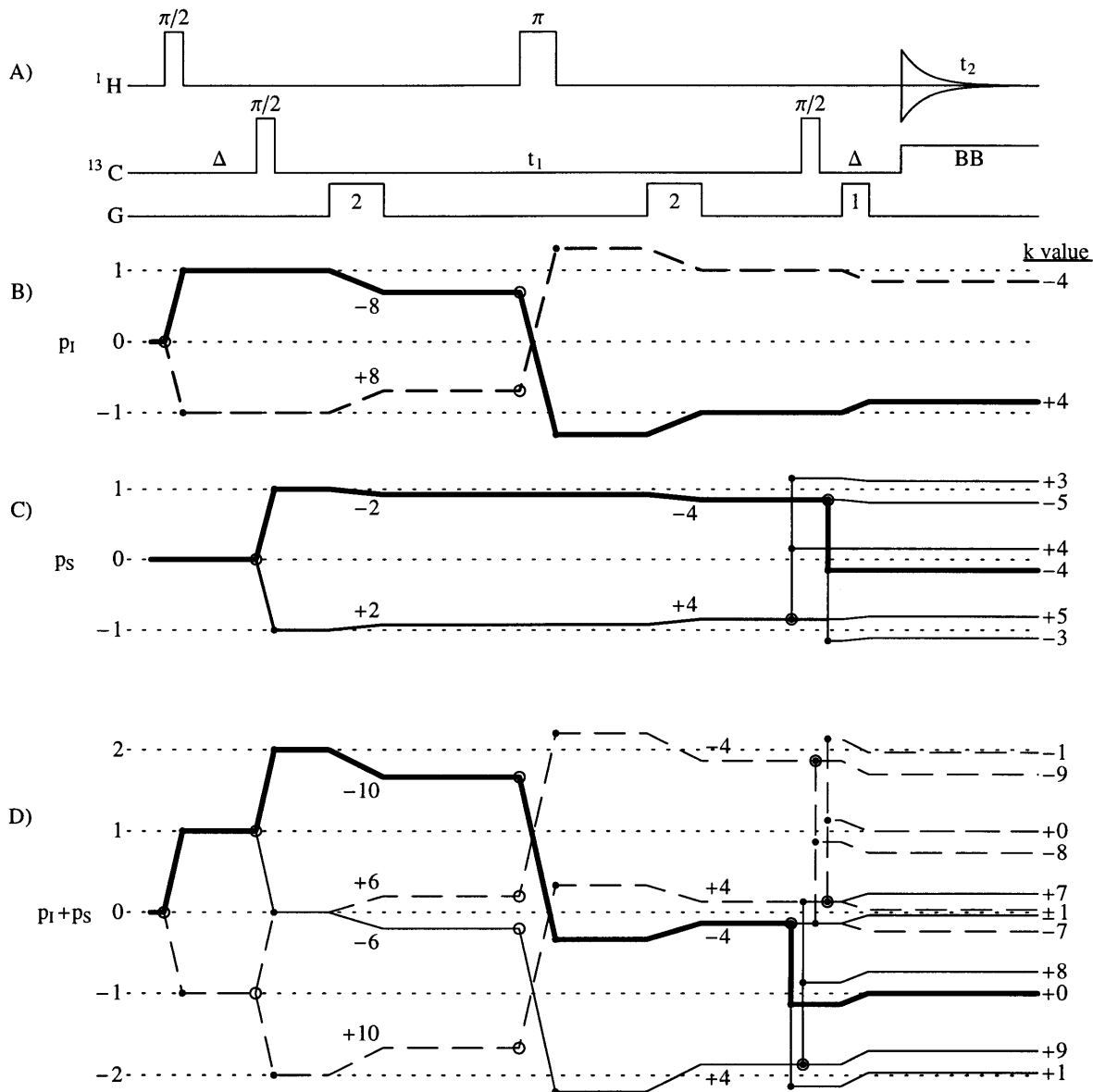


Figure 1-15: A heteronuclear multiple quantum coherence experiment. A) The pulse sequence. The modified coherence pathway diagrams for B) the proton, and C) the carbon nuclei, tracking both coherence numbers  $p_I$  and  $p_S$ , and the spatial phase factors  $k$ . D) The combined diagram, formed by merging the trajectories of B) and C) in all combinations. The dashed trajectories are those formed by combination with the dashed proton trajectory. The selected pathway is highlighted in bold, as are the component individual spin trajectories from which it is formed. Filled circles represent the states created by RF-pulse transformation of the initial operators marked with open circles. The proton gyromagnetic ratio is assumed to be exactly four times that of carbon for the gradient pulse lengths indicated. All pairs of symmetrically formed states combine into spatially modulated multiple quantum coherences whose wavenumber is determined by the  $k$  value of the state with negative  $p$ .

of suppression is attained, as is demonstrated schematically in Figs. 1-13C and 1-14C. If, for example, the sample is approximated as a rectangular region of length  $2L$  along the gradient direction, then its Fourier transform in that direction is a sinc function,

$$\tilde{\rho}(k) = 2L \operatorname{sinc}\left(\frac{kL}{\pi}\right) = 2L \frac{\sin(kL)}{kL}. \quad (1.31)$$

Shifting the distribution by  $\Delta k$  through spatial modulation of the coherence results in residual signal of magnitude  $\tilde{\rho}(\Delta k)/\tilde{\rho}(0)$ . For sample regions which are not rectangular, the distribution is no longer exactly a sinc function, but instead reflects the shape of the sample. Nonetheless, if the sample has an approximate length of  $2L$  in the gradient direction, a useful rule of thumb is that the suppression factor varies approximately as the envelope of the sinc function, yielding a suppression factor  $1/(\Delta kL)$  for a modulation at wavenumber  $\Delta k$  [29].

### Sensitivity Losses

Gradient selection techniques are versatile and may be performed with a single experimental repetition, but often suffer a sensitivity loss compared to their phase cycling counterparts [29]. One source of signal loss arises from the sensitivity of gradient techniques to the sign of the coherence number. While the P/N type selection experiment of Fig. 1-13 suffers no loss compared to phase cycling, the DQF-COSY experiment of Fig. 1-14 has half the signal intensity of the phase cycled version, as the gradient filtering selects the  $p = +1, +2, -1$  trajectory while eliminating the  $p = +1, -2, -1$  pathway. Phase cycling, on the other hand, can be devised to select both pathways simultaneously, although multiple experiment repetitions are then required. Similarly, the HMQC experiment of Fig. 1-15 suffers a sensitivity loss of 1/2 due to the selection of the  $p = +1, +2, 0, -1$  pathway at the expense of the  $p = +1, 0, +2, -1$  trajectory.

An additional source of attenuation in gradient-selection experiments arises from molecular diffusion along a given trajectory in  $[p, k]$ . Combination of a trajectory with its symmetrically formed counterpart at  $[-p, -k]$  has been seen to form a spatial modulation in the appropriate  $\{pQC\}$ . As the multiple quantum coherences

described in this section arise between nuclear spins in the same molecule, motion of the molecule through the spatial grating displaces all involved spins equally, so the previous results for moving spins still apply directly. Uniform flow or unrestricted molecular diffusion along the modulation axis results, respectively, in a pure phase shift or a pure attenuation of the coherence pathway. These factors may be calculated as in previous sections, where the  $k$ -value along the desired pathway is defined as in Eq. 1.27 for homonuclear systems, or Eq. 1.30 for heteronuclear systems. The calculation of flow-induced phase shifts is sensitive to the sign of the spatial grating, which is determined from the  $k$  value of the operator with the negative coherence number. Since these flow phenomena impact only those sample components that are spatially modulated, diffusive losses do not occur in phase-cycling experiments which proceed without field gradients.

### **Square Wave Modulation**

Although gradient-based techniques are widely used for coherence pathway selection, it would be advantageous to regain the factor of two in sensitivity that is typically sacrificed. This would allow the collection of spectra in a single scan while maintaining the full sensitivity of the related phase-cycled experiments. Techniques have recently been developed [18, 30] to address these issues, based on the notion of exciting coherences with a square wave modulation rather than the oscillatory modulations typically produced by evolution in field gradients. The key to this approach [18] is the realization that by appropriately choosing RF pulse amplitudes and phases, it is possible to tailor the  $k$  space distribution of grating components to produce a desired frequency selectivity. As Fig. 1-12 demonstrated, a series of hard pulses gives rise to a manifold of lines in  $k$  space, whose amplitude and phase factors depend on the sequence of RF pulses employed. Each line in  $k$  corresponds to a coefficient of the Fourier series describing the frequency response of the excited magnetization, here a square wave as a function of frequency. By performing this sequence with periods of gradient evolution interspersed between the RF pulses, the frequency selectivity is mapped to a spatial selectivity.

This type of square wave modulation may be used to perform a spatial analog of phase cycling [18]: Different phase cycling steps are effectively performed simultaneously in separate regions of the sample. Each spatial block is excited uniformly, but differently from its neighboring regions, in such a way that the desired signal adds uniformly over the entire sample volume, while undesired signals cancel by summation over separate blocks. Unlike standard phase cycling experiments, all phase cycling steps are performed in a single shot. Moreover, unlike typical gradient techniques, the desired signal is retained with full intensity, as signal phases vary discretely rather than continuously across the sample.

## 1.9 Summary and Conclusions

In this work, a generalized  $k$  space formalism has been presented which lends physical insight into a wide variety of NMR experiments, while at the same time retaining complete analytical correctness for any signal pathway of interest. The approach involves a Fourier decomposition of single-spin magnetization or multi-spin coherences into a set of basis functions that most naturally describe the spatial modulations formed under evolution in linear field gradients and RF pulses. Tracking the evolution of these grating components provides a complete description of the spatial behavior of the sample at all times. The formalism is not in fact restricted to describing spatial modulations in the presence of linear field gradients, but may track evolution in any inhomogeneous interaction, describing more generally variations of the sample as a function of resonance offset.

This approach lends itself to a simple graphical representation. The  $k$  space diagrams thus produced rapidly provide qualitative physical insight into the various grating components contributing to the system's overall spatial behavior. For example, these diagrams easily predict when echoes will form, and by exactly what mechanisms. Yet for any signal pathway of interest, analytically correct results are straightforward to derive, simply by accumulating amplitude and phase terms along the  $k$  space trajectory of interest. The formalism provides a conceptual framework

to describe the spatial aspects of the spin system, while simplifying the analysis of numerous experiments into straightforward steps of sketching  $k$  space diagrams and looking up the appropriate amplitudes.

# References

- [1] D. B. Twieg, “The k-trajectory formulation of the NMR imaging process with applications in analysis and synthesis of imaging methods,” *Medical Physics*, vol. 10, no. 5, pp. 610–621, 1983.
- [2] P. Mansfield and P. K. Grannell, “ “Diffraction” and microscopy in solids and liquids by NMR,” *Physical Review B*, vol. 12, no. 9, pp. 3618–3634, 1975.
- [3] J. Hennig, “Multiecho imaging sequences with low refocusing flip angles,” *Journal of Magnetic Resonance*, vol. 78, pp. 397–407, 1988.
- [4] T. R. Saarinen and C. S. Johnson, Jr., “Imaging of transient magnetization gratings in NMR. analogies with laser-induced gratings and applications to diffusion and flow,” *Journal of Magnetic Resonance*, vol. 78, pp. 257–270, 1988.
- [5] P. T. Callaghan, *Principles of Nuclear Magnetic Resonance Microscopy*. Clarendon Press, Oxford, 1991.
- [6] C. P. Slichter, *Principles of Magnetic Resonance*. Springer-Verlag, New York, 3rd ed., 1990.
- [7] E. O. Stejskal and J. E. Tanner, “Spin diffusion measurements: Spin echoes in the presence of a time-dependent field gradient,” *Journal of Chemical Physics*, vol. 42, no. 1, pp. 288–292, 1965.
- [8] D. G. Cory and A. N. Garroway, “Measurement of displacement probabilities by NMR: An indicator of compartmentalization,” *Magnetic Resonance in Medicine*, vol. 14, pp. 435–444, 1990.

- [9] P. Plateau and M. Guéron, "Exchangeable proton NMR without base-line distortion, using new strong-pulse sequences," *Journal of the American Chemical Society*, vol. 104, pp. 7211–7312, 1982.
- [10] G. A. Morris and R. Freeman, "Selective excitation in Fourier transform nuclear magnetic resonance," *Journal of Magnetic Resonance*, vol. 29, pp. 433–462, 1978.
- [11] I. J. Lowe and R. E. Wysong, "DANTE ultrafast imaging sequence (DUFIS)," *Journal of Magnetic Resonance, Series B*, vol. 101, pp. 106–109, 1983.
- [12] J. Hennig and M. Hodapp, "Burst imaging," *MAGMA*, vol. 1, pp. 39–48, 1993.
- [13] P. J. Hore, "Solvent suppression in Fourier transform nuclear magnetic resonance," *Journal of Magnetic Resonance*, vol. 55, pp. 283–300, 1983.
- [14] D. L. Turner, "Binomial solvent suppression," *Journal of Magnetic Resonance*, vol. 54, pp. 146–148, 1983.
- [15] V. Sklenář and Z. Starčuk, "1–2–1 pulse train: A new effective method of selective excitation for proton NMR in water," *Journal of Magnetic Resonance*, vol. 50, pp. 495–501, 1982.
- [16] A. G. Redfield, S. D. Kunz, and E. K. Ralph, "Dynamic range in Fourier transform proton magnetic resonance," *Journal of Magnetic Resonance*, vol. 19, pp. 114–117, 1975.
- [17] C. Wang and A. Pardi, "NMR spectra of exchangeable protons using uniform excitation solvent suppression pulse sequences," *Journal of Magnetic Resonance*, vol. 71, pp. 154–158, 1987.
- [18] W. E. Maas and D. G. Cory, "Discrete magnetization gratings in NMR spectroscopy," *Chemical Physics Letters*, vol. 254, pp. 165–169, 1996.
- [19] D. I. Hoult, "The solution of the Bloch equations in the presence of a varying  $B_1$  field—an approach to selective pulse analysis," *Journal of Magnetic Resonance*, vol. 35, pp. 69–86, 1979.

- [20] J. Pauly, D. Nishimura, and A. Macovski, "A k-space analysis of small-tip-angle excitation," *Journal of Magnetic Resonance*, vol. 81, pp. 43–56, 1989.
- [21] I. Serša and S. Macura, "Excitation of arbitrary shapes in nuclear magnetic resonance by a random walk in discrete k space," *Journal of Magnetic Resonance, Series B*, vol. 111, pp. 186–188, 1996.
- [22] O. W. Sørensen, G. W. Eich, M. H. Levitt, G. Bodenhausen, and R. R. Ernst, "Product operator formalism for the description of NMR pulse experiments," *Progress in NMR Spectroscopy*, vol. 16, pp. 163–192, 1983.
- [23] A. Bax, P. G. DeJong, A. F. Mehlkopf, and J. Smidt, "Separation of the different orders of NMR multiple-quantum transitions by the use of pulsed field gradients," *Chemical Physics Letters*, vol. 69, no. 3, pp. 567–570, 1980.
- [24] A. A. Maudsley, A. Wokaun, and R. R. Ernst, "Coherence transfer echoes," *Chemical Physics Letters*, vol. 55, no. 1, pp. 9–14, 1978.
- [25] P. Barker and R. Freeman, "Pulsed field gradients in NMR. An alternative to phase cycling," *Journal of Magnetic Resonance*, vol. 64, pp. 334–338, 1985.
- [26] R. E. Hurd, "Gradient-enhanced spectroscopy," *Journal of Magnetic Resonance*, vol. 87, pp. 422–428, 1990.
- [27] R. E. Hurd and B. K. John, "Gradient-enhanced proton-detected heteronuclear multiple-quantum coherence spectroscopy," *Journal of Magnetic Resonance*, vol. 91, pp. 648–653, 1991.
- [28] J. Ruiz-Cabello, G. W. Vuister, C. T. W. Moonen, P. van Gelderen, J. S. Cohen, and P. C. M. van Zijl, "Gradient-enhanced heteronuclear correlation spectroscopy. Theory and experimental aspects," *Journal of Magnetic Resonance*, vol. 100, pp. 282–302, 1992.
- [29] J. Keeler, R. T. Clowes, A. L. Davis, and E. D. Laue, "Pulsed-field gradients: Theory and practice," *Methods in Enzymology*, vol. 239, pp. 145–207, 1994.



- [30] Q. N. Van and A. J. Shaka, “A pulsed-field-gradient NMR technique without the usual sensitivity loss. Spatial population sculpting,” *Journal of Magnetic Resonance, Series A*, vol. 119, pp. 295–301, 1996.

## Chapter 2

# RF Gradient BIRD/TANGO

# Sequence to Eliminate Uncoupled Magnetization<sup>1</sup>

## 2.1 Introduction

Ubiquitous in NMR spectroscopy is the need to study a particular signal of interest in the presence of background signals that may be comparatively quite large. A number of techniques exist to remove the unwanted signal components. The most widely used of these techniques rely on phase cycling or on the application of  $B_0$  gradients. Phase-cycling relies on systematically changing RF phases in the pulse cycle to alter the phases of signal components during subsequent scans. The resulting signals are then combined in such a way that the desired signal adds constructively while undesired components cancel to zero. This, however, requires numerous acquisitions, and yields poor digitizer resolution for small signals of interest, as the digitizer dynamic range is filled in each scan by the dominant unwanted resonances (e.g the solvent signal) before being removed by signal combination.

---

<sup>1</sup>A shortened version of this work will be published shortly: A. Sodickson and D. G. Cory, "RF gradient BIRD/TANGO sequence to eliminate uncoupled magnetization," *Journal of Magnetic Resonance*, 1997, in press.

Static  $B_0$  gradient techniques [1] are commonly used with a similar rationale. Gradient pulses are applied at appropriate points in the pulse cycle and produce a spatially-dependent phase evolution in the various coherences present. By choosing appropriate gradient pulse lengths and timings, one can arrange for part of the desired signal to pass through the pulse sequence in phase, while unwanted signal components are left with a spatially-dependent phase factor that causes the net signal to integrate to zero over the full sample volume.  $B_0$  gradient techniques have the advantage that unwanted coherence pathways are eliminated in each scan, yielding improved digitizer resolution as the receiver gain can be increased to observe the small signals alone. However, standard techniques often incur a sensitivity loss if the desired signal component is not modulated uniformly over the sample volume but instead integrates to a dc-level less than unity.

RF gradient techniques rely on variations in the  $B_1$  field strength to dephase unwanted magnetization components in a plane containing the z-axis, in contrast to the transverse phase modulation caused by  $B_0$  gradients.  $B_1$  gradient techniques have a number of intrinsic advantages. The gradients are frequency selective, they may be implemented with standard RF probe and amplifier hardware, they have rapid switching times and do not perturb the lock system or require recovery from eddy current effects.

Most importantly, for some applications, as in the sequences described below,  $B_1$  gradients fit more logically into the pulse sequence structure than  $B_0$  gradients, by preserving its overall structure and symmetries. Since RF gradients are capable of simultaneously producing coherence transformations and encoding spatial modulations, they may be incorporated into an experiment without even altering the form of the pulse sequence, simply by replacing appropriate excitation pulses with RF gradient pulses. Previous applications of  $B_1$  gradients include solvent suppression [2, 3], P/N-type selection [4, 5], multiple quantum filters [6, 7, 8], and heteronuclear correlation spectroscopy [9].

In this report, a modification of the BIRD and TANGO sequences is presented which uses RF gradients to eliminate the net magnetization from uncoupled spins,

while completely preserving coupled magnetization. The RF gradient sequence was developed to perform selective excitation and saturation simultaneously, as a function of the scalar coupling constant  $J_{CH}$ . It is designed so that RF gradients selectively dephase the unwanted magnetization components (here, uncoupled spins with  $J = 0$ ) over the sample volume, while the desired components—those coupled with a particular scalar coupling strength—are completely refocussed. The sequence acts as a selective filter to pass magnetization with a particular scalar-coupling constant. It may be used alone or at any point in a lengthier sequence. It simultaneously eliminates the unwanted signal components while retaining the desired magnetization with no theoretical attenuation factor, in contrast to static  $B_0$  gradient techniques which often sacrifice sensitivity due to signal averaging over the sample volume. It is performed as a single-shot experiment which at the same time makes maximal use of the receiver dynamic range, in contrast to phase cycling schemes which require the addition of multiple signals of which the desired component is only a small part. A  $B_0$ -gradient modification of the BIRD sequence with similar goals has previously been reported [10]. Like the  $B_1$ -gradient version presented here, it dephases unwanted magnetization while retaining the coupled magnetization without any loss in sensitivity.

The effect of the RF-gradient sequence was confirmed here using only the residual RF inhomogeneity of a standard “homogeneous coil.” It is demonstrated for selective excitation of the satellites in a sample of chloroform, yielding suppression of the uncoupled magnetization by a factor of approximately 800. Practical application of these techniques is likely to benefit further from the use of specially designed RF gradient coils with an enhanced  $B_1$  inhomogeneity, like those described in [4, 11].

## 2.2 RF vs. $B_0$ Gradients

Unlike  $B_0$  gradients which dephase magnetization in the transverse plane, RF gradients instead spread out magnetization over a plane which is normal to the local  $B_1$  field and which thus contains the z-axis. There are a number of intrinsic differences between the effects of these two types of gradients which must be understood in order

to design effective gradient strategies.

## **$B_0$ Gradients**

$B_0$  gradients comprise variations in the static  $B_0$  field. Typical gradient coils produce linear field gradients along each lab frame cartesian axis  $g_x = dB_z/dx$ ,  $g_y = dB_z/dy$ , and  $g_z = dB_z/dz$ . Since the curl of the field must equal zero, these coils also produce transverse field components—a  $g_x$  coil, for example, will also produce a static field gradient varying as  $dB_x/dz$ . However, the magnitude of these fields is small compared with the uniform  $B_0$  field (typically less than 1 part in  $10^4$ ). As a result, the vector sum of  $B_0$  with these transverse static fields is not perturbed significantly from the +z axis, or equivalently, rapid Larmor precession about the large  $B_0$  field second-averages any evolution about the small static transverse fields. The symmetry imposed upon the NMR experiment by the strong  $B_0$  field thus allows these transverse field components to be neglected, as only the secular components of the gradient fields (those along z) affect spin evolution. This greatly simplifies the design of gradient coils, and field gradients are typically quite linear over the sample region of interest, a great advantage for many NMR applications including imaging and the measurement of motion phenomena such as flow and diffusion.

The static field gradients  $g_x$ ,  $g_y$  and  $g_z$  are all secular—they all commute with  $B_0$ , and thus all cause rotations about the z-axis. Their Hamiltonians all commute with one another, so evolution in these gradients produces additive results. For example, application of a gradient pulse of length  $\tau$  along x followed by one along y (or vice versa) produces a net phase factor  $\gamma(g_x x + g_y y)\tau$  which is simply the sum of the individual phases. This property greatly simplifies experiments employing gradients varying along more than one direction. In imaging, spatial modulations may be encoded along orthogonal axes with separable effects. In suppression techniques, use of orthogonal  $B_0$  gradients may be used to provide better elimination of unwanted coherences, if these coherences are dephased about, for example, both the x and y axes. Since the interactions commute, there is no way for gradient evolution along one axis to be refocussed by evolution in an orthogonal gradient.

Nonetheless,  $B_0$  gradients do have some practical disadvantages. As the fields are static, the skin depth in conducting surfaces is large, and gradient pulses produce substantial eddy currents in the magnet dewar and superconducting coils. This not only perturbs the lock system during gradient application, but also requires long settling times before subsequent RF pulses are applied or signal acquisition is begun. Since  $B_0$  is quite large, significant gradient evolution requires the construction of strong gradient coils which have long rise times due to their large inductance, and which require high power amplifiers to produce the necessary currents.

### $B_1$ gradients

Radiofrequency gradients exploit spatial variation in the  $B_1$  field strength, and perform dephasing about the RF axis since the nutation frequency varies as a function of position in the sample. For a given RF coil, these gradients may be denoted as  $g_x = dB_x/du$  and  $g_y = dB_y/du$ , where  $u$  is defined as the local gradient axis, and the phase of the RF pulse determines whether evolution occurs under  $g_x$  or  $g_y$ .

Since these gradient fields are modulated at the Larmor frequency, all transverse components affect the spin system, so it is generally more difficult to produce an RF gradient that varies linearly with position. Composite pulses have been used to produce linear gradients from a quadrupolar field geometry [4], although in this case the strength of the  $B_1$  field passes through zero, where off-resonance effects become significant.

As the RF-gradient Hamiltonians do not commute with one another, evolution in separate gradients does not occur independently, in contrast to the  $B_0$  gradient case. For example, if starting equilibrium magnetization along  $z$  is dephased sequentially by equal pulses of  $g_x$  and  $g_y$ , half of the  $z$  magnetization is in fact refocussed by the second pulse, while the other half is dephased further. This effect occurs since the intrinsic spatial variation of the  $B_1$  field gradients is the same for  $g_x$  and  $g_y$ , and only the nutation axis varies.

A further complication of  $B_1$  gradients is their dependence on resonance offset. In the rotating frame, nutation occurs about an effective axis that is tilted out of

the transverse plane. If off-resonance effects are significant, this effective axis varies throughout the sample in a  $B_1$  field-dependent manner, which can complicate gradient experiments and potentially reduce the attainable suppression of unwanted coherences if not dealt with explicitly.

Despite these experimental issues, RF gradients do have a number of intrinsic advantages over  $B_0$  field gradients. They are frequency selective, and can be applied independently to different nuclear species [9], unlike static gradients. They use standard RF hardware, and are thus easily integrated into the pre-existing system architecture. They do not require additional amplifiers, do not interfere with the lock system, and have very rapid switching times.

Most importantly, for certain applications such as the sequences discussed below, RF gradients fit most naturally into the pulse sequence. Since they are able to simultaneously perform coherence transformations and gradient dephasing, these sequences can be made more compact than their  $B_0$  gradient counterparts.

RF gradients are nonsecular—they do not commute with the Zeeman Hamiltonian. As a result, they may be used to coherently modulate secular  $I_z$  interactions, either eliminating or scaling the effects of these Hamiltonians by second-averaging.

In general, the spin system under study may be segmented into spin packets that differ on the basis of chemistry (chemical shift and J-coupling), and as a function of  $B_0$  field strength variations (due to shimming and susceptibility variations), and  $B_1$  field strength variations (in the presence of an RF gradient), all of which generally have a complex functional dependence on position within the sample. Just as signal detection in  $B_0$  gradient experiments is sensitive only to the  $k = 0$  component, NMR experiments more generally involve an intrinsic integration over all dynamical degrees of freedom—the net signal is a sum over all spin-packets in the sample.

Because RF gradients are nonsecular, they may be used in certain circumstances to collapse the dimensionality of the spin dynamics, so that the only spin-packet degree of freedom governing evolution is the  $B_1$  field strength. For example, spin-locking in an RF field eliminates chemical shift evolution by second-averaging, while reducing the loss of transverse magnetization by lengthening the transverse relaxation

time constant to a value intermediate between  $T_2$  and  $T_1$ .

### 2.2.1 RF Gradients in Practice

Standard NMR probes are designed to have uniform  $B_1$  profiles, in order to produce uniform excitation and detection profiles across the sample volume, with the object of achieving maximal sensitivity and location-independent effects of multiple-pulse cycles. Even in these probes, however, residual RF inhomogeneity produces differential nutation angles relative to the nominal flip angle.

Figures 2-1, 2-2, 2-3, and 2-4 are experimental spectra performed in order to characterize the  $B_1$  inhomogeneity present across the sample volume. Each represents a different cross-section through the multidimensional space that defines the spin packet dynamics.

Figure 2-1 is the result of a nutation experiment for the proton coil from a commercial Bruker 500 MHz  $\{^1H, ^{13}C, ^{15}N\}$  probe. In this experiment a series of short RF pulses are applied on resonance with one data point collected after each pulse. In order to satisfy the Nyquist condition, the nutation angle of each pulse must be less than  $\pi$ . For an RF axis along x, the net magnetization vector nutates periodically in the y-z plane, but attenuates due to the differential nutation of spin packets located in regions of differing RF field strength. The transverse magnetization is thus sine-modulated at the RF-nutation frequency  $\omega_1$ , so Fourier transformation yields the distribution of  $\omega_1$  over the sample volume, or equivalently, how many spins in the sample experience each particular  $B_1$  field strength. The distribution is highly peaked at the nominal nutation frequency, with a full width at half maximum that is only a few percent of the peak  $B_1$ , but it also contains relatively broad shoulders — with a full width of approximately 25% — as portions of the sample experience RF fields that vary significantly from the average value.

Figure 2-2 demonstrates a 2D nutation experiment. A small readout gradient is used to collect a gradient echo after each increment in nutation angle. Fourier transformation in both domains then produces a nutation spectrum as in Fig. 2-1, but spread out over a one-dimensional projection along the gradient direction, here along



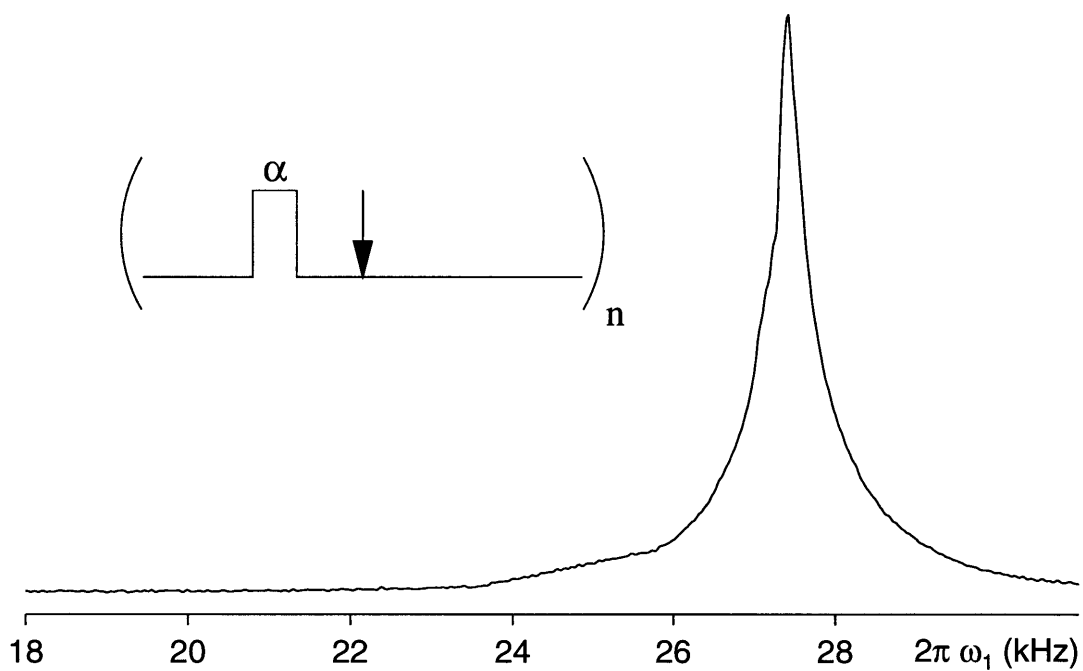


Figure 2-1: Nutation Experiment: On-resonance RF pulses are applied sequentially to a sample of  $\text{H}_2\text{O}$ , with one data point collected after each pulse. The net magnetization vector nutates about the RF-axis at the average  $\omega_1$  frequency, and attenuates due to the dispersion in RF field strength over the sample volume. Each spin packet contributes a transverse magnetization component that is sine modulated at the local nutation frequency. Fourier transformation then yields the distribution of  $B_1$  field strengths over the sample volume.

$z$ . The sharp central ridge corresponds to the region of greatest RF homogeneity, with  $\omega_1 \approx 27$  kHz, and is approximately 1 cm long for the coil used. Just past either end of the coil, the nutation frequency falls rapidly to zero. At a given  $z$  position, the spread in  $B_1$  reflects the RF field inhomogeneity in the corresponding x-y plane through the sample.

Figure 2-3 is a plot of chemical shift as a function of position along  $z$ . Variations in the lineshape as a function of position in part reflect residual field inhomogeneities that have not been removed entirely by shimming. Nonetheless, on the whole different slices through the sample exhibit fairly similar linewidths and center frequencies. Spins at each chemical shift value throughout the entire sample form a spin packet, whose spatial variation depends on the uniformity of the  $B_0$  field, and on the sample geometry.

Figure 2-4 displays a spectrum of nutation frequency as a function of chemical shift frequency. A spin packet at a given chemical shift value experiences a range of  $B_1$  field strengths over its finite spatial extent. Evolution in an RF gradient thus further subdivides the sample into spin packets differing on the basis of nutation frequency as well, which provides a mechanism to dephase spins which are otherwise magnetically indistinguishable.

If a commercial probe with a “homogeneous” coil of the sort used in the nutation experiment of Fig. 2-1 is employed for RF gradient applications, effective averaging requires that long high power pulses be used to produce an average nutation many times the nominal  $2\pi$  pulse length. A coil with a residual RF inhomogeneity of approximately 10%, for example, would spread the magnetization approximately 10 times about the RF axis during a hard pulse whose nominal flip angle is 100 full cycles. This will cause a substantial suppression, but will nonetheless leave some residual net magnetization if spins are not spread uniformly throughout the plane. The amount of uncanceled magnetization depends on the geometries of the sample volume and of the RF field inhomogeneity, which determine the shape of the nutation spectrum. The decay envelope during a long RF pulse is simply the inverse Fourier transform of the nutation distribution. Equivalently, as a long RF pulse is applied, one

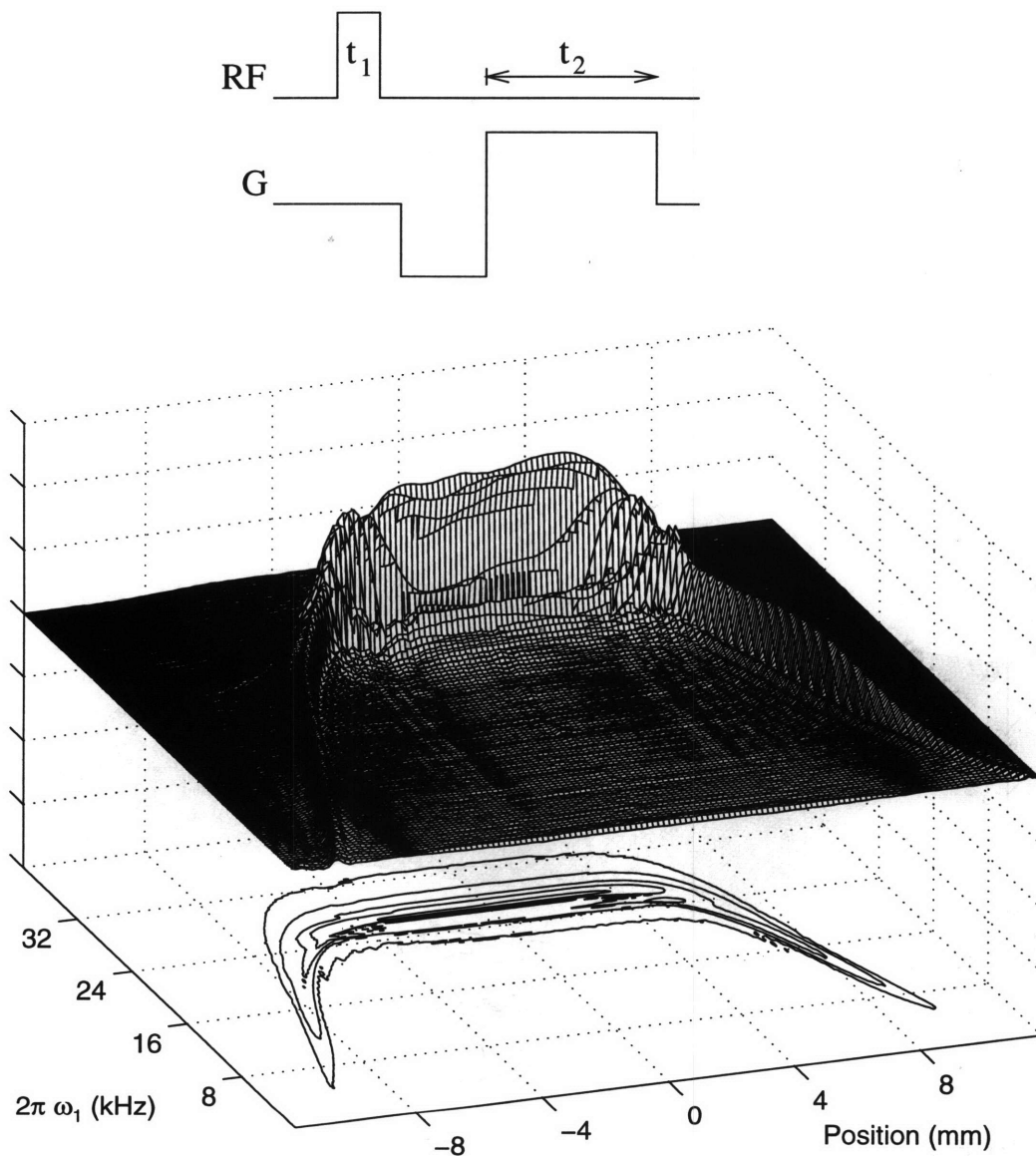


Figure 2-2: A 2D nutation experiment mapping out the  $B_1$  field strength as a function of position along  $z$  in the sample. An extension of the 1D nutation experiment is performed, with a gradient echo collected after each increment in nutation angle, to yield a projection along  $z$ . In the center of the coil, the RF field is rather homogeneous, with  $\omega_1 \approx 27$  kHz, but falls off rapidly outside the coil. The  $B_1$  variation in each  $x$ - $y$  plane through the sample is evident in the spread of the distribution at fixed  $z$ -position.

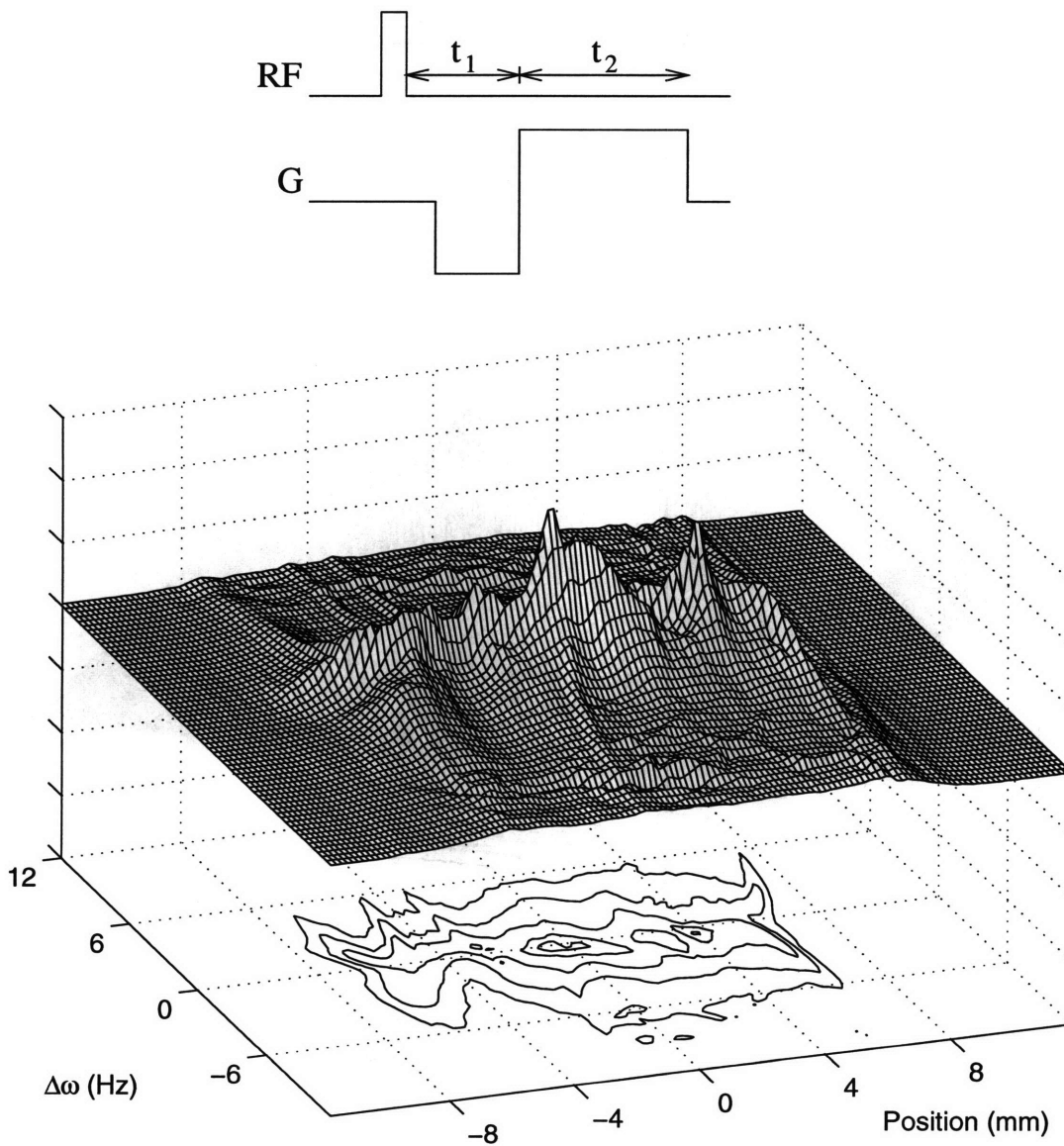


Figure 2-3: Chemical shift as a function of position along  $z$ . The  $t_1$  evolution time encodes chemical shift evolution, while a gradient echo is collected during  $t_2$  to yield a projection along the  $z$  direction. In a well-shimmed  $B_0$  field, spin packets at each chemical shift value are spread over the full sample extent.

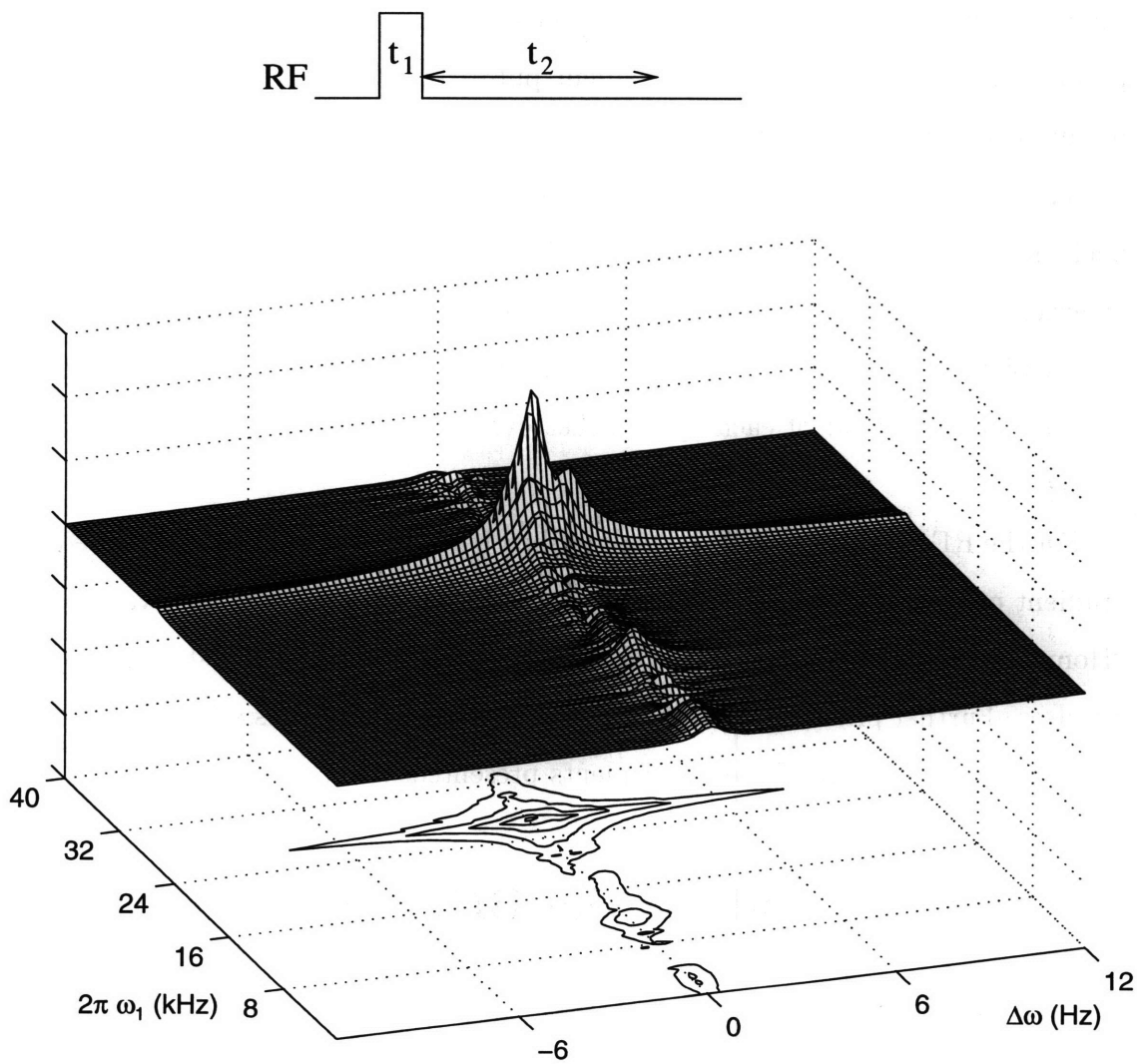


Figure 2-4:  $B_1$  field strength as a function of chemical shift value. The nutation angle is incremented in steps during  $t_1$ , while chemical shift evolution is recorded during  $t_2$ . Spin packets composed of spins which are indistinguishable on the basis of chemical shift are subdivided as a function of local RF field strength, providing a mechanism for spin-packet dephasing.

may envision the residual signal as the integral of the nutation spectrum of Fig. 2-1 after multiplication by a sine function whose pitch increases steadily with time. This sine function represents the differential nutation angle between spin packets sitting in different RF field strengths. For a coil with an inhomogeneity of 10%, 5 periods of the sine wave would fit inside the nutation spectrum after 50 nominal  $2\pi$  cycles, 10 periods after 100 cycles. Longer gradient pulses produce more rapidly varying sine modulations and better suppression factors after integration over the  $\omega_1$  axis.

This integration over the nutation spectrum in fact occurs separately for spin packets at each chemical shift value of Fig. 2-4. Each of these spin packets must experience sufficient dispersion in  $\omega_1$  over the sample volume to produce adequate suppression at each offset. A well-shimmed sample assists the suppression by increasing the spatial spread of each spin packet over sample regions of different RF field strength.

For the RF-gradient experiments described below, long RF pulses were used as the gradient pulses, utilizing the slight  $B_1$  inhomogeneity to produce effective dephasing. “Homogeneous” pulses of short duration were used to produce the standard  $\pi/2$  and  $\pi$  pulses. Further practical aspects of RF-gradient use are discussed at the end of this chapter, in the context of the experiments presented below.

## 2.3 Background for the BIRD and TANGO Sequences

### 2.3.1 Pulse Sequence Building Blocks

Two common pulse sequence building blocks will be of use in describing the standard BIRD and TANGO sequences as well as their RF-gradient counterparts. The unit  $\tau - \pi_x - \tau$  is used in many NMR sequences to refocus evolution under the chemical shift and heteronuclear J-couplings. Transverse magnetization acquires a phase  $\Delta\omega\tau$  after evolution for time  $\tau$  under the chemical shift hamiltonian  $\Delta\omega I_z$ . The  $\pi$  pulse inverts this phase angle, resulting in complete refocussing after evolution during the second

$\tau$  period. Since the  $\pi$  pulse has no effect on the spin state  $S_z$  of the heteronuclear coupling partner, the scalar coupling evolution frequency  $2\pi JS_z$  remains the same on both sides of the  $\pi$  pulse, in analogy with the chemical shift, so its effects are refocussed as well. The building-block thus behaves as  $\pi_x$  while completely refocussing evolution under the chemical shift and the heteronuclear  $J_{CH}$  coupling.

The sequence  $\tau - \pi_x(^1H, ^{13}C) - \tau$  refocusses chemical shift evolution just as the  $\tau - \pi_x(^1H) - \tau$  unit does. However, the additional  $\pi$  pulse on the X-nucleus (here  $^{13}C$ ) inverts  $S_z$ , reversing the sense of evolution at the same time as the phase inversion. Evolution under the heteronuclear  $J_{CH}$  coupling therefore accumulates for both  $\tau$  periods, as may be seen in the graphical representation of Fig. 2-5 or in the corresponding product operator description:

$$\begin{aligned} \begin{Bmatrix} I_x \\ I_y \\ I_z \end{Bmatrix} &\xrightarrow{\tau} \begin{Bmatrix} I_x \cos(\pi J\tau) + 2I_y S_z \sin(\pi J\tau) \\ I_y \cos(\pi J\tau) - 2I_x S_z \sin(\pi J\tau) \\ I_z \end{Bmatrix} \xrightarrow{\pi_x} \begin{Bmatrix} I_x \cos(\pi J\tau) + 2I_y S_z \sin(\pi J\tau) \\ I_y \cos(\pi J\tau) - 2I_x S_z \sin(\pi J\tau) \\ I_z \end{Bmatrix} \quad (2.1) \\ &\xrightarrow{J_{CH}} \begin{Bmatrix} I_x \cos(\pi J\tau) + 2I_y S_z \sin(\pi J\tau) \\ -I_y \cos(\pi J\tau) + 2I_x S_z \sin(\pi J\tau) \\ -I_z \end{Bmatrix} \xrightarrow{\tau} \begin{Bmatrix} I_x \cos[\pi J(2\tau)] + 2I_y S_z \sin[\pi J(2\tau)] \\ -I_y \cos[\pi J(2\tau)] + 2I_x S_z \sin[\pi J(2\tau)] \\ -I_z \end{Bmatrix}. \end{aligned}$$

This unit behaves as  $\pi_x$  for  $J = 0$ , and as  $\pi_y$  for  $J_{CH} = 1/2\tau$ . It is precisely this differential effect on coupled versus uncoupled spins that makes possible the selectivity of the excitation techniques described below. Changing the phase of the central proton  $\pi_x$  pulse to  $\pi_y$  reverses the effect of the building block: the sequence then behaves as a net  $\pi_y$  for uncoupled spins, and as  $\pi_x$  for spins coupled with  $J_{CH} = 1/2\tau$ . All sequences which exert their selective effects through the  $\tau - \pi(^1H, ^{13}C) - \tau$  building block thus have their actions on coupled versus uncoupled spins reversed by a  $90^\circ$  phase shift of the central proton  $\pi$  pulse.

### 2.3.2 Standard BIRD Sequence

The standard BIRD<sub>x</sub> sequence  $(\pi/2)_x - \tau - \pi_x(^1H, ^{13}C) - \tau - (\pi/2)_x$  is composed simply of the  $\tau - \pi(^1H, ^{13}C) - \tau$  unit of Fig. 2-5 surrounded by  $(\pi/2)_x$  pulses [12].

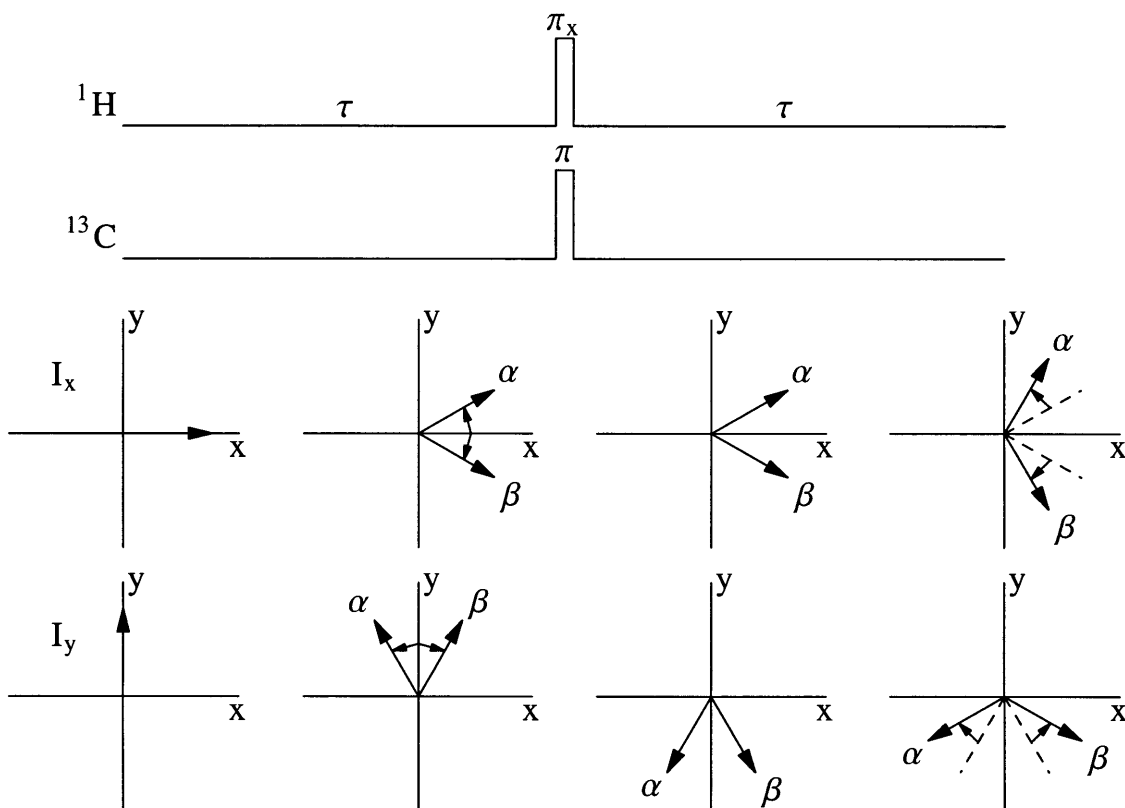


Figure 2-5: A common pulse-sequence building block, responsible for the selectivity of the standard BIRD and TANGO sequences and their RF-gradient modifications. The sequence is displayed above a graphical representation of the magnetization state at subsequent stages of the pulse sequence. The starting spin state  $I_x$  or  $I_y$  evolves for a time  $\tau$  under the chemical shift Hamiltonian and under a heteronuclear  $J$ -coupling. Inverting pulses are applied on both nuclei, after which an additional  $\tau$  evolution occurs, resulting in the final spin state. The  $^1\text{H}$   $\pi_x$  pulse refocusses evolution under the chemical shift and inverts the  $^1\text{H}$  spin states about the  $x$ -axis. The  $^{13}\text{C}$   $\pi$  pulse swaps the  $^{13}\text{C}$  spin labels  $\alpha \leftrightarrow \beta$  at the same time as the  $^1\text{H}$  inversion, thus allowing continued evolution under the heteronuclear  $J_{CH}$  coupling for the full  $2\tau$  period. For  $J = 0$ , the overall effect is a  $\pi_x$  rotation, while for  $J = 1/2\tau$ , the net result is  $\pi_y$ .



Replacing the central building block with  $\pi_x$  or  $\pi_y$  for uncoupled and coupled spins, respectively, reveals the behavior of the overall sequence:

$$\begin{aligned}
 J = 0 : & \quad (\pi/2)_x - \overbrace{\tau - \pi_x(^1H, ^{13}C) - \tau}^{\pi_x} - (\pi/2)_x = 2\pi_x \\
 2J\tau = 1 : & \quad (\pi/2)_x - \underbrace{\tau - \pi_x(^1H, ^{13}C) - \tau}_{\pi_y} - (\pi/2)_x = \pi_y.
 \end{aligned} \tag{2.2}$$

BIRD<sub>x</sub> thus acts as a  $2\pi_x$  pulse for uncoupled spins, and as  $\pi_y$  for coupled magnetization. If the system starts in equilibrium, BIRD<sub>x</sub> inverts the coupled magnetization to -z while leaving uncoupled spins along +z.

### 2.3.3 Standard TANGO Sequence

The standard TANGO sequence  $(\pi/2 + \alpha)_x - \tau - \pi_x(^1H, ^{13}C) - \tau - (\pi/2 - \alpha)_x$  can be understood most generally by recognizing its equivalence to the sequence  $\alpha_x - \text{BIRD}_x - \alpha_{-x}$ , simply a formal rotation of the BIRD<sub>x</sub> sequence by an angle  $-\alpha$  about the x-axis [13]. TANGO thus still acts as a  $2\pi_x$  rotation for  $J = 0$ , leaving uncoupled spins along +z. For  $2J\tau = 1$ , however, the net effect is  $\alpha_x - \pi_y - \alpha_{-x}$ , equivalent to a  $\pi$  rotation about an axis in the y-z plane, at an angle  $\alpha$  below the y-axis. For the standard TANGO sequence where  $\alpha = \pi/4$ , coupled magnetization starting along +z is thus placed along -y for  $2J\tau = 1$ .

## 2.4 RF Gradient Sequences

Both the BIRD and TANGO sequences are ideal candidates for RF gradient use. Without further complication of the sequences, they can be modified to eliminate the uncoupled magnetization rather than leaving it unperturbed along +z. At the same time, these modified sequences result in complete retention of the desired magnetization that is directly bound to a coupling partner with a scalar coupling constant  $J_{CH} = 1/2\tau$ .

### 2.4.1 RF Gradient BIRD (rBIRD)

The RF gradient BIRD sequence is formed simply by replacing the  $(\pi/2)_x$  pulses in the standard sequence with long RF-gradient pulses  $a_x$  which result in nutation angles  $a$  that vary throughout the sample in a manner dependent on the coil geometry. This sequence is depicted in Figure 2-6A.

The first RF gradient pulse dephases all magnetization components in the y-z plane. The central  $\tau - \pi(^1H,^{13}C) - \tau$  unit is then the key to the sequence's selective action on coupled versus uncoupled magnetization. For  $J = 0$ , the central building block unit results in a  $\pi_x$  nutation about the RF axis. The second gradient pulse then causes further dephasing. The result is that uncoupled magnetization nutates through a spatially-dependent angle  $(\pi + 2a)_x$ , and is spread throughout the y-z plane (Fig. 2-6B). For a sufficiently long RF gradient pulse,  $a$  varies continuously over many cycles throughout the range zero to  $2\pi$ , and the net signal integrates to zero:

$$\begin{aligned}
 J = 0 : I_z &\Rightarrow \int_0^{2\pi} [-I_z \cos(2a) + I_y \sin(2a)] da = 0 \\
 2J\tau = 1 : a_x - \pi_y - a_x &= a_x - \underbrace{\pi_y - a_x - \pi_{-y}}_{a_{-x}} - \pi_y = \pi_y.
 \end{aligned}
 \tag{2.3}$$

For  $2J\tau = 1$ , however, the effect of the central unit is instead a  $\pi_y$  rotation, which causes the second gradient pulse to refocus the magnetization completely in a rotary echo and results in complete retention of this magnetization component (Fig. 2-6C). Substituting the equivalent rotation  $a_{-x}$  for  $\pi_y - a_x - \pi_{-y}$  in Eq. [2.3] makes it clear that the net effect on coupled magnetization is simply a net  $\pi_y$  rotation.

Alternatively, the experiment is easily described by re-quantizing the spin states along the axis of the RF-gradient pulses [14]. Any magnetization—transverse or longitudinal—that is in a plane orthogonal to the RF-axis may be viewed as a combination of states with effective coherence numbers  $k_x = \pm 1$  when quantized along the RF-axis (here along x). These states thus dephase in the RF-gradient, just as z-quantized  $\pm 1$  quantum coherences dephase about the z-axis under the influence of a  $B_0$  gradient. Conversely, transverse magnetization that lies along the RF-axis has an effective coherence number of  $k_x = 0$  in this basis set, and does not therefore evolve

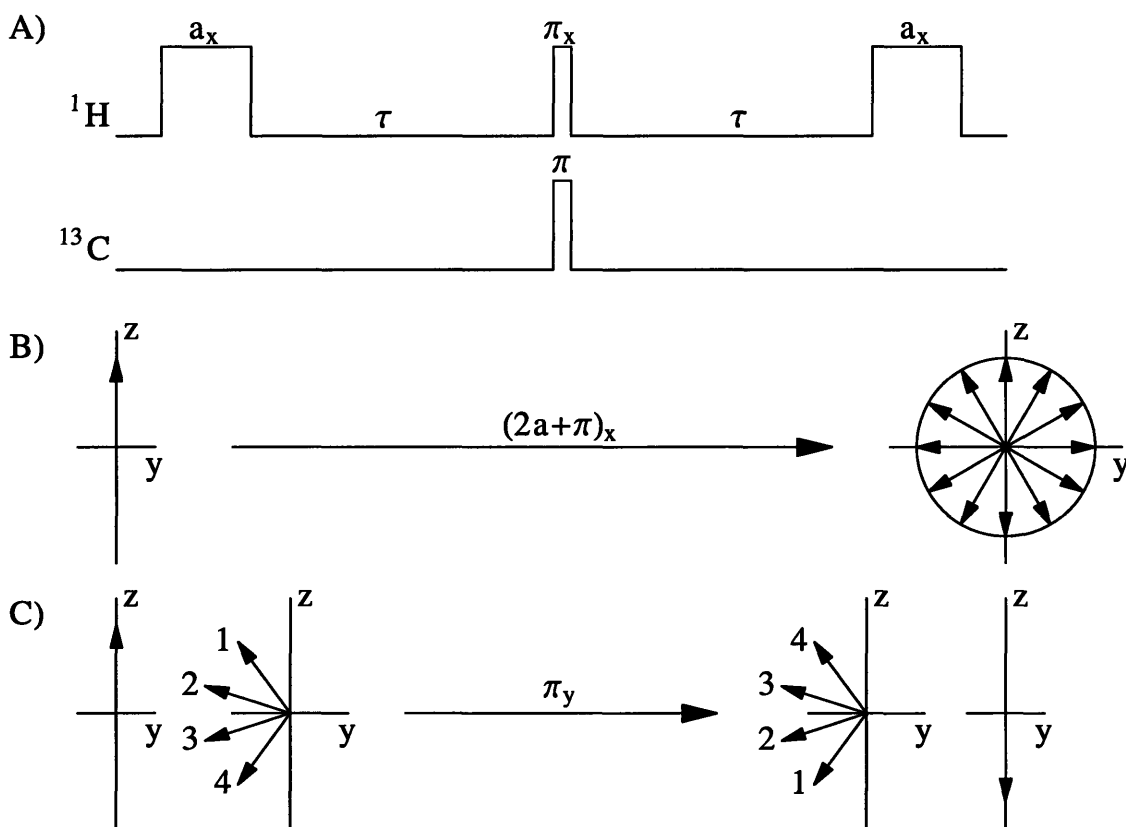


Figure 2-6: A) rBIRD<sub>x</sub>, the RF-gradient version of the BIRD sequence formed by replacing the  $(\pi/2)_x$  pulses of the standard BIRD sequence with RF gradient pulses of spatially-varying nutation angle  $a_x$ . B) Uncoupled magnetization with  $J = 0$  undergoes a spatially-varying RF nutation of angle  $(\pi + 2a)_x$ , and is thus spread uniformly throughout the Y-Z plane, yielding zero net signal. The vector diagrams schematize the spin states before the first gradient pulse, and after the second gradient. C) Coupled magnetization with  $2J\tau = 1$  is refocused in a rotary echo, and is entirely recovered. Spin packets 1-4 are located in regions of different RF field strengths and thus undergo different nutation angles  $a$ , yet they are all refocused together along the  $-z$  axis at the end of the sequence. The spin-packet orientations are shown before and after each gradient pulse.

during the gradient pulse. For uncoupled magnetization, the sequence acts simply as a single gradient pulse, dephasing the starting states ( $I_z$  and  $I_y$ ) with  $k_x = \pm 1$ , while preserving the spin-locked state ( $I_x$ ) with  $k_x = 0$ . For the coupled magnetization, however, the action of the central  $\tau - \pi_x - \tau$  unit as  $\pi_y$  inverts the effective coherence numbers  $k_x = \pm 1$  to  $k_x = \mp 1$ , causing evolution in the opposite sense during the second gradient pulse, and resulting in complete refocussing. The spin dynamics are thus analogous to those of a  $B_0$  gradient echo sequence  $G - \pi - G$ , once the spin states have been requantized along the appropriate gradient evolution axis.

### 2.4.2 RF Gradient TANGO

An RF-gradient version of the TANGO sequence can likewise be created to eliminate uncoupled magnetization while placing coupled spins in the transverse plane. In analogy with the standard sequence, the RF gradient version is formed simply as  $\alpha_x - \text{rBIRD}_x - \alpha_{-x}$ . As the  $a_x$  pulses in the central rBIRD unit are long RF-gradient pulses causing complete dephasing, they may be arbitrarily lengthened by  $\alpha_x$  to yield  $\text{rBIRD}_x - 2\alpha_{-x}$ , which is identical to the rBIRD sequence of Fig. 2-6A followed by a  $2\alpha_{-x}$  pulse to nutate the refocussed magnetization from -z into the transverse plane. The rBIRD component eliminates the uncoupled magnetization while placing coupled spins along -z, which are then caused to nutate into the transverse plane by the additional  $2\alpha$  rotation. For  $\alpha = \pi/4$ , the magnetization with  $2J\tau = 1$  is placed along -y, as in the standard sequence. The difference between the standard sequence and the RF-gradient modification is once again the elimination of the unwanted signal component with  $J = 0$ .

### 2.4.3 Miscalibration Error Terms

The standard BIRD and TANGO sequences are typically rather sensitive to incorrectly set pulse lengths and delays, which result in error terms that are antiphase or that may be transformed into antiphase states (and other multiple quantum coherences) by later RF pulses. The RF-gradient version, on the other hand, is relatively

forgiving of incorrectly set experimental parameters. Misset delays or pulse lengths result purely in attenuation of the desired terms, but do not create any multiple-quantum coherences. The ability to excite coherence transformations while simultaneously removing troublesome signal components is a property unique to RF gradients, which further supports their utility as the most natural means of selective excitation in this and other related pulse sequences. The error terms arising from a variety of miscalibrations are straightforward to calculate with the product operator formalism. Table 2.1 compares the transformations between spin states that occur with the standard BIRD<sub>x</sub> sequence and the RF-gradient rBIRD<sub>x</sub> modification.

To review, both sequences provide complete retention of the directly coupled magnetization components with  $2J\tau=1$ , acting merely as a net  $\pi_y$  rotation to invert  $I_x$  and  $I_z$  with no effect on  $I_y$ .  $\{I_x, I_y, I_z\}$  should thus transform to  $\{-I_x, I_y, -I_z\}$ . Conversely, for uncoupled magnetization with  $J=0$ , the BIRD<sub>x</sub> sequence acts as  $2\pi_x$ , leaving all components in their starting state, while the RF-gradient version rBIRD<sub>x</sub> performs spin-locking about the x-axis, completely eliminating all spin states not aligned along x.

The first row of the table presents the error terms arising from an incorrectly-set evolution delay  $\tau$ . Equivalently, it demonstrates the sensitivity of both sequences to the coupling strength  $J$ . If  $\tau$  is set incorrectly for the system of interest, or, as is commonly the case, the sample contains coupled partners with a range of coupling constants  $J$ , complete preservation of the coupled magnetization does not occur. The standard BIRD<sub>x</sub> sequence produces zero-quantum and antiphase error terms, which are eliminated by the RF gradient version. Furthermore, for a starting  $I_z$  spin state, the rBIRD sequence retains the desired final  $-I_z$  component with higher efficiency, varying with the coupling constant  $J$  as  $\sin^2(\pi J\tau)$  rather than as  $\cos(2\pi J\tau)$ . For small miscalibrations  $2J\tau = 1 - \epsilon/\pi$ , the retention efficiency of rBIRD decreases at half the rate of the standard sequence, varying as  $1 - \epsilon^2$  rather than  $1 - 2\epsilon^2$ .

The second and third rows, respectively, demonstrate the error terms that arise from miscalibration of the carbon  $\pi$  pulse and the proton  $\pi$  pulse, performed on resonance for magnetization coupled with  $2J\tau=1$ . The standard sequence again produces

Table 2.1: Comparison of error terms for the standard and RF-Gradient BIRD sequences.

Source of Error	BIRD <sub>x</sub>	rBIRD <sub>x</sub>
incorrect $\tau$	$I_x \quad I_x \cos[\pi J(2\tau)] + 2I_z S_z \sin[\pi J(2\tau)]$ $I_y \Rightarrow I_y$ $I_z \quad I_z \cos[\pi J(2\tau)] + 2I_x S_x \sin[\pi J(2\tau)]$	$I_x \quad I_x \cos[\pi J(2\tau)]$ $I_y \Rightarrow I_y \sin^2[\pi J\tau]$ $I_z \quad -I_z \sin^2[\pi J\tau]$
incorrect length of $\pi(^{13}C)$ : pulse length $(\pi + \epsilon)$ , $2J\tau = 1$	$I_x \quad -I_x \cos(\epsilon) - 2I_z S_z \sin(\epsilon)$ $I_y \Rightarrow I_y$ $I_z \quad -I_z \cos(\epsilon) + 2I_x S_x \sin(\epsilon)$	$I_x \quad -I_x \cos(\epsilon)$ $I_y \Rightarrow I_y \cos^2(\epsilon/2)$ $I_z \quad -I_z \cos^2(\epsilon/2)$
incorrect length of $\pi_x(^1H)$ : pulse length $(\pi + \epsilon)$ , $\Delta\omega = 0, 2J\tau = 1$	$I_x \quad -I_x \cos(\epsilon) - 2I_y S_y \sin(\epsilon)$ $I_y \Rightarrow I_y \cos(\epsilon) - 2I_x S_x \sin(\epsilon)$ $I_z \quad -I_z$	$I_x \quad -I_x \cos(\epsilon)$ $I_y \Rightarrow I_y \cos^2(\epsilon/2)$ $I_z \quad -I_z \cos^2(\epsilon/2)$

zero- and single-quantum error terms, which are again eliminated by the RF gradient technique, at the cost of a slight attenuation. The BIRD (or TANGO) sequence is commonly used to perform selective excitation of desired coupling partners as a first step in longer experiments. While it is possible to use phase cycling or gradient techniques to remove the miscalibration error terms that can be converted into undesired coherences by later pulses, the intrinsic elimination of these imperfections by the RF-gradient sequence is of advantage experimentally.

## 2.5 Experimental Results

Figure 2-7 shows experimental spectra of a chloroform sample, obtained on a Bruker 500 MHz Avance DRX spectrometer, using the probe whose nutation spectrum was shown in Fig. 2-1. The proton spectrum of chloroform in Fig. 2-7A reveals a large uncoupled central line that arises from protons bound to the non-magnetic  $^{12}C$  nuclei. This peak is flanked by the  $^{13}C$ -bound satellites, which are 200 times smaller than the uncoupled line since  $^{13}C$  has a natural abundance of only 1% (0.5% in each satellite). Fig. 2-7B shows the results of the standard BIRD sequence, followed by  $\pi/2$ , which selectively inverts the satellites, without affecting the uncoupled magnetization. Fig. 2-7C demonstrates that the RF-gradient BIRD sequence then yields substantial suppression of the uncoupled magnetization—by a factor of approximately 800—

reducing its magnitude to well below that of the satellites, which are refocused to a magnitude that is 80% that of Fig. 2-7B. The rBIRD sequence of Fig. 2-6A was repeated twice with the same RF phase in order to reduce attenuation of the desired magnetization due to molecular diffusion, and to ease the demands placed on the RF amplifier, as explained below in the discussion. It was then followed by a  $\pi/2$  pulse to place the satellites in the transverse plane. The nominal nutation caused by all four RF-gradient pulses was 500 complete cycles, resulting in substantial suppression due to the coil's residual  $B_1$  inhomogeneity.

## 2.6 Discussion

While the RF gradient sequence causes substantial suppression after a single-shot experiment, residual uncoupled magnetization does survive the sequence as a result of imperfect dephasing by the RF-gradients. Conversely, not all of the magnetization with the correct coupling strength  $2J\tau=1$  is refocused. There are several experimental factors responsible for both the incomplete suppression and the imperfect refocussing.

Imperfect refocussing of coupled magnetization occurs primarily as a result of molecular diffusion in those regions of the sample where the local RF gradient is strongest. During the  $2\tau$  delay between the RF-gradient pulses, and during the gradient pulses themselves, diffusion causes molecular displacements to nearby regions of different  $B_1$  field strength, which results in incomplete refocussing by the second gradient pulse. If the RF-gradient were linear, the diffusive attenuation factor during this sequence would be the same as that of a standard pulsed-gradient spin echo (PGSE) diffusion experiment using static  $B_0$  gradient [15]. Linear RF-gradients have in fact been used successfully in diffusion experiments by making use of this correspondence [11]. For the RF-gradient BIRD sequence, the predicted attenuation factor is thus

$$A = \exp\{-(\gamma g \delta)^2 D(2\tau + 2\delta/3)\}, \quad (2.4)$$

where  $D$  is the diffusion constant,  $\delta$  is the length of each linear gradient pulse, and  $2\tau$

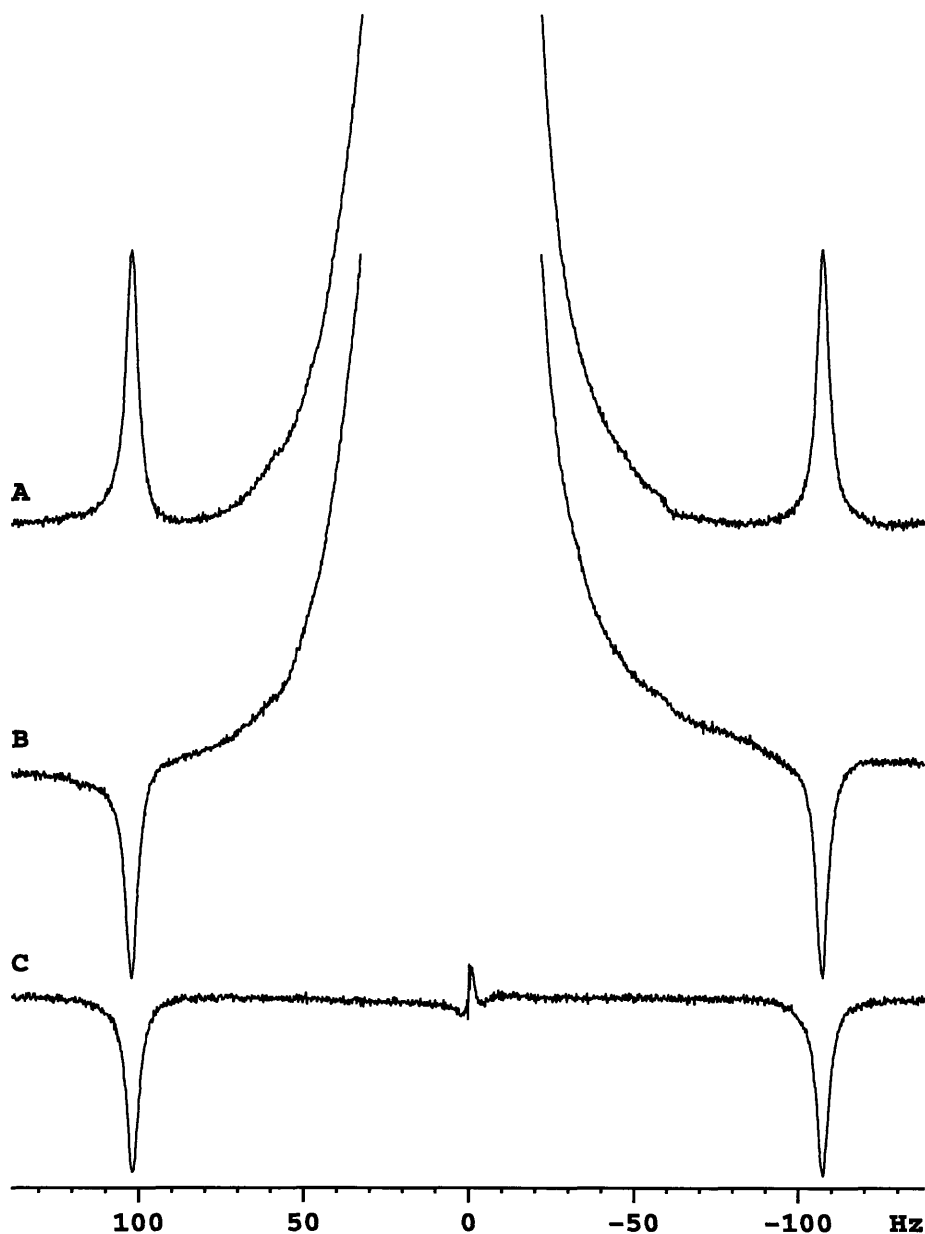


Figure 2-7: A sample of 10%  $\text{CHCl}_3$  in  $\text{CDCl}_3$  was used to investigate the RF gradient BIRD sequence (rBIRD) on a Bruker 500 MHz DRX spectrometer. Chromium acetylacetonate (CrAcAc) was added to reduce  $T_1$  to 4 seconds. A) Chloroform spectrum, expanded to show the satellites. B) The standard  $\text{BIRD}_x$  sequence, showing satellite inversion. C) The result of  $\text{rBIRD}_x - \text{rBIRD}_x - (\pi/2)_x$ , demonstrating significant suppression of the central peak with 80% refocussing of the satellites, as compared with B). The RF-gradient pulses had duration  $\alpha_x = 4.5\text{msec}$ , and the  $\pi/2$  pulse duration was  $9\mu\text{sec}$ . All three sequences were performed on resonance. B) and C) use  $\tau = 2.38\text{msec}$ , corresponding to  $J_{CH} = 210\text{Hz}$ .



is the separation between the defocussing and refocussing gradient pulses. However, since the RF gradients are not linear across the sample in the coil used in this work, this attenuation factor does not apply globally across the entire sample but must be summed over local regions of different RF-gradient strength. Greater attenuation occurs in sample regions experiencing a stronger gradient. Nonetheless, solving for  $g$  in Eq. [2.4] with  $D = 2.4\mu\text{m}^2/\text{msec}$  for chloroform, and with the observed signal amplitude of 88% for  $\delta = 4.5$  msec and  $\tau = 2.4$  msec, yields an effective linear-gradient strength of approximately 7 Gauss/cm, which corresponds to a variation in nutation frequency of 30 kHz/cm. The central sample regions, where the RF field is most uniform, contribute very little to the attenuation, while those regions near the top and bottom of the coil experience a much higher RF gradient and thus attenuate more rapidly. For the coil used here, with a nominal nutation frequency of 27 kHz, a  $B_1$  gradient larger than 7 Gauss/cm can reasonably be expected over a large enough fraction of the sample to account for the observed attenuations: Two-dimensional nutation experiments (nutation frequency vs z-position) reveal that near the ends of a 5 mm diameter, 1 cm long homogeneous coil, the nutation frequency falls rapidly from near-maximum to near-zero over a distance of only a couple millimeters. While this diffusive attenuation is noticeable for a rapidly-diffusing molecule such as chloroform, it would be much less significant for larger molecules which diffuse more slowly, and which would thus refocus more completely.

The residual uncoupled signal that survives the RF-gradient BIRD sequence is due primarily to incomplete averaging by the RF-gradients. As discussed above, the inverse fourier transform of the coil's nutation spectrum yields the expected decay envelope of uncoupled magnetization as a function of the RF-gradient pulse length. To achieve better averaging, one must either apply longer RF-gradient pulses, repeat the experiment serially, or use an RF coil with a larger  $B_1$  inhomogeneity.

While it is possible to increase the RF gradient pulse-lengths, the long high power pulses required when using a "homogeneous" coil do pose some experimental challenges. The frequency-selectivity of long RF pulses could limit the spectral width over which suppression is effective. RF power deposition in the sample may also be

of concern for certain samples. The most significant issues, however, depend upon the probe and RF amplifier used. During the pulse, an RF phase shift or a gradual decline in the power output of the RF amplifier may appear. Alternatively, heating of the probe may occur, thus altering the probe's Q-factor which may cause variations in the phase or intensity of the RF transmitted to the sample. These RF amplitude and phase effects may be corrected by adjusting the lengths and phases of the refocussing gradient pulses. For the hardware used here, the dominant effect was a slight droop in the amplifier output, easily corrected by lengthening the second gradient pulse (by about 1%).

As an alternative to the long-pulse approach, it is possible instead to use shorter RF-gradient pulses while repeating the sequence twice or more in series, thus producing further dephasing of the uncoupled magnetization with each repetition. This approach decreases the average RF duty cycle, potentially easing several of the difficulties associated with long RF pulse lengths. Furthermore, as the desired magnetization component is refocussed at the end of each repetition, losses due to molecular diffusion are reduced, just as diffusive attenuation factors can be reduced with a Carr-Purcell cycle. This is indeed observed experimentally — a single rBIRD sequence with 9 msec gradient pulses refocusses only 62% of the desired signal, while two serial repetitions using 4.5msec pulses yield nearly 80% refocussing (close to the square of the 88% factor from a single repetition using 4.5msec gradients). For additive suppression effects, the sequence must be applied with the same RF phase during subsequent repetitions. Shifting the RF phase by  $90^\circ$  during a second repetition causes only half of the original uncoupled magnetization to dephase further, while the other half is instead refocussed.

Finally, suppression factors may be improved by using a probe with an RF gradient coil specifically designed with enhanced  $B_1$  inhomogeneity to produce better averaging over the sample volume [4, 11]. This broadens the nutation spectrum, producing superior dephasing with shorter RF gradient pulses, and thus eliminates the pulse duration issues discussed above. Sequences employing RF gradients typically require homogeneous pulses as well as the gradient pulses to retain sensitivity. The rBIRD

sequence for example, requires fairly homogeneous  $\pi$  pulses to achieve full refocussing. As a result, RF-gradient probes typically contain both a homogeneous coil and a gradient coil, either with separate RF amplifiers for each coil [11], or with active switching between the two coils [4].

When RF-gradient techniques are performed over a range of resonance offsets, it is difficult to achieve uniformly excellent suppression factors. This occurs because a portion of the starting magnetization is spin-locked due to the slight tilt of the effective RF-axis out of the transverse plane. The RF-gradient dephases only the magnetization component that is orthogonal to the RF axis, while spin-locking the parallel component. Figure 2-8 demonstrates this effect on a water sample over a range of resonance offset values. For a given resonance offset  $\Delta\omega$  and a given RF field strength causing a nutation frequency  $\omega_1$ , the tilted effective RF axis is oriented at an angle  $\theta = \tan^{-1}(\Delta\omega/\omega_1)$  from the transverse plane. The residual spin-locked fraction is simply the projection of the starting magnetization vector onto the RF axis, and is thus proportional to  $\sin(\theta) \approx \Delta\omega/\omega_1$ , for  $\Delta\omega \ll \omega_1$ . This accurately predicts the observed magnitude of the spin-locked magnetization in Fig. 2-8, corresponding to  $\approx 2\%$  of the magnetization at an offset of 500 Hz for the RF coil used here with an average  $\omega_1 \approx 27$  kHz.

When applying the RF-gradient sequence off resonance, as for a sample spanning a large spectral width, this spin-locked component must be eliminated. The  $\text{rBIRD}_x$  sequence may be followed by a  $(\pi/2)_{-y}$  pulse to nutate the spin-locked component from the x-axis back to -z, although this approach leaves net uncoupled magnetization which may be significant if later manipulations are planned. This residual magnetization may instead be eliminated by incorporating a two-step phase cycle which adds the results of  $\text{rBIRD}_x - (\pi/2)_y$  and  $\text{rBIRD}_{-x} - (\pi/2)_y$ . Alternatively, the usual  $(\pi/2)_x$  pulse may be applied, followed by a brief RF-gradient pulse along y to dephase the previously spin-locked component while spin-locking the coupled magnetization component. This requires that the orthogonal y-gradient pulse be made short compared to the total preceding RF-gradient length in order to avoid refocussing half the magnetization.

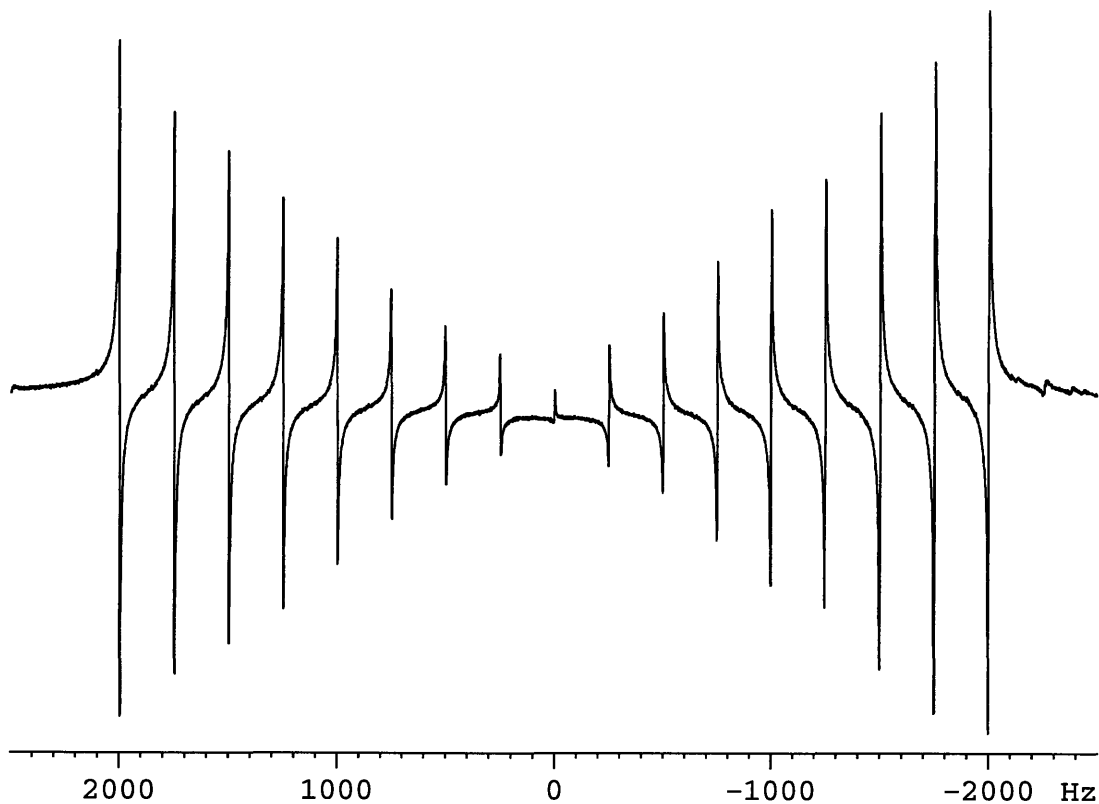


Figure 2-8: The residual magnetization that remains after an RF gradient pulse due to spin-locking about the tilted effective RF axis. Starting equilibrium magnetization along  $z$  is dephased with a 10 msec RF gradient pulse. The resonance offset is varied in intervals of 250Hz, and the results added. The phasing used produces an absorptive signal after a  $\pi/2$  pulse. The signal remaining after the RF gradient pulse is purely dispersive, as this magnetization component is spin-locked about the RF axis. As expected, this spin-locked component reverses phase about  $\Delta\omega = 0$ , and grows linearly with offset. It corresponds to approximately 2% of the equilibrium magnetization at an offset of 500 Hz.

The other approach to avoid spin-locking is to place the starting spin state orthogonal to the the tilted effective RF-axis. A composite pulse [16] compensated for resonance offset could be used to nutate the starting  $I_z$  state to  $I_y$  before applying the gradient sequence with an RF-phase of x. A different, elegant solution was presented by Canet et al. [17], in which the first gradient pulse is preceded by  $(\pi/2)_x - \tau - (\pi/2)_{-x}$ . During the  $\tau$  interval, chemical shift evolution occurs, so for small offsets  $\Delta\omega \ll \omega_1$ , the sequence may be represented as  $(\pi/2)_x - (\Delta\omega\tau)_z - (\pi/2)_{-x} = (-\Delta\omega\tau)_y$ . By choosing  $\tau = 1/\omega_1$ , the magnetization vector then nutates to a position tilted by  $-\Delta\omega/\omega_1 \approx -\theta$  from the z-axis, orthogonal to the effective RF-axis of the gradient pulse that follows. More complete dephasing thus occurs over a larger range of offsets.

## 2.7 Conclusions

By combining the steps of coherence pathway transformation and spatial modulation, RF gradients are ideally suited for certain types of selective excitation sequences, such as the RF gradient BIRD/TANGO sequence presented here. The incorporation of RF gradients may be achieved without altering the form of the pulse sequence, while at the same time eliminating not only the target magnetization component (here the uncoupled magnetization with  $J=0$ ) but also a variety of coherences that normally arise from imperfectly set pulse lengths and evolution delays. RF gradients pose a variety of experimental challenges—especially when using the residual  $B_1$  inhomogeneity of a nominally homogeneous coil. Nonetheless, rBIRD is capable of producing substantial suppression factors in eliminating uncoupled magnetization, as predicted by theory. General application of these techniques would ideally employ specially designed RF-gradient coils to provide more complete elimination of unwanted magnetization components while at the same time alleviating experimental challenges associated with the use of long high power RF-gradient pulses.

# References

- [1] J. Keeler, R. T. Clowes, A. L. Davis, and E. D. Laue, "Pulsed-field gradients: Theory and practice," *Methods in Enzymology*, vol. 239, pp. 145–207, 1994.
- [2] D. Canet, J. Brondeau, E. Mischler, and F. Humbert, "Solvent suppression by use of a DANTE train of  $B_1$ -gradient pulses," *Journal of Magnetic Resonance, Series A*, vol. 105, pp. 239–244, 1993.
- [3] W. E. Maas and D. G. Cory, "Solvent suppression by radiofrequency gradients," *Journal of Magnetic Resonance, Series A*, vol. 106, pp. 256–259, 1994.
- [4] W. E. Maas, F. Laukien, and D. G. Cory, "Coherence selection by radiofrequency gradients," *Journal of Magnetic Resonance, Series A*, vol. 103, pp. 115–117, 1993.
- [5] P. Mutzenhardt, J. Brondeau, and D. Canet, "COSY experiments and solvent suppression with  $B_1$  gradients," *Journal of Magnetic Resonance, Series A*, vol. 108, pp. 110–115, 1994.
- [6] C. J. R. Counsell, M. H. Levitt, and R. R. Ernst, "The selection of coherence-transfer pathways by inhomogeneous z-pulses," *Journal of Magnetic Resonance*, vol. 64, pp. 470–478, 1985.
- [7] J. Brondeau, D. Boudot, P. Mutzenhardt, and D. Canet, "The equivalent of the DQF-COSY experiment, with one transient per  $t_1$  value, by use of  $B_1$  gradients," *Journal of Magnetic Resonance*, vol. 100, pp. 611–618, 1992.

- [8] D. G. Cory, F. H. Laukien, and W. E. Maas, "Double-quantum-filtered-COSY  $B_1$ -gradient experiments," *Journal of Magnetic Resonance, Series A*, vol. 105, pp. 223–229, 1993.
- [9] W. E. Maas and D. G. Cory, "Heteronuclear correlation spectroscopy with RF gradients," *Journal of Magnetic Resonance, Series A*, vol. 112, pp. 229–236, 1995.
- [10] C. Emetarom, T. Hwang, G. Mackin, and A. J. Shaka, "Isotope editing of NMR spectra. excitation sculpting using BIRD pulses," *Journal of Magnetic Resonance, Series A*, vol. 115, pp. 137–140, 1995.
- [11] D. Canet, B. Diter, A. Belmajdoub, J. Brondeau, J. C. Boubel, and K. Elbayed, "Self-diffusion measurements using a radiofrequency field gradient," *Journal of Magnetic Resonance*, vol. 81, pp. 1–12, 1989.
- [12] J. R. Garbow, D. P. Weitekamp, and A. Pines, "Bilinear rotation decoupling of homonuclear scalar interactions," *Chemical Physics Letters*, vol. 93, no. 5, pp. 504–509, 1982.
- [13] S. C. Wimperis and R. Freeman, "An excitation sequence which discriminates between direct and long-range CH coupling," *Journal of Magnetic Resonance*, vol. 58, pp. 348–353, 1984.
- [14] Y. Zhang, W. E. Maas, and D. G. Cory, "Analysis of homonuclear RF gradient NMR spectroscopy," *Molecular Physics*, vol. 86, no. 3, pp. 347–358, 1995.
- [15] E. . Stejskal and J. E. Tanner, "Spin diffusion measurements: Spin echoes in the presence of a time-dependent field gradient," *Journal of Chemical Physics*, vol. 42, no. 1, pp. 288–292, 1965.
- [16] M. H. Levitt, "Composite pulses," *Progress in NMR Spectroscopy*, vol. 18, pp. 61–122, 1986.

- [17] P. Mutzenhardt, J. Brondeau, and D. Canet, "Selective COSY experiments with  $B_1$  gradients," *Journal of Magnetic Resonance, Series A*, vol. 117, pp. 278–284, 1995.



# Chapter 3

## Shimming a High Resolution

## MAS Probe<sup>1</sup>

### 3.1 Introduction

Magic angle sample spinning (MAS) is developing as a powerful tool for the study of semi-solids, including the important examples of combinatorial chemistry [1] and excised tissues [2]. These recent applications have been facilitated by the development of high resolution MAS probes where care is taken to use susceptibility matched materials, and MAS gradient probes [3] which permit excellent water suppression and gradient selection of coherence pathways. Here, a systematic approach to shimming these high resolution probes is discussed, which takes into account the different symmetries of the normal shim coils and the MAS experiment.

Since the NMR resonance frequency is directly proportional to the magnetic field strength, the NMR line shape reflects the variation of the magnetic field strength over the sample volume. This rather obvious conclusion has led to the requirement that any high resolution NMR experiment be preceded by a tedious period of shimming, and a culture has been established around this art, along with a hierarchy of methods aimed at obtaining the best field homogeneity. An abundance of manual, computer-

---

<sup>1</sup>A. Sodickson and D. G. Cory, "Shimming a high resolution MAS probe," Submitted to the *Journal of Magnetic Resonance*, 1997.

assisted and gradient-based mapping methods are established for the high resolution liquid state experiment that may provide excellent resolution for the initiate (useful general references are [4, 5]).

The case of shimming an MAS probe is distinct from the liquid state geometry, both because of the high rates of sample spinning involved and because the spinning axis does not lie along the field direction. Very early, Bloch [6] pointed out that mechanical motion can be used to coherently average selected spatial variations of the magnetic field. A coherent modulation of an inhomogeneous interaction will subdivide the spectrum into a sharpened central band and a collection of sidebands. The intensity of these sidebands vary as Bessel functions whose arguments are proportional to the residual off-axis inhomogeneity divided by the spinning speed. If the modulation frequency is on the order of the field inhomogeneity then the sidebands have an observable intensity. Hence shim sets include two categories of correction coils, the zonal shims which are cylindrically symmetric about the sample axis and are thus not averaged by the spinning, and the tesseral shims which possess lesser symmetry, whose task it is to reduce the off-axis field variations sufficiently that sidebands are not troublesome. With the importance today of multi-dimensional experiments, and a desire to avoid  $t_1$  noise [7], it has become routine to study stationary samples, and the zonal and tesseral shims may be weighted more equally.

In MAS experiments, the spinning is employed for coherent averaging of contributions to the NMR linewidth from susceptibility variations [8] and residual dipolar couplings [9]. The spinning rates are typically at least a few kilohertz, much faster than the inhomogeneous linewidth due to spatial variations in the field. In this case, the amplitudes of the sidebands are always small, and shimming may be focused on that set of shims that have cylindrical symmetry about the MAS spinner axis. The most natural approach to shimming for high resolution MAS probes is thus to use a set of zonal shims whose symmetry axis is oriented along the spinner axis.

$$\begin{aligned}
B_{z^0} = T_0 &= 1 \\
B_{z^1} = T_1 &= z \\
B_{z^2} = 2T_2 &= 2z^2 - (x^2 + y^2) \\
B_{z^3} = 2T_3 &= 2z^3 - 3z(x^2 + y^2) \\
B_{z^4} = 8T_4 &= 8z^4 - 24z^2(x^2 + y^2) + 3(x^2 + y^2)^2 \\
B_{z^5} = 48T_5 &= 6[8z^5 - 40z^3(x^2 + y^2) + 15z(x^2 + y^2)^2]
\end{aligned}$$

Table 3.1: Lab frame zonal shims in cartesian coordinates.

## 3.2 Standard Lab-Frame Shim Geometries

Detailed descriptions of typical shim coils have been presented elsewhere [4, 10]. They are designed to produce z-components of the magnetic field whose magnitudes vary as spherical harmonics. The shims may be described in the laboratory frame as being composed of zonal harmonics—those that have cylindrical symmetry about z—and tesseral harmonics, which vary azimuthally about the sample. They are presented in cartesian coordinates in Tables 3.1 and 3.2, and are proportional to the surface spherical harmonic basis functions

$$\begin{aligned}
T_n &= r^n P_n(\cos \theta), \\
T_{nm}^{\begin{pmatrix} e \\ o \end{pmatrix}} &= r^n P_{nm}(\cos \theta) \begin{pmatrix} \cos m\phi \\ \sin m\phi \end{pmatrix},
\end{aligned} \tag{3.1}$$

where  $P_n$  and  $P_{nm}$  are, respectively, the Legendre polynomials and the associated Legendre polynomials. Note that the angular dependence of the even and odd tesseral basis functions comprise linear combinations of the standard  $Y_{n,\pm m}$  spherical harmonics whose azimuthal dependence is instead  $e^{\pm im\phi}$ .  $T_n$  and  $T_{nm}$  form a complete orthonormal basis set. They are truly orthogonal only over a spherical volume, however, resulting in the unfortunate interactions between shims that are observed when the shim fields are integrated over cylindrical sample geometries. Correction fields of higher order  $n$  are required to eliminate field inhomogeneities that vary as higher orders of any given spatial coordinate.

The shims presented in Tables 3.1 and 3.2 cover the 18 nominal shims found in

First Order :

$$B_x = T_{11}^e = x$$

$$B_y = T_{11}^o = y$$

Second Order :

$$B_{zx} = \frac{1}{3}T_{21}^e = zx$$

$$B_{zy} = \frac{1}{3}T_{21}^o = zy$$

$$B_{x^2-y^2} = \frac{1}{3}T_{22}^e = (x^2 - y^2)$$

$$B_{xy} = \frac{1}{6}T_{22}^o = xy$$

Third Order :

$$B_{z^2x} = \frac{2}{3}T_{31}^e = x(4z^2 - (x^2 + y^2))$$

$$B_{z^2y} = \frac{2}{3}T_{31}^o = y(4z^2 - (x^2 + y^2))$$

$$B_{z(x^2-y^2)} = \frac{1}{15}T_{32}^e = z(x^2 - y^2)$$

$$B_{xyz} = \frac{1}{30}T_{32}^o = xyz$$

$$B_{x^3} = \frac{1}{15}T_{33}^e = x^3 - 3xy^2$$

$$B_{y^3} = \frac{1}{15}T_{33}^o = 3yx^2 - y^3$$

Table 3.2: Lab frame tesseral shims in cartesian coordinates.

wide-bore systems and in older standard bore shim sets. As shown in the tables, the zonal shims are complete through fifth order, while the tesseral shims are only complete through third order. The reasons are two-fold; the number of tesseral shims grow as twice the order, and the shim sets are optimized for correcting field variations along the long axis of the sample. A complete set of shims through fifth order numbers 36 and the extra shims add greatly to the complexity of the shim set and to the overall currents used for correcting the field. Figure 3-1 shows a collage of selected shims demonstrating the underlying symmetries of the shims and their increasing complexity as a function of order. The displayed surfaces are the nodal planes of the correction fields.

### 3.3 Shims in the Tilted MAS Frame

The desired set of zonal shims along the MAS axis could, of course, be implemented by a new set of gradient windings, but there is no need since through third order a complete set of spherical harmonic fields exists. Since the lab frame correction fields form a complete set of basis functions, any desired field profile up to third order may be expressed as a linear combination of the lab frame shims. For ease of shimming under MAS conditions, it is only necessary to transform the existing shims into a set that is oriented along the MAS spinner axis, and then to explore the extent of averaging introduced by MAS. To third order the shim set is complete, and may thus be transformed into a set at any orientation. The transformation from the laboratory frame into the MAS axis system depends on their azimuthal relationship, so for the results that follow the z-axis of this tilted frame has been arbitrarily chosen to be aligned at  $[\sqrt{2/3}, 0, \sqrt{1/3}]$  relative to the laboratory frame. In other words, the MAS spinner axis is assumed to be aligned with the x-axis of the lab frame shim set.

For this spinner orientation, the tilted MAS reference frame and the lab frame share a common y-axis, and a rotation about this axis through  $-\theta_m$  transforms the MAS coordinates to lab frame coordinates. Any physical rotation of a spherical harmonic results in a linear combination of harmonics of the same order but all  $m$ -

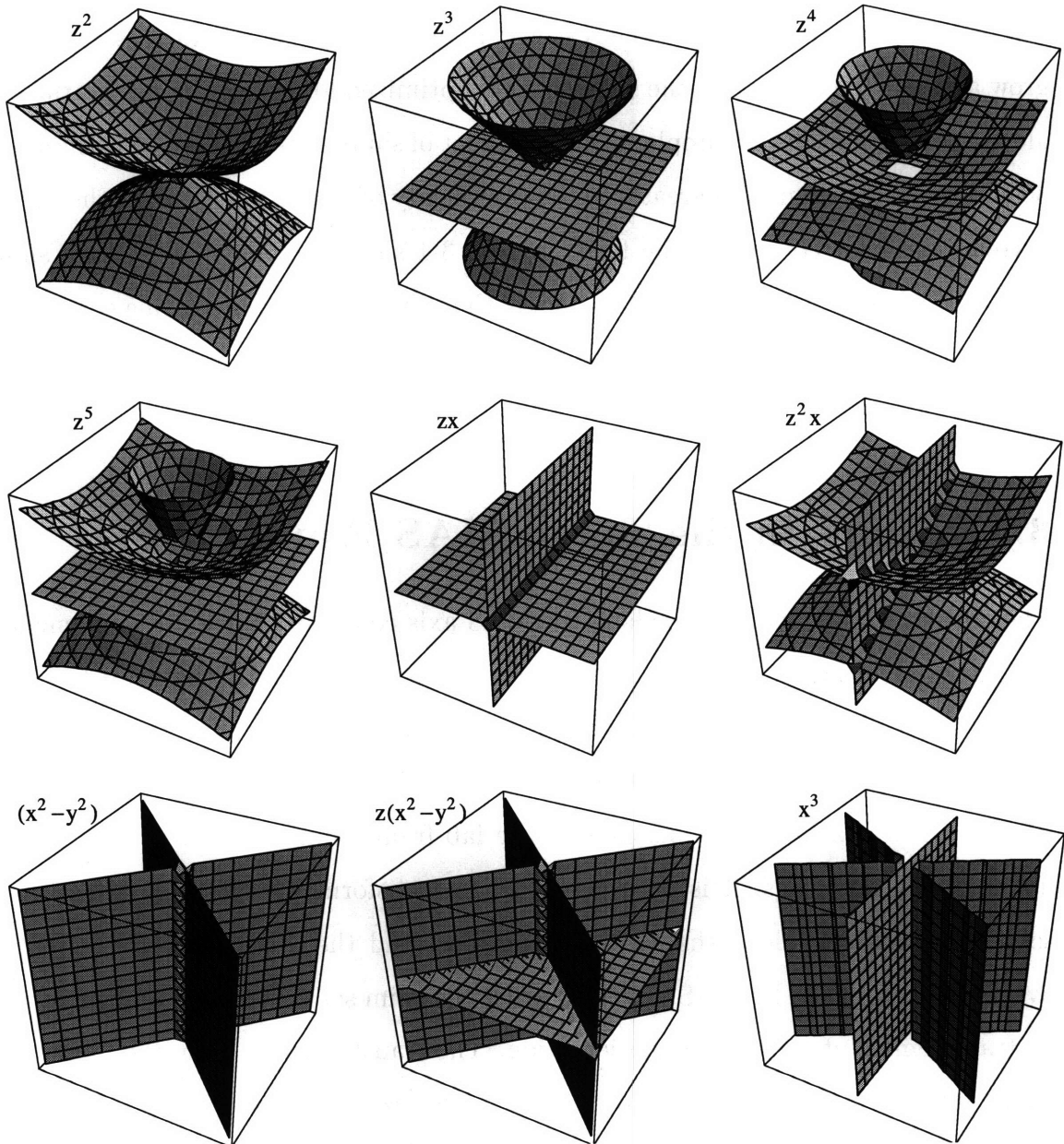


Figure 3-1: Isometric plots of the nodal surfaces for selected lab-frame shims. The fields shown correspond, from left to right, to the zonal shims  $z^2$ ,  $z^3$ ,  $z^4$ ,  $z^5$ , and the even-symmetry tesseral shims  $zx$ ,  $z^2x$ ,  $(x^2 - y^2)$ ,  $z(x^2 - y^2)$ , and  $x^3$ . Note in particular that the nodal surface for the  $z^2$  shim includes the magic angle. The odd-symmetry tesseral shims may be visualized simply by rotating the plots for the corresponding even-symmetry shims by  $\pi/2m$ , where  $m = 1$  for  $zy$  and  $z^2y$ ,  $m = 2$  for  $xy$  and  $xyz$ , and  $m = 3$  for  $y^3$ .

values. In addition, the transformed  $T_{nm}$  state will include contributions only from states that share the same even or odd azimuthal symmetry:

$$\begin{aligned} T_{nm}^e(r, \theta, \phi) &= \sum_{m'=0}^n c_{m'} T_{nm'}^e(r', \theta', \phi'), \\ T_{nm}^o(r, \theta, \phi) &= \sum_{m'=1}^n c_{m'} T_{nm'}^o(r', \theta', \phi'). \end{aligned} \quad (3.2)$$

Furthermore, from the addition formula of spherical harmonics it is straightforward to derive the transformations for the zonal shims:

$$T_n(r, \theta, \phi) = \sum_{m=0}^n \epsilon_m \frac{(n-m)!}{(n+m)!} P_{nm}(\cos \theta_m) T_{nm}(r', \theta', \phi'), \quad (3.3)$$

where  $\epsilon_m = 2 - \delta_{m,0}$ , and the unprimed MAS frame transforms to the primed lab frame simply by a rotation through  $-\theta_m$  about their shared y-axes. The tesseral shims may be transformed using the Wigner rotation matrix elements  $\mathcal{D}_{m,m'}(0, -\theta_m, 0)$ . Alternatively, the coordinate transformations may of course be performed in cartesian coordinates, and the results decomposed into the lab frame shim fields of the same order and symmetry as the original tilted-frame shim.

Table 3.3 presents the spherical harmonic shims in the magic-angle-tilted reference frame, expressed in terms of the normal lab frame shims. Again, note that these are complete to third order, but there is no possible transformation for the fourth and fifth order zonal spins, *vide infra*. So under non-spinning conditions with the sample tilted at the magic angle, the field may be shimmed to third order in exactly the manner accustomed from high resolution work, provided that the appropriate subset of shims are varied in concert. The fourth and fifth order lab frame shims, if varied, will contribute to the desired zonal shims in the tilted frame, although they will of course also transform into other harmonic fields of the same order and even azimuthal symmetry.

### 3.4 Simplifications due to Sample Spinning

Under spinning conditions, only the zonal shims in the tilted frame will contribute and hence shimming becomes simpler. As discussed above, spinning sidebands are negligible since the spinning rate is much greater than the line broadening due to field inhomogeneities. The only surviving shims are thus the zonal shims  $B_{z^1}^{tilt}$  through  $B_{z^5}^{tilt}$  in the spinning frame, which, being invariant to rotation about the spinner axis, still transform to the same linear combination of lab frame shims listed in Table 3.3. As none of the odd-symmetry shims contribute to the zonal harmonics in the tilted frame,  $B_y^{lab}$ ,  $B_{zy}^{lab}$ ,  $B_{xy}^{lab}$ ,  $B_{z^2y}^{lab}$ ,  $B_{xyz}^{lab}$ ,  $B_y^{lab}$  and are all averaged completely by spinning, and current to these shims may thus be eliminated when spinning. In fact, spinning quickly about any axis in the x-z plane would eliminate contributions from these lab frame shims, as the x-z plane is one of the nodal planes for each of these shims. In addition, the  $B_{z^2}^{lab}$  shim has absolutely no influence on the NMR lineshape under MAS, due to the specific choice of the magic angle for the spinning axis. As seen in Fig. 3-1, this shim contains a nodal plane exactly along the magic angle—the field varies as the 2nd Legendre polynomial  $P_2(\cos \theta) = (3 \cos^2 \theta - 1)/2$ , which of course disappears at the magic angle  $\theta_m = \cos^{-1}(1/\sqrt{3})$ .

Of particular interest are the fourth and fifth order shims, for which the lab frame tesseral components were not implemented, so the only possibility is to employ the residual variation of these zonal shims. These lab frame shims transform into the MAS-frame zonal shims, which survive spinning, and into MAS-frame tesseral shims of the same order, which are eliminated by spinning. From Equation 3.3,  $B_{z^4}^{lab}$  and  $B_{z^5}^{lab}$  transform into  $B_{z^4}^{tilt}$  and  $B_{z^5}^{tilt}$  with efficiencies of  $-7/18$  and  $-1/6\sqrt{3}$ , respectively. The absence of the other fourth and fifth order lab frame shims simply reduces the efficiency with which the MAS-frame correction fields may be produced. Nonetheless, MAS-frame zonal shims through fifth order are all created perfectly when spinning, as spinning itself serves to eliminate all but the zonal contributions.

This observation in fact leads to a simplified approach to shimming when spinning. While varying the shim fields in concert according to the linear combinations of



First Order :

	$B_z^{\text{lab}}$	$B_x^{\text{lab}}$	$B_y^{\text{lab}}$
$B_z^{\text{tilt}}$	$+\frac{1}{\sqrt{3}}$	$-\frac{\sqrt{2}}{\sqrt{3}}$	
$B_x^{\text{tilt}}$	$+\frac{\sqrt{2}}{\sqrt{3}}$	$+\frac{1}{\sqrt{3}}$	
$B_y^{\text{tilt}}$			$+1$

Second Order :

	$B_{z^2}^{\text{lab}}$	$B_{zx}^{\text{lab}}$	$B_{zy}^{\text{lab}}$	$B_{(x^2-y^2)}^{\text{lab}}$	$B_{xy}^{\text{lab}}$
$B_{z^2}^{\text{tilt}}$		$-2\sqrt{2}$		$+1$	
$B_{zx}^{\text{tilt}}$	$+\frac{\sqrt{2}}{6}$	$-\frac{1}{3}$		$-\frac{\sqrt{2}}{6}$	
$B_{zy}^{\text{tilt}}$			$+\frac{1}{\sqrt{3}}$		$-\frac{\sqrt{2}}{\sqrt{3}}$
$B_{(x^2-y^2)}^{\text{tilt}}$	$+\frac{1}{3}$	$+\frac{2\sqrt{2}}{3}$		$+\frac{2}{3}$	
$B_{xy}^{\text{tilt}}$			$+\frac{\sqrt{2}}{\sqrt{3}}$		$+\frac{1}{\sqrt{3}}$

Third Order :

	$B_{z^3}^{\text{lab}}$	$B_{z^2x}^{\text{lab}}$	$B_{z^2y}^{\text{lab}}$	$B_{z(x^2-y^2)}^{\text{lab}}$	$B_{xyz}^{\text{lab}}$	$B_{x^3}^{\text{lab}}$	$B_{y^3}^{\text{lab}}$
$B_{z^3}^{\text{tilt}}$	$-\frac{2}{3\sqrt{3}}$	$-\frac{1}{\sqrt{6}}$		$+\frac{5}{\sqrt{3}}$		$-\frac{5}{3\sqrt{6}}$	
$B_{z^2x}^{\text{tilt}}$	$\frac{2}{3\sqrt{3}}$	$-\frac{\sqrt{3}}{2}$				$+\frac{5}{6\sqrt{3}}$	
$B_{z^2y}^{\text{tilt}}$			$+\frac{1}{6}$		$-\frac{10\sqrt{2}}{3}$		$+\frac{5}{6}$
$B_{z(x^2-y^2)}^{\text{tilt}}$	$-\frac{1}{3\sqrt{3}}$					$-\frac{\sqrt{2}}{3\sqrt{3}}$	
$B_{xyz}^{\text{tilt}}$			$+\frac{\sqrt{2}}{12}$		$-\frac{1}{3}$		$-\frac{\sqrt{2}}{12}$
$B_{x^3}^{\text{tilt}}$	$\frac{\sqrt{2}}{3\sqrt{3}}$	$+\frac{1}{2\sqrt{3}}$		$+\frac{2\sqrt{2}}{\sqrt{3}}$		$+\frac{5}{6\sqrt{3}}$	
$B_{y^3}^{\text{tilt}}$			$+\frac{1}{2}$		$+2\sqrt{2}$		$+\frac{1}{2}$

Fourth Order :

$$B_{z^4}^{\text{tilt}} = -\frac{7}{18}B_{z^4}^{\text{lab}} + \sum_{m=1}^4 c_m T_{4m}$$

Fifth Order :

$$B_{z^5}^{\text{tilt}} = -\frac{1}{6\sqrt{3}}B_{z^5}^{\text{lab}} + \sum_{m=1}^5 c_m T_{5m}$$

Table 3.3: Spherical harmonic shims in the tilted frame expressed as linear combinations of laboratory frame shims.

Table 3.3 will produce the proper correction field geometries even when the sample is stationary, alternatively, when spinning, one need only choose a single lab frame shim to substitute for the appropriate MAS-frame  $n$ th order zonal shim  $B_{z^n}^{\text{tilt}}$ . Choosing the terms that contribute with the highest efficiency in the linear combinations of Table 3.3 (and including the weighting factors from Table 3.2), this suggests the use of  $B_x^{\text{lab}}$ ,  $B_{zx}^{\text{lab}}$ ,  $B_{z^2x}^{\text{lab}}$ ,  $B_{z^4}^{\text{lab}}$ , and  $B_{z^5}^{\text{lab}}$  as the surrogate  $n$ th order shims. If these coils cannot produce strong enough fields for adequate shimming, current may be applied to the other shims in the linear combination, with the appropriate sign. Of course, these choices and the weighting factors in Table 3.3 rely on the weighting factors listed in Tables 3.1 and 3.2 connecting the shims to their corresponding spatial harmonics. The exact weightings will in fact be shim-set dependent, varying with the coil geometry used and the number of windings. To shim a spinning sample, these efficiencies are not crucial, and trial and error will quickly determine which of the lab frame coils in the linear combination contributes most efficiently in practice to the MAS frame zonal correction field. If one were to attempt to shim in the tilted frame while stationary, however, the actual efficiencies become more important, as inappropriate shim combinations will produce not only the desired zonal shims but other tesseral shims of the same order as well.

It should further be realized that the results of Table 3.3 and the conclusions drawn above all rely on the fact that the spinner is oriented in the x-z plane. This relative orientation may be tested in practice by observing that the y-shim or any other odd-symmetry shim has no influence on the NMR lineshape in an MAS experiment. If the azimuthal alignment of the spinner and shim set is off by a phase angle  $\psi$  then the lab frame shims must be transformed further by a rotation about the z-axis. The even and odd-symmetry tesseral shims of a given  $m$ -value will transform cyclically into one another as  $m\psi$  under this rotation:

$$T_{nm} \begin{pmatrix} e \\ o \end{pmatrix} \longrightarrow T_{nm} \begin{pmatrix} e \\ o \end{pmatrix} \cos(m\psi) \pm T_{nm} \begin{pmatrix} o \\ e \end{pmatrix} \sin(m\psi). \quad (3.4)$$

This effect must of course be taken into account either to align the spinner in the lab

frame x-z axis, or to modify the linear combinations of Table 3.3 to include lab frame shims of the other symmetry as well.

### 3.5 Conclusions

In summary, some appreciation for the geometries and symmetries of typical correction fields leads to a simple and useful approach to high resolution shimming under MAS. To shim a tilted but stationary sample, correction fields of the proper geometry in the tilted frame can be produced by varying the currents through the lab frame shims in the proper ratios, which requires knowledge of the coil efficiencies in the actual shim set. Spinning, however, eliminates all but those correction field components that are cylindrically symmetric about the spinner axis, greatly simplifying the task at hand. Current may be removed entirely from the lab frame shims that do not contribute to the MAS-frame zonal shims  $B_z^{\text{lab}}$  and those with odd symmetry when the spinner is aligned in the x-z plane. Any lab frame shim that contributes to the linear combinations of the transformed zonal shims in Table 3.3 then contributes only a correction field of the same order that is cylindrically symmetric in the MAS frame. One or more of the contributing shims may be used in any ratio in place of a true  $B_z^{\text{tilt}}$  shim coil.

# References

- [1] R. C. Anderson, M. A. Jarema, M. J. Shapiro, J. P. Stokes, and M. Ziliox, *Journal of Organic Chemistry*, vol. 60, p. 2650, 1995.
- [2] L. L. Cheng, C. L. Lean, A. Bogdanova, S. C. Wright, J. L. Ackerman, T. J. Brady, and L. Garrido, "Enhanced resolution of proton NMR spectra of malignant lymph nodes using magic-angle spinning," *Magnetic Resonance in Medicine*, vol. 36, no. 5, pp. 653–658, 1996.
- [3] W. E. Maas, F. H. Laukien, and D. G. Cory, *Journal of the American Chemical Society*, in press.
- [4] C. N. Chen and D. I. Hoult, *Biomedical Magnetic Resonance Technology*. Adam Hilger, Bristol, 1989, chapter 3.
- [5] V. W. Miner and W. W. Conover, "Shimming ain't magic." Acorn NMR, Fremont CA., 1992.
- [6] F. Bloch, *Physical Review*, vol. 94, p. 496, 1954.
- [7] A. F. Mehlkopf, D. Korbee, T. A. Tiggelman, and R. Freeman, "Sources of  $t_1$  noise in two-dimensional NMR," *Journal of Magnetic Resonance*, vol. 58, p. 315, 1984.
- [8] A. N. Garroway, *Journal of Magnetic Resonance*, vol. 49, p. 168, 1982.
- [9] E. R. Andrew and R. G. Eades, *Nature*, vol. 183, p. 1802, 1959.
- [10] F. Roméo and D. I. Hoult, *Magnetic Resonance in Medicine*, vol. 1, p. 44, 1984.

# Chapter 4

## The Initiation of Radiation Damping by Noise<sup>1</sup>

### 4.1 Introduction

In the NMR of strong resonances such as water, the phenomenon of radiation damping has long been considered a nuisance. When a large net magnetization is present, radiation damping causes the magnetization vector to nutate [1]-[4] back towards the +z-axis (parallel to the magnetic field) at a rate proportional to the magnitude of the transverse magnetization. This description of radiation damping leads to the conclusion that there will be no damping effect when there is no net magnetization in the transverse plane. Of particular interest here, this implies that magnetization can be stored purely along -z. In practice, however, it is observed that even a “perfect”  $\pi$  pulse (a  $\pi$  pulse followed by a  $B_0$  gradient to dephase all transverse magnetization) leads to observable magnetization as the magnetization vector nutates from -z through the transverse plane to +z under the influence of radiation damping.

In the presence of radiation damping, magnetization left purely along -z constitutes an unstable state since the radiation damping mechanism provides a restoring force that tends to nutate magnetization back towards +z. While the restoring force

---

<sup>1</sup>A. Sodickson, W. E. Maas, and D. G. Cory, “The initiation of radiation damping by noise,” *Journal of Magnetic Resonance, Series B*, vol. 110, pp. 298–303, 1996.

is in fact zero along  $-z$ , any slight perturbation can result in a transverse magnetization component that grows exponentially at first, giving rise to the signal observed in experiments. We have found that residual RF leakage from the spectrometer and even thermal noise from the RF coil produce perturbing fields sufficient to initiate radiation damping for magnetization stored exactly along  $-z$ . These fields nutate the magnetization slightly into the transverse plane, causing a departure from the unstable equilibrium which grows under the influence of the radiation damping mechanism. To avoid radiation damping effects, the necessary approach is then to continuously suppress the initiation of radiation damping.

## 4.2 Background—Radiation Damping

There are two equivalent physical pictures that are generally used to understand radiation damping [1]. In the first, transverse magnetization induces a voltage (the signal) in the coil, which results in a current through the coil and thus an RF field. This signal-induced field  $B_r$  is always precisely on resonance at the Larmor frequency, and (by Lenz's law) lags the transverse magnetization by  $90^\circ$  [2], as shown in Fig 4-1. It thus provides a torque which tends to restore the magnetization directly back towards the equilibrium  $+z$  axis, with no extra nutation about this axis;  $d\phi/dt = 0$ , where  $\phi$  is the standard azimuthal angle. The strength of the induced self-nutating field is proportional to the component of the magnetization vector in the transverse plane, thus

$$\frac{d\theta}{dt} = -\frac{\sin\theta}{\tau_r}, \quad (4.1)$$

where  $\theta$  is the polar angle between the magnetization vector and the  $+z$  axis, and  $\tau_r$  is a characteristic time constant determined by the quality factor and filling factor of the coil, and the magnitude of the equilibrium magnetization.

Alternatively, radiation damping may be viewed in terms of power dissipation in the coil due to its finite resistance. This power comes at the expense of the magnetization energy  $-\mu \cdot B_0 = -\mu B_0 \cos\theta$  stored in the sample [3]. As power is

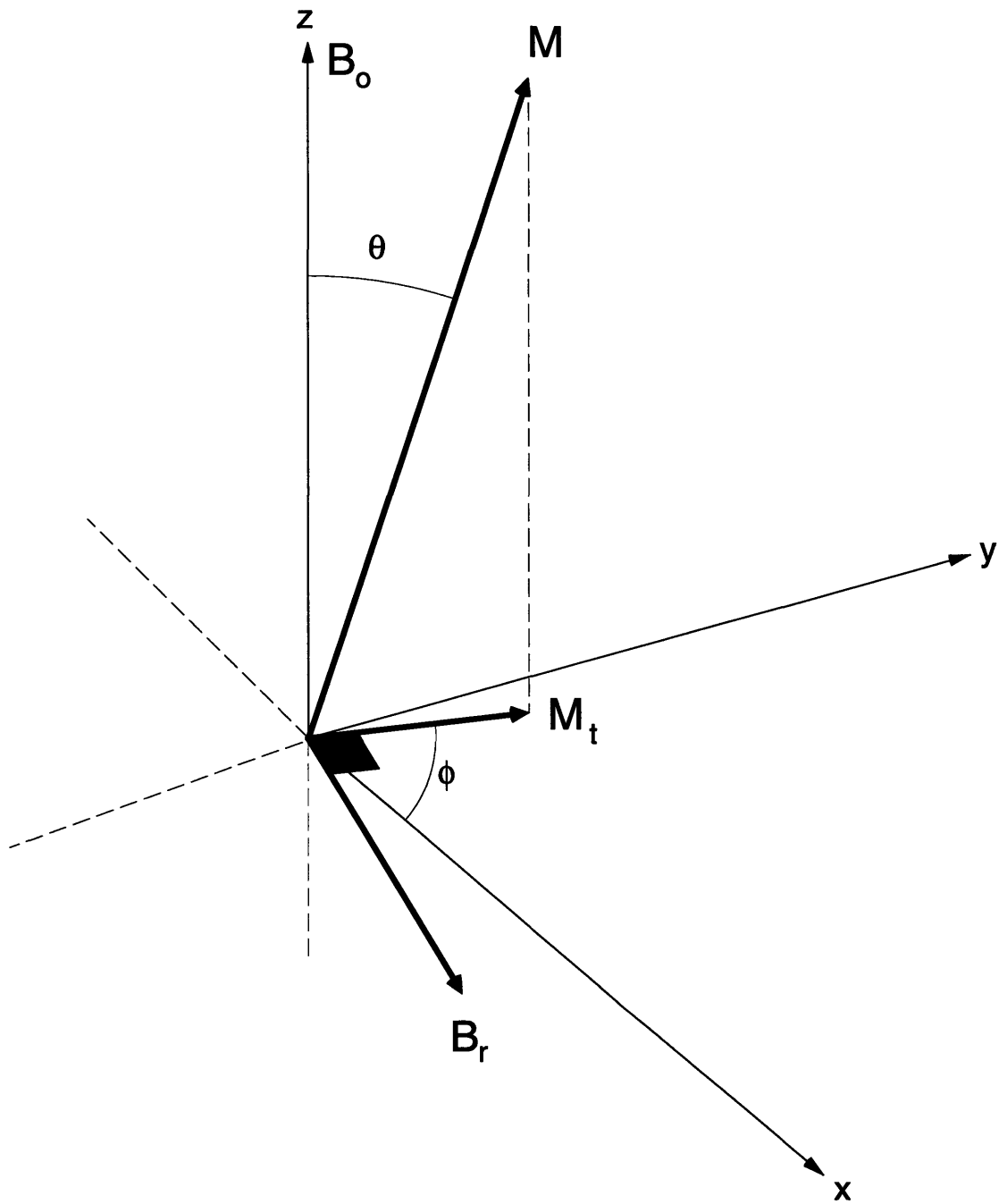


Figure 4-1: The signal-induced RF field responsible for radiation damping. The magnetization vector  $M$  precesses in a right-handed sense about the static field  $B_0$ , and induces a current in the RF coil. This current in turn induces a transverse reaction field  $B_r$  which lags  $M_t$  by  $90^\circ$ .  $B_r$  is an on-resonance RF field which causes  $M$  to nutate towards the  $+z$  axis.

dissipated, the magnetization vector must therefore nutate back towards the lower energy equilibrium state along  $+z$ , as in Eq. 4.1. Using either approach, the radiation damping time constant (in CGS units) is

$$\tau_r = (2\pi\eta M_0 Q \gamma)^{-1}, \quad (4.2)$$

where  $\eta$  is the filling factor,  $M_0$  the equilibrium magnetization per unit volume,  $Q = \omega L/R$  the quality factor of the coil (where  $\omega$ ,  $L$  and  $R$  are the resonance frequency, inductance and resistance of the coil) and  $\gamma$  is the gyromagnetic ratio. For radiation damping to be observable, an approximate condition that must be met is  $\tau_r < T_2^*$ , so that the magnetization vector can nutate significantly before the transverse magnetization decays away. This condition is often met in high-resolution liquid state studies in the presence of strong solvent resonances.

It is worth noting that radiation damping is not a local spin phenomenon but is instead a bulk magnetization effect arising from the net induced current of all spins in the sample. As such it is not strictly a relaxation mechanism (“damping” is in this sense somewhat of a misnomer): No dephasing occurs and the length of the magnetization vector does not change. Instead, the magnetization vector simply nutates back towards  $+z$ , with an instantaneous rate proportional to  $\sin \theta$ . While the appearance of this signal is somewhat similar to a traditional echo, it is not strictly an echo as nothing is in fact refocused. As described below, the envelope follows a hyperbolic secant rather than a symmetric exponential profile. Due to its non-local character, radiation damping may be completely suppressed by eliminating the net transverse magnetization, such as by dephasing it with a magnetic field gradient. Local spin packets do not undergo dissipation due to radiation damping, and can later be refocused with an opposite gradient [5], at least to the extent permitted by the truly dissipative mechanisms of diffusion and relaxation.

By explicitly incorporating the signal-induced field in the torque equation  $dM/dt = \gamma(M \times B)$ , radiation damping may be formulated as an addition to the Bloch equations [2]. In a rotating frame off-resonance by  $\Delta\omega$  with an RF amplitude  $\omega_1$  and phase  $\phi$ , the Bloch equations then become:



$$\begin{aligned}
dM_x/dt &= \Delta\omega M_y + \omega_1 \sin \phi M_z - M_x/T_2 - M_x M_z/M_0 \tau_r, \\
dM_y/dt &= -\Delta\omega M_x + \omega_1 \cos \phi M_z - M_y/T_2 - M_y M_z/M_0 \tau_r, \\
dM_z/dt &= -\omega_1 [\cos \phi M_y + \sin \phi M_x] - (M_z - M_0)/T_1 + (M_x^2 + M_y^2)/M_0 \tau_r,
\end{aligned} \tag{4.3}$$

where the last term in each equation is due to radiation damping. Because of the non-local nature of the radiation damping mechanism, the net magnetization vector must first be calculated by integration over the sample volume, rather than solving these equations locally for different spin packets throughout the sample.

For periods of free precession following an RF pulse, the radiation damping Eqs. 4.1 or 4.3 may be solved analytically (see [2, 6] for solutions in this and other situations) to yield transverse and longitudinal magnetization components

$$\begin{aligned}
M_t &= M_0 \operatorname{sech} [(t - t')/\tau_r], \\
M_z &= M_0 \tanh [(t - t')/\tau_r],
\end{aligned} \tag{4.4}$$

where  $t'$  defines the moment at which the magnetization vector is purely transverse. A nutation by polar angle  $\theta_0$  thus establishes the initial conditions,

$$\begin{aligned}
M_T(0) &= M_0 \sin \theta_0 = M_0 \operatorname{sech} [t'/\tau_r], \\
M_z(0) &= M_0 \cos \theta_0 = M_0 \tanh [t'/\tau_r].
\end{aligned} \tag{4.5}$$

An example of the effects of radiation damping is the response of a water sample in an inversion recovery experiment (Fig. 4-2). Following a near- $\pi$  pulse, the net magnetization is expected to grow exponentially from -z towards the equilibrium +z state with the  $T_1$  time-constant. After a delay  $\tau$ , a  $\pi/2$  pulse transfers  $M_z$  into observable transverse magnetization, resulting in a signal whose amplitude should follow an exponential profile as a function of  $\tau/T_1$ . When this experiment is carried out for a concentrated water solution, however (Fig. 4-2A), the longitudinal magnetization instead follows a hyperbolic tangent approach towards +z under the influence of radiation damping, as predicted by Eq. 4.4. This return to equilibrium occurs in a time much shorter than  $T_1$ , as the magnetization vector nutates rapidly from -z through the transverse plane to +z. By contrast, in Fig. 4-2B a static  $B_0$  gradient is applied throughout the relaxation delay to continuously dephase transverse magnetization and thus suppress radiation damping. In this situation,  $M_z$  does indeed follow the

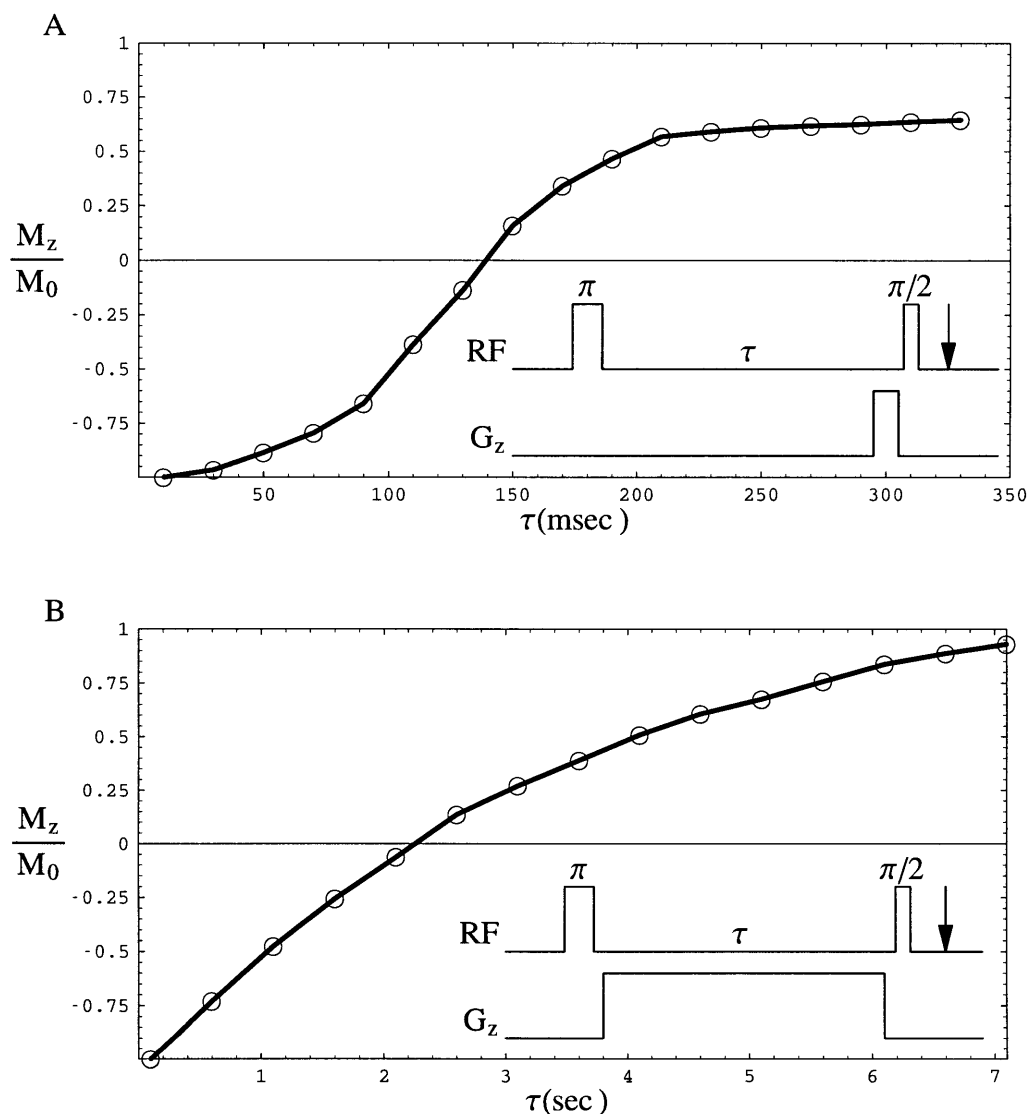


Figure 4-2: Inversion recovery experiment on a water sample, recorded on a Bruker 400 MHz AMX spectrometer.  $M_z$  is plotted vs delay time  $\tau$ . A) The gradient pulse at the end of the delay removes any residual transverse magnetization so the observed signal gives a measure of  $M_z$  before the  $\pi/2$  pulse. Note the hyperbolic tangent radiation damping profile as the magnetization vector nutates from  $-z$  through the transverse plane to  $+z$  on the time scale of  $\tau_r \ll T_1$ . (Shortening of the magnetization vector—apparent as an asymptote less than 1—occurs due to  $T_2^*$  relaxation during its passage through the transverse plane.) B) The  $B_0$  gradient provides continuous suppression of radiation damping during the delay by preventing buildup of transverse magnetization. This profile is now the standard exponential approach to equilibrium with the  $T_1$  ( $\approx 3$  secs here) of water. Note the difference in time scale between the plots in A and B: The entire return to equilibrium of experiment A occurs before the 2nd data point in experiment B.

expected exponential approach to equilibrium with the  $T_1$  of water.

### 4.3 Experimental Results and Interpretation

For purely longitudinal magnetization ( $\theta = \pi$ ), Eq. 4.1 predicts  $d\theta/dt = 0$ , and thus no radiation damping effects. Nevertheless, Fig. 4-3 demonstrates that radiation damping signals do indeed result after magnetization is left solely along  $-z$ . In the figure, an RF pulse of nutation angle greater than  $\pi/2$  is followed by a  $B_0$  gradient pulse to dephase any transverse magnetization, resulting in a magnetization vector stored along  $-z$  with a magnitude scaled by the cosine of the nutation angle. Shortening the magnetization vector  $M_0$  lengthens the radiation damping time constant  $\tau_r$ , as expected from Eq. 4.2. The envelope of the radiation damping signal follows a hyperbolic secant profile (Eq. 4.4) as the magnetization vector nutates from  $-z$  through the transverse plane to  $+z$ . While the signals follow the expected profile, their formation in the absence of an initial net transverse magnetization must still be accounted for.

We have identified two mechanisms that can initiate radiation damping following a perfect  $\pi$  pulse; RF leakage from the spectrometer and thermal noise in the RF coil. Both mechanisms may be viewed simply as producing a small RF field throughout the sample. Although the amplitudes of both these phenomena are quite small, they nutate the magnetization slightly into the transverse plane, causing an initial disturbance away from the unstable  $-z$  magnetization state which grows rapidly under the influence of radiation damping.

In order to nutate the magnetization effectively and thus initiate a radiation damping signal, the RF power must be approximately on resonance. The radiation damping time constant  $\tau_r$  is a characteristic of the spin system and the coil, and sets the inherent time scale of interest in this system, regardless of the exact perturbing mechanism responsible for signal initiation. Of concern are those components of RF power that remain correlated over a time on the order of  $\tau_r$  and thus cause an additive (rather than oscillatory) nutation over that time scale. In this case, the relevant frequency bandwidth is thus approximately  $1/\tau_r$ . RF within this bandwidth remains roughly

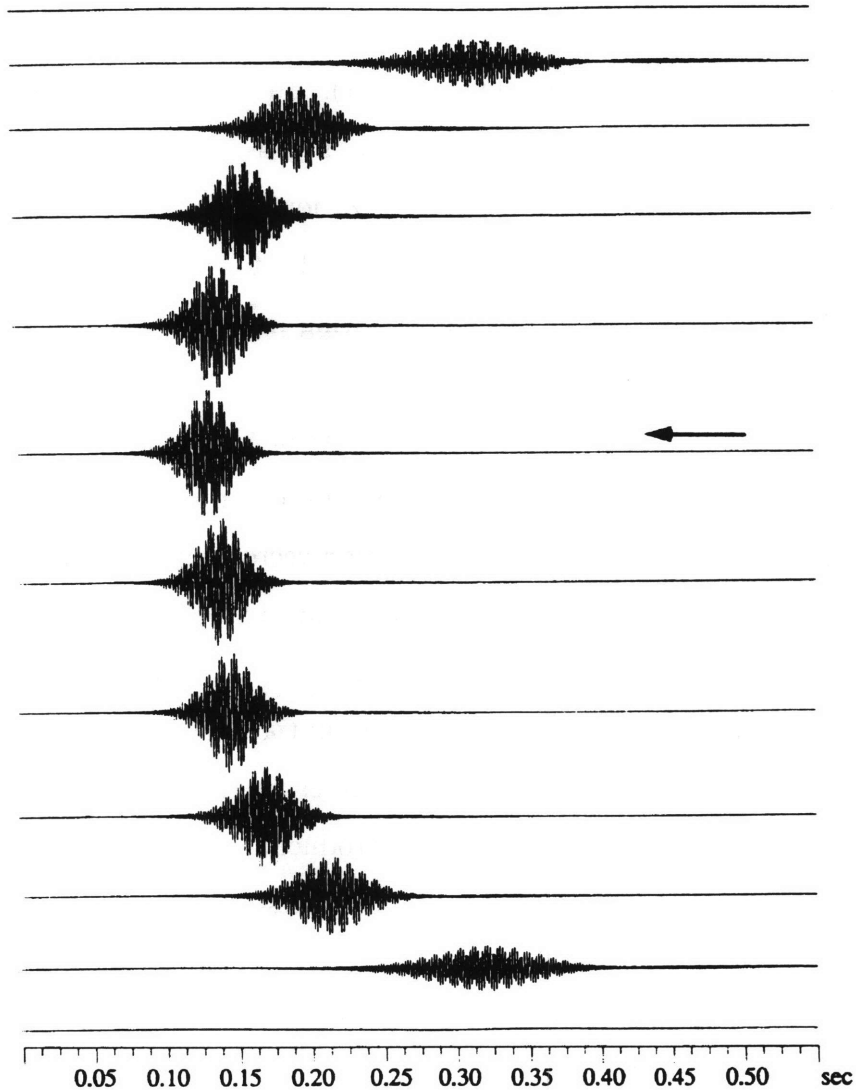


Figure 4-3: Radiation damping signals after an RF pulse – gradient pulse sequence. The arrow indicates  $\theta_p \approx 180^\circ$ . Above and below are pulse lengths respectively less than and greater than  $180^\circ$ . The  $G_z$  pulse destroys net transverse magnetization, effectively creating a "perfect"  $\pi$  pulse while reducing the length of the magnetization vector  $M_0$  and thus lengthening  $\tau_r$ . Although theory predicts that there should be no radiation damping ( $d\theta/dt = 0$ ) for  $\theta = \pi$ , radiation damping signals still occur. Note the hyperbolic secant profile of the transverse magnetization.

in phase over one radiation damping time constant, resulting in a net nutation away from  $-z$ .

RF power in the appropriate bandwidth causes a nutation with frequency  $\omega_1$ , in exact analogy to the RF amplitude during an applied pulse. On resonance and neglecting relaxation, Eq. 4.3 becomes  $dM_t/dt = -\omega_1 M_z - M_t M_z / M_0 \tau_r$ . For short times when  $M_z \approx -M_0$ , the equation may be linearized to  $dM_t/dt = \omega_1 M_0 + M_t / \tau_r$  and solved analytically, yielding an initial growth of transverse magnetization, or equivalently of the polar angle, as;

$$\frac{M_t(t)}{M_0} = \pi - \theta(t) = \tau_r \omega_1 [e^{t/\tau_r} - 1]. \quad (4.6)$$

For times  $t \ll \tau_r$ , this corresponds to a transverse component growing as  $\omega_1 t$ , clearly satisfying the initial condition of a weak rf field of amplitude  $\omega_1$ .

Spectrometer leakage occurs due to imperfect RF isolation at the transmit frequency, both on the observe channel and through additional RF connections to the probe, such as the lock channel and heteronuclear channels. Although greatly attenuated in amplitude, the leakage to the coil is coherent; the initial nutation of the magnetization vector away from  $-z$  always occurs in the same direction under the influence of the transmit frequency feedthrough, leading to a radiation damping signal whose phase is expected to remain constant from one measurement to the next.

Thermal noise in the coil is best described as white noise producing an rms voltage

$$\langle v \rangle = \sqrt{4kTBR}, \quad (4.7)$$

across the effective coil resistance  $R$ , where  $k$  is the Boltzmann constant,  $T$  the temperature in Kelvin, and  $B$  the frequency bandwidth able to influence the system of interest. As discussed above,  $B \approx 1/\tau_r$  is the approximate bandwidth in this case. The noise power within this bandwidth centered on the spin resonance frequency again causes a nutation of the magnetization vector away from  $-z$ , but the phase relative to the  $\pi$  pulse is now expected to be random.

Figure 4-4 demonstrates radiation damping signals observed on-resonance after the  $\pi$  pulse – gradient sequence. Stacked traces show the results of successive experi-

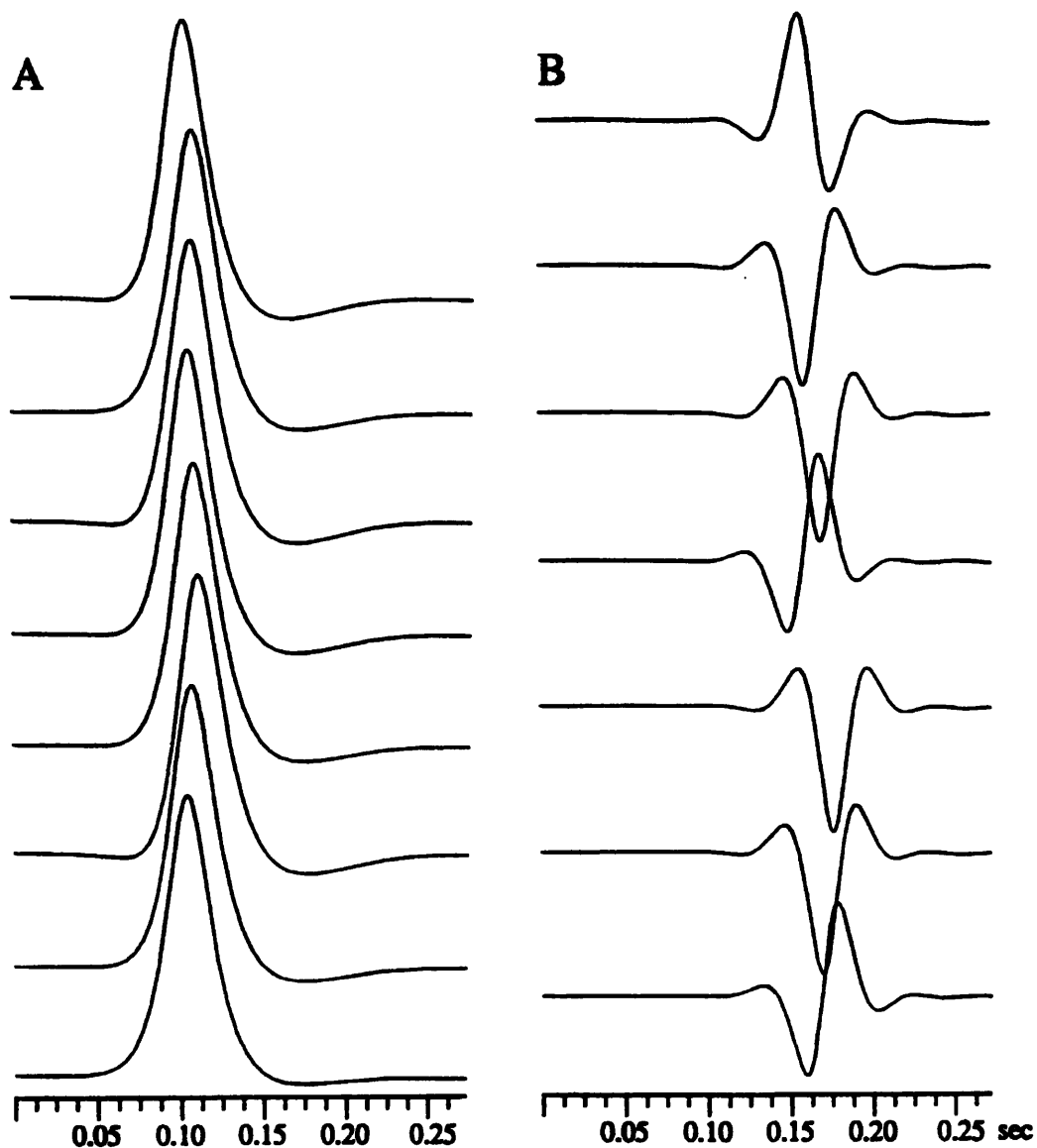


Figure 4-4: On-resonance radiation damping signals following  $\pi$  pulse - gradient, repeated under identical conditions. A) Coherent effect: the initial nutation is due to spectrometer feedthrough, resulting in a uniform phase. B) Incoherent effect: the initiation of radiation damping is due to noise, resulting in a random phase of the initial nutation and thus the signal. The signals in A occur earlier than those in B as the RF power of the spectrometer feedthrough is greater than that of thermal noise.

ments, repeated under identical conditions on a Bruker 500 MHz AMX spectrometer. In Fig. 4-4A, spectrometer feedthrough results in signals with a reproducible phase in subsequent scans. The effect is coherent because the spectrometer feedthrough causing the initial nutation always maintains the same phase relationship relative to the  $\pi$  pulse.

Fig. 4-4B demonstrates incoherent signals, produced after systematic elimination of spectrometer feedthrough at the spin frequency. The lock channel was disconnected and a blanking switch added at the amplifier input to improve the isolation. The radiation damping signal still appears but has become an incoherent phenomenon—with a random phase from one experiment to the next—as it is now initiated by noise. The signals of Fig. 4-4A occur earlier than those in Fig. 4-4B, as the field introduced by spectrometer feedthrough is larger than that from thermal noise in the coil, producing a faster initial buildup of transverse magnetization (the effective RF amplitude  $\omega_1$  is larger) and thus an earlier radiation damping signal. Once the dominant coherent leakage effect has been removed, the weaker incoherent effect becomes visible.

## 4.4 Discussion and Conclusions

Estimation of the strength of the field produced by thermal noise in the coil depends on the bandwidth  $B$  and the effective coil resistance  $R$ . As discussed above, the relevant bandwidth is approximately  $1/\tau_r$ . The problem of estimating the effective coil resistance may be simplified by viewing the probe as an equivalent  $50\Omega$  load as seen from the spectrometer, while accounting for the measured RF efficiency of the probe. The RF field experienced by the sample is proportional to the current through the small series resistance of the coil. The equivalent circuit picture allows one to bypass the details of the probe circuit itself and directly relate the current through the coil to a voltage applied across the probe terminals. Since by design the probe is tuned to resonance and its impedance matched to  $50\Omega$ , it is appropriate to calculate equivalent currents across a  $50\Omega$  load at the probe terminals (rather than across the coil resistance itself), and to scale the nutation frequency with the magnitude of the

current at this point. Applying 50W of RF power from the spectrometer through the matched 50Ω probe circuit results, for this particular probe, in a  $\pi/2$  pulse length of approximately 5μsec; that is, 1A of current into the probe translates to a nutation frequency of approximately 50kHz.

Thermal noise in the coil results in an rms voltage  $\langle v \rangle$  from Eq. 4.7 across the small series coil resistance  $R$ , or equivalently, an rms current  $\langle i \rangle = \langle v \rangle / R$ . This current transforms to an external current through 50Ω at the probe terminals, which may be scaled according to the external current supplied by the spectrometer during a pulse to determine the approximate nutation frequency of the noise power within the bandwidth  $B$ . When properly tuned, the probe simply behaves at its terminals as an effective 50Ω thermal noise source. Indeed, noise measurements on the spectrometer verify this conclusion<sup>2</sup>.

The calculation outlined above yields an approximate RF amplitude from noise of  $\langle \omega_1 \rangle \approx (50\text{kHz}/\text{Amp}) \times \sqrt{4kTB/R}$  (Amps) =  $8.7 \cdot 10^{-6}$  Hz, using  $T = 300^\circ\text{K}$ ,  $R = 50\Omega$ , and  $B = 1/\tau_r$ , with  $\tau_r = 11\text{msec}$ , an approximate value determined empirically from Fig. 4-4. Replacing  $\omega_1$  in Eq. 4.6 with the rms RF amplitude  $\langle \omega_1 \rangle$  from thermal noise results in an initial excursion from -z as:

$$\frac{M_t(t)}{M_0} = \pi - \theta(t) = \tau_r \omega_1 [e^{t/\tau_r} - 1] = 9.6 \cdot 10^{-8} [e^{t/\tau_r} - 1], \quad (4.8)$$

corresponding to  $M_t(t)/M_0 = \pi - \theta(\tau_r) \approx 1.6 \cdot 10^{-7}$  at  $t = \tau_r$ .

For the above calculations,  $\tau_r \approx 11\text{msec}$  was estimated from the width of the signals in Fig. 4-4. The peak of the incoherent signals thus occur at approximately  $15\tau_r$ . Using the hyperbolic secant magnetization profile from Eq. 4.4 to extrapolate back to  $t = 0$  yields a required  $M_t/M_0 \approx 6 \cdot 10^{-7}$  after the gradient pulse. The thermal noise effect is thus of approximately the right magnitude to explain the experimental

---

<sup>2</sup>These measurements were made by integrating a noise power spectrum over the filter bandwidth of the receiver. The integrated power levels scale linearly with bandwidth as expected from Eq. 4.7. Leaving the receiver gain constant throughout all measurements and therefore assuming a fixed noise contribution from the preamplifier, measurements were made on a 50 ohm load at 77 K and room temperature. This allows the determination of the constant background noise contribution from the receiver system, by exploiting the temperature dependence of Eq. 4.7. The equivalent noise resistance of the probe may then be determined, and as expected, its value is quite close to 50 ohms when the probe is properly matched.



results.

Another potential source of transverse magnetization that could in theory initiate radiation damping arises from statistical fluctuations of the excited spins. For an equilibrium state with  $n$  excited spins oriented along  $-z$ , on the order of  $\sqrt{n}$  spins are expected to lie in the transverse plane. This normally negligible magnetization component, though unobservable, will grow exponentially at first under the influence of radiation damping, resulting in a signal whose phase is of course expected to be random. For our spin = 1/2 system,  $n = N_{\uparrow} - N_{\downarrow} \approx N\gamma\hbar B_0/2kT = 2.1 \cdot 10^{-18}$  spins/cm<sup>3</sup>. Since magnetization is simply proportional to the number of excited spins, there is—for a 1 cm<sup>3</sup> sample—an initial transverse magnetization  $M_t(0)/M_0 = \sqrt{n}/n \approx 7 \cdot 10^{-10}$ . Linearizing the Bloch equations as above, but with  $\omega_1 = 0$  yields  $dM_t/dt = M_t/\tau_r$ , whose solution is

$$\frac{M_t(t)}{M_0} = \frac{M_t(0)}{M_0} e^{t/\tau_r} \approx 7 \cdot 10^{-10} e^{t/\tau_r}, \quad (4.9)$$

corresponding to  $M_t(\tau_r)/M_0 = \pi - \theta(\tau_r) \approx 1.9 \cdot 10^{-9}$  at  $t = \tau_r$ . This statistical noise is significantly smaller than the thermal noise, and is thus not expected to contribute to the initiation of radiation damping. Thermal noise remains the dominant mechanism for the initial nutation away from  $-z$  once spectrometer feedthrough has been adequately reduced.

Because of the ease with which radiation damping can be initiated for magnetization stored along  $-z$ , one should be cautious about storing magnetization in a  $-z$  state, and where necessary employ techniques that continuously suppress radiation damping. Several techniques exist, although most come at the expense of increased probe complexity or spectrometer modifications. A  $B_0$  gradient may be used to remove radiation damping, as in Fig. 4-2B, if one wishes only to store magnetization along  $-z$  without concern for the transverse coherences. A gradient echo may then be used to restore  $M_t$  in situations where diffusion effects are minimal [5]. Q switching has been used to lower the Q of the coil during delays, thus increasing  $\tau_r$  and reducing radiation damping. The probe Q can be left high during detection for Signal to Noise [7, 8]. Other recent techniques use an active electronic RF feedback system to

reduce the induced coil current [9, 10], allowing simultaneous suppression of radiation damping and high-Q signal detection.

In summary, a magnetization vector oriented purely along  $-z$  represents an unstable equilibrium situation in the presence of the radiation damping mechanism. Any perturbation that can create transverse magnetization—no matter how small—will, in the absence of larger perturbing mechanisms, initiate a radiation damping signal as the magnetization vector nutates away from  $-z$ . The time to onset of the signal thus depends on the magnitude of the perturbing nutation. In many spectrometers the initial perturbation is most likely caused by residual spectrometer leakage currents, resulting in coherent signals of repeatable phase. Improved isolation, while reducing the feedthrough, cannot remove the radiation damping effect entirely as thermal noise itself provides enough RF power to initiate a radiation damping signal, though with random phase and a longer time to onset. Indeed, thermal noise in the coil defines the lower limit of physical mechanisms that will initiate these nutations, and thus corresponds to the longest achievable signal delay. In order to avoid the effects of radiation damping, it is thus necessary to perform continuous suppression of the radiation damping mechanism rather than simply storing magnetization in a  $-z$  state.

# References

- [1] N. Bloembergen and R. V. Pound, “Radiation damping in magnetic resonance experiments,” *Physical Review*, vol. 95, no. 1, pp. 8–12, 1954.
- [2] S. Bloom, “Effects of radiation damping on spin dynamics,” *Journal of Applied Physics*, vol. 28, no. 7, pp. 800–805, 1957.
- [3] A. Abragam, *The Principles of Nuclear Magnetism*. Oxford University Press, London, 1962.
- [4] A. Szöke and S. Meiboom, “Radiation damping in nuclear magnetic resonance,” *Physical Review*, vol. 113, no. 2, pp. 585–586, 1959.
- [5] V. Sklenář, “Suppression of radiation damping in multidimensional NMR experiments using magnetic field gradients,” *Journal of Magnetic Resonance, Series A*, vol. 114, pp. 132–135, 1995.
- [6] W. S. Warren, S. L. Hammes, and J. L. Bates, “Dynamics of radiation damping in nuclear magnetic resonance,” *Journal of Chemical Physics*, vol. 91, no. 10, pp. 5895–5904, 1989.
- [7] C. Anklin, M. Rindlisbacher, G. Otting, and F. H. Laukien, “A probehead with switchable quality factor. suppression of radiation damping,” *Journal of Magnetic Resonance, Series B*, vol. 106, pp. 199–201, 1995.
- [8] W. E. Maas, F. H. Laukien, and D. G. Cory, “Suppression of radiation damping by Q switching during acquisition,” *Journal of Magnetic Resonance, Series A*, vol. 113, pp. 274–277, 1995.

- [9] A. Louis-Joseph, D. Abergel, and J.-Y. Lallemand, "Neutralization of radiation damping by selective feedback on a 400 MHz NMR spectrometer," *Journal of Biomolecular NMR*, vol. 5, pp. 212–216, 1995.
- [10] P. Broekaert and J. Jeener, "Suppression of radiation damping in NMR in liquids by active electronic feedback," *Journal of Magnetic Resonance, Series A*, vol. 113, pp. 60–64, 1995.